Lehrstuhl für Hochfrequenztechnik
Technische Universität München

Electromagnetic Drop Scale Scattering Modelling for Dynamic Statistical Rain Fields

Susanne Maria Hipp

Und Gott sprach: Das ist das
Zeichen des Bundes, den ich
gemacht habe zwischen mir
und euch und allen lebendigen
Seelen bei euch hinfort
ewiglich: Meinen Bogen habe
ich gesetzt in die Wolken; der
soll das Zeichen sein des
Bundes zwischen mir und der
Erde. Und wenn es kommt,
daß ich Wolken über die Erde
führe, so soll man meinen
Bogen sehen in den Wolken.

(1. Moses 9, 12–14,
Translation according to
Martin Luther)

Contents

Contents

Nomenclature

Latin Letters

$\vec{A}$	magnetic vector potential	$V\,s/m$
$\vec{a}$	arbitrary vector	
A	microwave attenuation	dB/km
A	surface area	m^2
a	large semi-axis of spheroid	m
a	power law coefficient	$dB\,h/km\,mm$
A_1	measured average integrated attenuation per length	dB/km
A_2	specific attenuation per length	dB/km
a_n	Mie coefficient a of order n	
a_n	expansion coefficients	
a_p	normalisation parameter of specific rain characteristic	
A_{e0n}	equal expansion coefficient for Helmholtz equation for TM mode of order n	
$\vec{B}$	magnetic flux density	T
b	power law coefficient	
b	small semi-axis of spheroid	m
b_n	Mie coefficient b of order n	
B_{o0n}	odd expansion coefficient for Helmholtz equation for TE mode of order n	
c_0	speed of light in vacuum	m/s
c_n	coefficients of Tchebycheff polynomials	
c_n	internal Mie coefficients c of order n	
c_{xx}	auto-covariance of signal with x polarisation	
x	x coordinate of Cartesian coordinate system	
c	speed of light	m/s
$\vec{D}$	electric displacement or electric flux density	$A\,s/m^2$
D	equivolume diameter of drop	cm
d_n	internal Mie coefficients d of order n	
ds	line element	m
dV	volume element	m^2

$\widehat{E}_0$	polarisation direction	
$|E_x|$	amplitude of electric field in x polarisation	V/m
$\vec{E}$	electric field	V/m
$\vec{E}_0$	initial electric field	V/m
$\vec{E}_i$	incident electric field	V/m
$\vec{E}_x$	x component of electric field	V/m
$\vec{E}_k$	electric field of drop with index k	V/m
$\vec{e}_x$	unit vector in x direction	
E_{0x}	complex amplitude of initial electric field in x polarisation	V/m
$E_{x,y}$	x component of electric field in y direction	V/m
$\vec{f}_k$	scattering amplitude/radiation vector	
f	frequency	Hz
$f(x)$	arbitrary function	
f_i	normalisation factor of differential equation for u_i	
f_x	variation of order x for radius perturbation	
f_{xx}	amplitude matrix entry	
g	standart gravity	m/s^2
$g_n(x)$	basis function for construction of function f(x)	
g_{ii}	metric coefficient	
h	spherical Hankel function (of first or second kind)	
$\vec{H}$	magnetic field	A/m
$\vec{H}_x$	x component of magnetic field	A/m
$H_{x,y}$	x component of magnetic field in y direction	V/m
I	Intensity	W/m^2
I_0	initial intensity	W/m^2
J	Bessel function	
j	spherical Bessel function	
j	imaginary unit	
$\vec{J}$	electric current density	A/m^2
$\widehat{k}_0$	direction of propagation	
$\widehat{k}_k$	direction of propagation vector of wave scattered by drop with index k	
$\vec{k}_0$	free space wave vector	$1/m$
$\vec{k}$	wave/propagation vector	$1/m$
$\vec{k}_k$	propagation vector of waves scattered by drop with index k	$1/m$
K	total number of drops	
k	drop index	

k	wave number	$1/m$
k_0	free space propagation constant	$1/m$
k_x	amplitude of propagation vector in x direction	$1/m$
$\vec{L}$	singular wave mode	
L	link length	m
$\vec{M}$	H/TE-mode of wave	
m	correlation index	
m	degree of Legendre function	
m	refractive index of a medium	
∇	Nabla differential operator	
$\vec{N}$	E/TM-mode of wave	
$\vec{n}_+$	normal vector pointing outside	
N	maximum necessary extension for Mie coefficients	
N	number of drops	
N	number of signal points for auto-covariance analysis	
n	expansion order of Legendre and Bessel functions	
n	index of time step	
$n(r)$	Drop size distribution	$1/m^3\,m$
N_0	Coefficient of drop size distribution	$1/m^3\,m$
$\overline{P}$	phase matrix	
P	specific rain characteristic	
p	moment of specific rain characteristic	
$\vec{r}$	location vector	m
$\vec{r}_k$	location vector of drop with index k	m
R	rain rate	mm/h
R	solution function of Helmholtz equation in r direction	
r	distance	m
r	radius	m
r_0	mean drop radius	m
r_0	unperturbed spherical radius	m
$r_{fresnel}$	maximum Fresnel radius	m
r_k	distance to drop with index k	m
r_m	normalised Gamma parameter	m
r_p	perturbed spherical radius	m
$\vec{S}$	(complex) Pointing vector	W/m^2
$\vec{S}_x$	x component of Pointing vector	W/m^2
S	scattering matrix	
s	link path coordinate	km

$S_{\mathrm{x},y}$	y direction of x component of Pointing vector	W/m^2
$S_{\mathrm{x},y}$	x component of Pointing vector in y direction	W/m^2
S_{xx}	scattering matrix entry	
T	temperature	$^{\circ}{}^{\circ}C$
t	time	s
$t(\delta)$	distribution of canting angles	
u	variable of Legendre or related functions equal to $\cos(\theta)$	
u_i	arbitrary coordinate	
$U_i(u_i)$	solution function of Helmholtz equation in general u_i coordinate	
U_v	height gradient	
v	terminal fall velocity	m/s
V_{fill}	refilled Volume	m^3
$V_{\mathrm{simulation}}$	simulation volume	m^3
W	liquid water content	g/m^3
W_{ext}	energy	J
$\overline{x}$	mean of x	
x	arbitrary variable	
x	size parameter	
Y	Neumann function	
y	spherical Neumann function	
y	y coordinate of Cartesian coordinate system	
Δz	refill height above simulation volume	m
Z	radar reflectivity factor	mm^6/m^3
z	z coordinate of Cartesian coordinate system	
z	solution function of Helmholtz equation in r direction	
Z_0	free space impedance	Ω
Z_n	derivation of function of Bessel family z_n	
z_n	function of Bessel family of order n	

Greek Letters

α	attenuation	Np
α	ratio of drops semi-axes a and b	
α	spread parameter for permittivity	
α_j	separation variable for Stäckelmatrix for differential equation of u_i concerning u_j	
Δ	Laplace operator	
δ	canting angle	
δ	variation order for radius perturbation	

$\partial\Gamma$	border of volume Γ	
η	complex bulk refractive index	
ε	permittivity	$\mathrm{As/Vm}$
ε_0	vacuum permittivity	$\mathrm{As/Vm}$
ε_r	permittivity of a medium	$\mathrm{Asm/V}$
ε_D	Debye model of permittivity of a medium	$\mathrm{As/Vm}$
ε_0	static permittivity of Debye model	$\mathrm{As/Vm}$
ε_∞	high frequency permittivity of Debye model	$\mathrm{As/Vm}$
ε'	real part of permittivity	$\mathrm{As/Vm}$
ε''	imaginary part of permittivity	$\mathrm{As/Vm}$
γ	attenuation along path transmitter - receiver	Np
γ_1	attenuation along path transmitter - drop	Np
γ_2	attenuation along path drop - receiver	Np
γ_D	relaxation frequency of Debye model	$\mathrm{1/Hz}$
λ_s	relaxation wavelength of Debye model	
$\Im$	imaginary component	
Λ	inverse scale parameter/rate parameter of drop size distribution	$\mathrm{1/m}$
λ	wavelength	m
μ	permeability	$\mathrm{Vs/Am}$
μ	shape parameter of Gamma distribution	
μ_0	vacuum permeability	$\mathrm{Vs/Am}$
ω	angular frequency	$\mathrm{1/s}$
∂	partial derivation	
Φ_{ij}	Stäckelmatrix for differential equation of u_i concerning u_j	
π	angular Mie π function of order n	
φ_x	phase of wave in x polarisation	rad
Ψ	scalar potential	V
Φ	solution function of Helmholtz equation in φ direction	
Ψ	solution function of Helmholtz equation	
$\Re$	real component	
ρ	(charge) density	$\mathrm{As/m^3}$
Σ	optical extinction	$\mathrm{1/km}$
σ	conductivity for dielectric	
σ_x	standard deviation of x	
σ_{abs}	absorption cross section	$\mathrm{m^2}$
σ_{b}	backscattering/monostatic/radar cross section	$\mathrm{m^2}$
σ_{bi}	bistatic cross section	$\mathrm{m^2}$
σ_{d}	differential cross section	$\mathrm{m^2/rad}$
σ_{ext}	extinction cross section	$\mathrm{m^2}$

Nomenclature

$\sigma_{\mathrm{ext,Vol}}$	extinction cross section normalised on volume	$^1/_{\mathrm{m}}$
σ_{s}	scattering cross section	m^2
τ	angular Mie τ function of order n	
Θ	solution function of Helmholtz equation in θ direction	
θ	polar angle of spherical coordinate system	
φ	azimuth angle of spherical coordinate system	

Subscripts

a	absorbed component
cross	cross component (Pointing vector)
c	coherent component
ext	extinction
f	incoherent component
h	horizontal polarisation
int	internal component
i	incident component
$\parallel$	parallel direction/polarisation
$\perp$	perpendicular direction/polarisation
φ	φ direction/polarisation
r	r direction/polarisation
r	radial direction
s	scattered component
θ	θ direction/polarisation
t	total field component
v	vertical polarisation
x	x direction/polarisation
y	y direction/polarisation
z	z direction/polarisation

x

1 Introduction

Water is vital to life on earth. The prevailing reserve of water exists as salt water, which is not drinkable. Ground water, which is supplied by precipitation or indirectly by rivers, serves as main resource for mankind. Therefore, precipitation is vital.

In contrast, hazardous events also emerge from precipitation. Insufficient precipitation causes droughts, excessive precipitation causes floods. Accordingly, to prevent consequences of extreme weather situations, water flow structures such as barriers or storm drains regulate water flow. However, to control flow, hydrologists researching this topic need a reliable measurement database of flow inputs such as precipitation.

Precipitation can be observed using rain gauges such as presented in figure 1.1, measuring the mass of collected water in discrete time intervals. Nevertheless, this process suffers from limited accuracy, affected by unknown variables of wind and exposure (Nešpor and Sevruk 1999; Sevruk and Zahlavova 1994). In order to acquire weather radar data, the gauge results serve as local truth to derive a relation between radar backscattering and actual rain rate. Weather radars emit a pulsed signal and detect the backscattered answer as illustrated in figure 1.2. They evaluate rain characteristics from the backscattering by clouds and precipitation particles. Since strong backscattering originates from large buildings or mountains illuminated by the radar beam, weather radar is poor for the estimation of precipitation in cities and mountainous regions.

Analogously, radiometers monitor precipitation and clouds (for an overview on radiometers refer to Hornbostel et al. (1997); Battaglia et al. (2009)). On the one hand, these are located on the earth and use unpolarised atmospheric radiation from the sun or diffuse skylight as their source. Thus, they receive natural radiation from the atmosphere. Alternatively, radiometers are mounted on satellites observing the influence of clouds and precipitation on thermal radiation from the ground. Moreover, both earthly and celestial setups can use active sources to analyse the scattering. Prominent missions, combining space born radiometer and radar, intended to derive precipitation are the Tropical Rainfall Measuring Mission (TRMM) (Simpson et al. 1996) launched 1997 and its extension the Global Precipitation Measurement (GPM) scheduled for 2013 (Smith et al. 2007).

Contemporary weather prediction and monitoring is based on the previously described devices. They are widely known due to their use in public weather forecasting, for instance in television or newspapers.
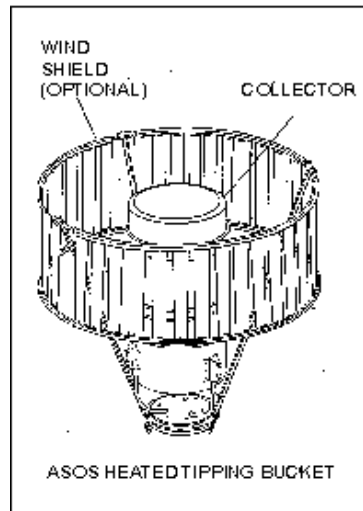
Figure 1.1: Concept of a tipping bucket rain gauge (from the American National Weather Service http://www.nws.noaa.gov/asos/tipbuck.htm).

1.1 Measurements of Scattering by Rain Fields

1.1.1 Former and Contemporary Campaigns

Extending the precipitation database is essential for hydrological models and simulations. A novel approach has emerged over the last few years. In short, the influence of precipitation on the signal of point-to-point links serves as an additional input for weather monitoring. When crossing the path of point-to-point links precipitation decreases the transmitted signal, where the received signal results from a line integration of the attenuation over the link length.

Early investigations of this idea are described by Ruf et al. (1996). The group performed measurements in Pennsylvania using a dual polarised link. They expected the relation of attenuation to rainfall rate to be linear as suggested by Atlas and Ulbrich (1977). At one end of the transmission link a 35 GHz transmitter emitted waves in horizontal and vertical polarisations. At around 100 m and 1000 m distance, trihedral corner reflectors with diameters of 15 cm and 46 cm, respectively, were installed. Furthermore, an examination of the stability of the setup in addition to an analysis of the differential attenuation and phase were realised.

At the same time, Rincon and Lang (compare with the review (Rincon and Lang 2002) and figure 1.3) equipped a path with a length of 2.3 km at Wallops Island, Virginia, USA with a four frequency link. At 8.45 GHz, the links were dual polarised, at 25 GHz and 38 GHz horizontal polarisation was available. Along the link, ten rain gauges recorded the rain rate. The goal of the project was the derivation of the drop size distribution (DSD) parameters, rain rate and rain accumulation. The group analysed the attenuation of two measurement links and reversely calculated the DSD parameter.
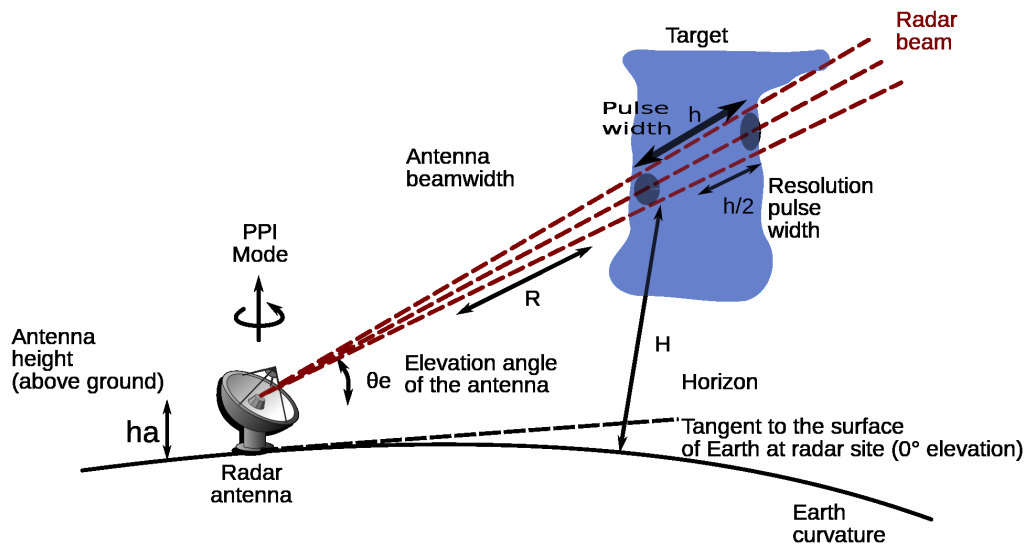
Figure 1.2: Illustration of a weather radar describing the basic concepts (from Wikipedia article about weather radar http://en.wikipedia.org/wiki/Weather_radar).

The derivation of the attenuation depending on DSD will be outlined in this work in later chapters. The group compared their results with disdrometer data.

Groups of scientists launched a large project called Mantissa (closed in 2004), involving partners all over Europe, built microwave links in the UK (Bolton, reuse of (Holt et al. 2000)), Italy (Sondrino and Bologna) and Germany (Essen). The links operated at one or two frequencies. The groups estimated occurrence and amount of rain. The resulting attenuation data served as a benchmark for radar data and was correlated with rain gauge and weather radar data from stations nearby. Furthermore, the project aimed at implementing the derived precipitation data in hydrological and water models. The project homepage (`http://prswww.essex.ac.uk/mantissa/`) and several publications (Holt, Kuznetsov, and Rahimi 2003; Rahimi et al. 2003; Rahimi 2004; Upton et al. 2005; Rahimi et al. 2006) give detailed information.

Succeeding this project, the group in Bolton (Cummings et al. 2009) published results where they acquired rain rate, drop size information and precipitation type using the attenuation and phase difference of a dual frequency link.

Further projects are currently in progress in the Netherlands, Japan, Norway, Spain and the Czech Republic.

In the Netherlands, Leijnse (2007); Leijnse, Uijlenhoet, and Stricker (2008) built a transmission link of 4.89 km. The link operates at 27 GHz and has a sampling rate of 10 Hz. In order to compare results with rain data seven rain gauges worked along the link. Furthermore, a microwave scintillometer measured temperature and humidity, two parameters directly influencing the effective permittivity $\varepsilon_{r,\text{eff}}$.

In Japan, Hirata et al. (2009) analysed rain along a 400 m path employing vertically
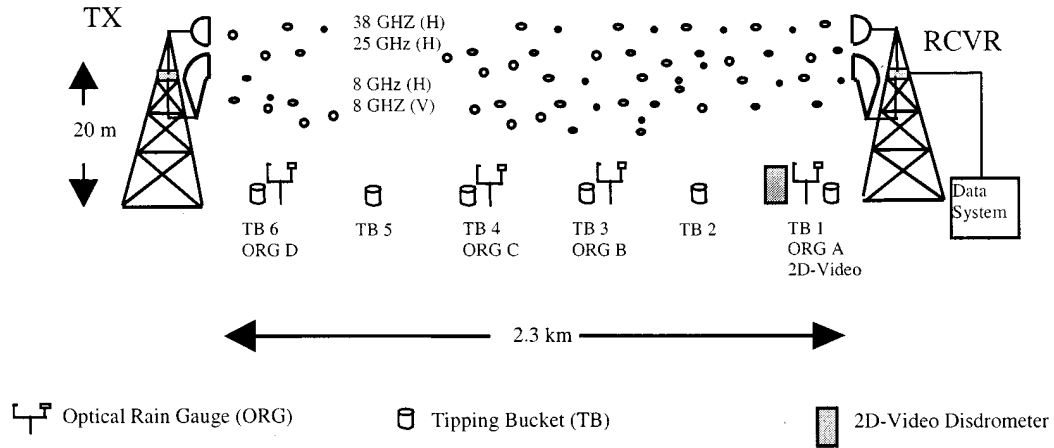
Figure 1.3: Measurement setup at Wallops Island performed by Rincon and Lang (2002).

polarised transmissions at 120 GHz to investigate various DSDs in Atsugi. In Nagoya, Minda and Nakamura (2005) compared data from a link of 820 m at 50 GHz with sensors for temperature, water vapour, weather radar and satellite measurements from TRMM.

In Kjeller, Norway, a star-like network with 5 QPSK links was built up by Cheffena (2010). Measurements recorded statistics for wet and dry periods. The group observed a change in $\varepsilon_{r,\text{eff}}$ caused by temperature and humidity variations.

In Spain, Garcia-Rubia et al. (2011) measured link data with a horizontal dual frequency link at 38.75 GHz and 85 GHz with a length of 840 m. They compared this data with a number of alternative methods including satellite measurements, an earth stationed radiometer, a laser disdrometer, a weather radar and rain gauges. The group correlated the attenuation of the links with results applying a statistical method (compare to section 4.2.1) using rain statistics obtained by weather radar and disdrometer.

In Prague, several groups (Fiser and Rezacova 2007; Valtr et al. 2011; Zvanovec and Pechac 2011) set up a link with a vertically polarised transmitter at 38.32 GHz along a link length of 9.3 km. Another dual frequency link, operating at vertical polarisation, transmitted along a 850 m path at 58 GHz and 95 GHz. Video images of the test site and temperature, humidity, air pressure and wind sensors as well as three rain gauges served as comparison for the link data. A 500 m optical link and radar data supplied additional input.

The attenuation caused by precipitation is significant for the design of point-to-point links e.g. in telecommunications. Due to regulations, a defined availability of the mobile network is required thus the failure probability must not exceed a certain threshold. Indeed, attenuation due to precipitation may decrease the received power provoking link failure. Therefore, the amount and timely distribution of precipitation needs to be considered during network planing. Information is given in the ITU-Handbook of

point-to-point links (ITU 2008) and several recommendations (ITU Recommendation P.838; ITU Recommendation P.525; ITU Recommendation P.530; ITU Recommendation P.676; ITU Recommendation P.840; ITU Recommendation P.837; ITU Recommendation P.678; ITU Recommendation P.1815; ITU Recommendation P.313; ITU Recommendation P.526; ITU Recommendation P.618; ITU Recommendation P.839; ITU Recommendation P.453; ITU Recommendation P.836). In conclusion, purpose-built transmission links for determining precipitation characteristics were and are a subject investigated worldwide. The presented experiments varied in frequency, path distance, polarisation and supporting precipitation measurements.

In contrast to the purpose-built links described earlier, Messer, Zinevich, and Alpert (2006) first proposed to use already installed and operating microwave links as sources for data, namely point-to-point links from the backhaul network of commercial mobile phone providers. Currently, this area is further explored by certain groups.

The pioneering group in Israel collected data from more than 200 point-to-point links. They evaluated 22 links in the region of Tel Aviv to generate rain maps and compared their results with weather radar measurements of the area matching these maps. The group performed evaluation of rain characteristics utilising advanced methods such as tomography and Markov modelling (Messer et al. 2008; Zinevich, Alpert, and Messer 2008; Goldshtein, Messer, and Zinevich 2009).

Berne et al. (Schleiss and Berne 2010) combined four links in Paris to distinguish between wet and dry periods. They studied this question with actual measurements and in theory.

In the Netherlands, the group around Uijlenhoet (Leijnse 2007; Leijnse, Uijlenhoet, and Stricker 2007) started with two links and ultimately obtained data from further links. DSDs, which were actually measured in the Netherlands, served for the derivation of a power law to convert between attenuation and rain rate. After applying this relation to the recorded attenuation data, the group evaluated correlation errors between different measurement systems. Two weather radars and a rain gauge adjacent to the links provided the comparison data. Additionally, the group studied known problems arising from the measurement method, namely the estimation of the signal baseline for dry conditions, antenna wetting as well as coarse time and power resolution.

So far, the still young approach of exploiting the attenuation on commercial point-to-point links rises in interest. The aforementioned groups contributed to a Winter school held in Garmisch-Partenkirchen in 2012 meeting the demand of students all over the world.

1.1.2 The PROCEMA Project

Collaborators from Israel and Germany established the virtual joint institute PROCEMA (Regional Precipitation Observation by Cellular Network Microwave Attenuation and Application to Water Resources Management) (Chwala et al. 2012). Partners in Israel were Messer from the school of electrical engineering and Alpert from the department of geophysics and planetary sciences, both from Tel Aviv University. The hydrological part was covered by Rimmer from the Israel Oceanographic and Limnological Research Ltd.

In Germany, the Institute for High-Frequency Engineering, at TUM, jointly with the Institute for Meteorology and Climate Research of the Karlsruhe Institute of Technology, worked together with Ericsson Germany. The German part comprised meteorological considerations for combining link and either weather radar or rain gauge data. Furthermore, a purpose-built transmission experiment with a very high time resolution and theoretical investigations concerning the transmission of electromagnetic waves through rain (Kunstmann et al. 2010) was investigated. Figure 1.4 shows the locations of the links and gauges.

The PROCEMA group evaluated possible methods to realise weather maps from attenuation data merged with other sources. In particular, the Copula method (Vogl et al. 2012) is able to combine data from different measurement methods observing different or even contrasting properties like spacial or temporal resolution. First implementations with time series from radar and rain gauges showed promising results. Currently, data obtained from five commercial microwave links in the Alpine region is included in the synthesis (Chwala et al. 2012). Additionally, the group evaluated new detection methods of wet and dry periods applying these links (Chwala et al. 2011c).

To gain better insight into the underlying physical effects, both detailed measurements as well as theoretical simulations, described in the next section, accompanied the project. The measurements exhibited a high sampling rate of 25 kHz and originated from a purpose-built transmission experiment spanning a 650 m path. The monostatic setup with combined transmitter and receiver operates at 22.235 GHz and 34.8 GHz and switches between vertical and horizontal polarisation. Range gating ensures the exclusive detection of rays reflected by a trihedral corner reflector located at the end of the path. Due to the monostatic design, transmitted and received signals are coherent (Chwala et al. 2010a; Chwala et al. 2010b; Chwala et al. 2011b; Chwala et al. 2011a).

1.2 Modelling of Scattering by Rain Fields

Included in the PROCEMA project, this present work deals with simulations of propagation of electromagnetic waves through rain fields. Although several methods for investigating this subject already exist, this work offers a new approach.

One of the established models integrates the extinction caused by the rain drop over the statistical drop ensemble, resulting in the attenuation caused by the rain field. The extended radiative transfer model utilises the scattering pattern at a drop to express its influence. Layers of drops are also described by statistics.

However, the model proposed in this work examines the scattering effects in greater detail. In addition to regarding the rain field as a whole, it inspects the individual scattering contributions on drop scale.

The special case of forward transmission in the atmosphere on ground level applies to microwave links. Satellite - earth transmission propagates in the forward direction as well but along a vertical or nearly vertical path. Therefore, these rays cross different atmospheric layers with varying properties.

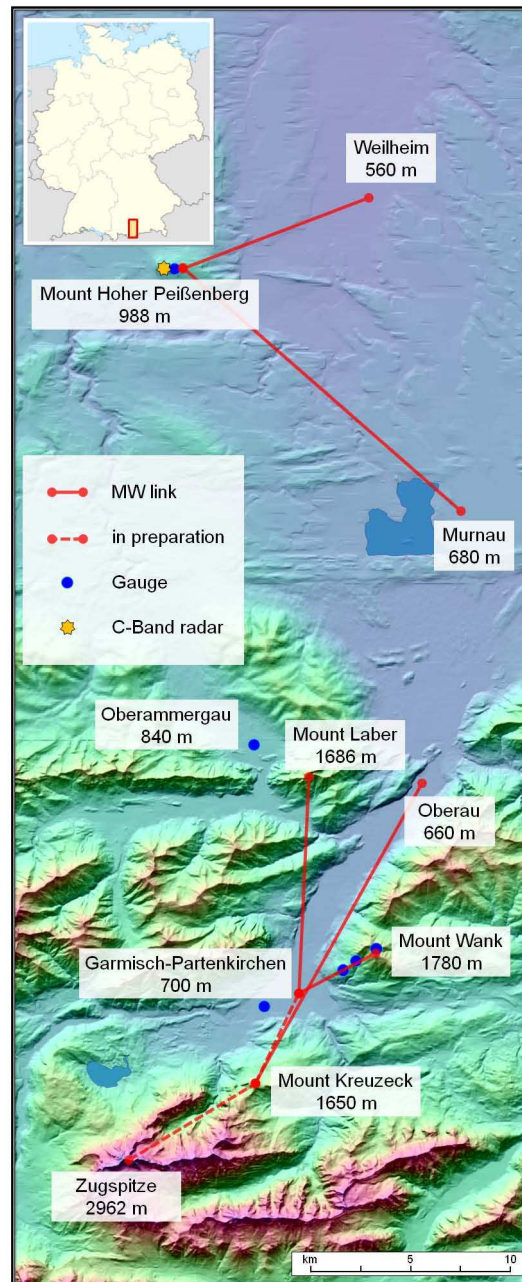In contrast to transmission setups where the receiver records the signal propagation

Figure 1.4: German test sites of the PROCEMA experiment near Garmisch-Partenkirchen (from Chwala et al. (2012)).

through the scatterers weather radars receive their backscattered response. This slightly modifies the equations, which are used. There are two main types of weather radar (compare Ishimaru (1997)). Conventional or non-coherent radars neglect phase information. These may be compared to commercial backhaul network links, which only record the signal strength. Coherent or pulsed radar uses phase information. Utilising this, the velocity distribution of rain drops may be calculated. Similar to the power law used for attenuation caused by precipitation, as described in the following subsection, modified power laws relate radar reflection to rain rate.

Furthermore, the approach described in this work serves to model these further applications by using small adaptations. For instance to apply the method to radar applications the propagated path changes by joining the position of receiver and transmitter.

1.2.1 Previous Work on Modelling

In parallel to measurements, theoretical studies investigate the area of scattering by rain fields in great detail. Science and commerce need models to estimate the impact of rain on a propagation path. In case of transmission the focus lies on attenuation, which is in contrast to the case of reflection such as in radar applications attenuation. The severity of its calculation depends on the complexity of the transmission path. Especially in mobile phone environments the waves observing attenuation propagate on ground level. In this case rain is rather homogeneous. For uphill propagation paths or in radar applications the scenario exhibits increasing complexity. Here the waves pass the atmosphere under a finite angle observing variations of the atmospheric conditions. The propagation through completely different atmospheric layers takes place in earth - satellite paths in radiometry or in commercial applications such as television broadcasting.

Considerations in the area of mobile communication merely require timely statistical information about the influence of rain (compare ITU Recommendation P.837, Crane (1996)): The estimation of the availability of the communication connections depends on worst month or daily average records. In contrast, analysis of influence on satellite paths is more ambiguous. Considering the varying atmospheric conditions the calculation of propagating waves requires analytical methods. The radiative transfer method, using spatial statistical properties, fulfils this requirement.

Many publications discuss waves propagation through rain. For instance, Oguchi (1983) contributed an overview, which serves as resource for this work. However, to start with, Ishimaru (1997) outlined a general view of scattering in random media. Beginning with single scattering he explained particle size distributions, for instance of particles in the atmosphere and in rain. After considering both static and dynamic cases of randomly distributed particles he investigated propagation related issues, such as pulses, backscattering and the Doppler effect caused by moving particles. Then, Ishimaru introduced coherent and incoherent signals, a concept that will also be used later on in this work. The presented topics make the book of Ishimaru of value for many applications, especially statistical considerations, approximations and special theories, such as the radiative transfer method, considerations of fluctuations, remote sensing

and surfaces.

Many publications focus on the general principle of scattering by raindrops, particularly on the concept of extinction, denoting the amount of power removed by the rain field. Integrating the extinction over the drop size distributions returns the attenuation. Basic publications such as Oguchi (1983) and the books by Born, Wolf, and Bhatia (1999); Kerker (1969); van de Hulst (1981); Bohren and Huffman (1983) used Mie theory to calculate the scattering. This work adapts this method in section 4.2.1.

Recently, many publications accounted for the non-spherical shape of rain drops. Aydin and Lure (1991) and Asano and Yamamoto (1975) analytically calculated the extinction of spheroidal drop shapes. The T-Matrix theory (Waterman 1976; Mishchenko, Travis, and Mackowski 1996) considers arbitrary drop shapes by integrating over their contour. This method yields scattering parameters and extinction.

Another often applied method to derive scattering parameters is the Discrete Dipole Approximation (Draine and Flatau 1994). This method locates small dipoles along the shape of the scattering object and derives the resulting scattering. An overview of this and further methods was given by Kahnert (2003). Scientists interested in these advanced considerations are referred to the Scattport website (`http://www.scattport.org/`), a collection of programs and articles concerning scattering issues.

In addition, it is interesting to note recent discussions about the concept of extinction itself by Mishchenko (2008) and Berg, Sorensen, and Chakrabarti (2008a); Berg, Sorensen, and Chakrabarti (2008b).

According to Setijadi et al. (2009) three aspects have a huge impact on the attenuation: Multiple scattering, polarisation and temperature. Furthermore, numerical calculations using non-spherical drops such as by Aydin and Lure (1991) and Asano and Yamamoto (1975) showed polarisation dependent attenuation.

Moreover, temperature directly influences the refractive index leading to modified electromagnetic characteristics of the rain drops. Setijadi et al. (2009) plotted the deviation of rain attenuation for a specific temperature related to the attenuation at $20\,^\circ$C versus frequency. They discovered three frequency values in the spectrum, around which the response of attenuation to temperature changes reversed its sign. Particularly looking at the interval between $12\,$GHz and $40\,$GHz showed a turning point at $22\,$GHz and provided the following characteristics: At $12\,$GHz an increase in temperature leads to additional scattering. At $40\,$GHz the size parameter increases, thus reducing the attenuation with increasing temperature. Furthermore, Medhurst (1965) compared calculations of attenuation with actual measurements from literature. He concludes an influence of less than $30\,\%$ of the temperature dependence on attenuation.

The remaining issue of multiple scattering will be dealt with in the appropriate chapter of this work.

Power Law

Solving the equation for the dependency of attenuation on the rain rate is cumbersome, even for spherical scatterers. Consideration of the extinction demands even larger effort, when applying advanced coordinate systems such as spheroidal ones to account for a

realistic drop shape. Therefore, classical publications (Oguchi 1983) as well as the ITU (ITU Recommendation P.838) recomment the use of a convenient power law relating rain rate R (in $^{mm}/h$) and attenuation A (in $^{dB}/km$) by

$$A = aR^b \, . \tag{1.2.1}$$

The parameter b works out to be almost unity, yielding a nearly linear relation.

Olsen, Rogers, and Hodge (1978) studied the equation concerning Mie scattering and different DSDs. The group calculated the Mie coefficients using asymptotic approximations for low frequencies and derived the extinction cross section for high frequencies. They obtained values related to frequency, temperature and various DSDs. Between these ranges, the Mie coefficients have to be fit numerically. Additionally, Atlas and Ulbrich (1977) performed further calculations for the Mie coefficients.

Publications presented numerical analyses of the power law coefficients using spheroidal (Aydin and Lure 1991) and Beard-Chuang shaped drops (Leijnse 2007) by using the T-Matrix method. In the publication from Aydin and Lure (1991) the group investigated the influence of different DSDs on power laws for attenuation and differential phase shift, while later on (Aydin and Daisley 2002) they additionally investigated the influence of canting and oscillations on the power law.

Many scientists analysed the applicability of the power law. In his Ph.D. Leijnse (2007) performed simulations concerning the influence of temperature. For dual link models he investigated the impact of different polarisations, frequency and the spatial separation of the links on the power law. His research showed stability in the following ranges:

$$
\begin{aligned}
250\,\text{K} \quad &< T < \quad 315\,\text{K} \\
1.04 \quad &< b < \quad 1.185 \\
0.125 \quad &< a < \quad 0.145
\end{aligned}
$$

Berne and Uijlenhoet (2007) used an artificial 2D rain field to test the power law concerning different frequencies and polarisations. Moreover, artificial rain fields served as simulation input for Luini and Capsoni (2010), who used their "MultiEXCELL" method (Luini and Capsoni 2009), and Matricciani (2009), who used the "synthetic storm technique" (Matricciani 1996).

A special attribute of point-to-point links is the measurement of the averaged integrated attenuation. Many publications deal with problems concerning this process. Actually, the rain causes possibly varying attenuation along the path, while the receiver records the integral along the total link length L

$$A_1 = \frac{1}{L} \int_0^L aR(s)^b \mathrm{d}s \, . \tag{1.2.2}$$

However, only an equation such as

$$A_2 = a \left[\frac{1}{L} \int_0^L aR(s)\mathrm{d}s \right]^b \tag{1.2.3}$$

allows the inversion of the specific attenuation and the path averaged rain rate

$$\frac{1}{L} \int_0^L R(s)\mathrm{d}s = \sqrt[b]{\frac{A_2}{a}} \, . \tag{1.2.4}$$

If b is unity equations (1.2.2) and (1.2.3) are equal, else the calculation leads to in-accurate results. This problem was discussed by Townsend and Watson (2011), as well as Berne and Uijlenhoet (2007) and Leijnse (2007). Small errors occur, if b is linear, which is appropriate around 25 GHz (Leijnse 2007). Therefore, for extended link lengths the error due to inversion possibly exceeds discrepancies by a non-linear b. Here b is chosen to be one. For rain rates above 40 $^{mm}/_h$, Leijnse (2007) recommended the power law.

1.2.2 New Dynamic Model on Drop Scale

The receiver records an attenuated signal caused by the statistical medium. Dynamics inside the medium excite an additionally fluctuating signal. Ishimaru denotes those contributions by coherent (or attenuated) signal and incoherent (or noisy) signal.

While present works, such as presented in section 1.2.1, focus on the calculation of attenuation, the fluctuating signal is disregarded due to the high effort required for its derivation.

For the first time, this work presents a new approach to expand the theoretical investigations of statistical rain by analysing the rain field on drop scale. To this end, the model takes into account the scattering by each individual drop during the continuous rain process.

This method not only yields very accurate results for the effect of a real rain field on propagating waves, but allows numerous properties of the rain drops to be considered. Thus, the method assigns individual drop attributes such as size and position or specific wind speeds. A different refractive index per drop reproduces the propagation through different atmospheric layers exhibiting for instance different temperatures. Therefore, the model has the capability to model satellite or up-/downhill transmission paths in addition to horizontal ones.

Furthermore, the model accounts for the dynamics of every drop. Rain drops observe different terminal velocities according to their sizes following models found in literature. Additionally, motion of drops results from internal oscillation and canting. These properties may vary during the simulation time. The Doppler effect is an example of the impact of motion on the rain medium. Hipp et al. (2011a), for the first time, published the Doppler results for undisturbed drops applying this method.

Beyond the dynamics of the single drops, the whole rain field observes motion. Therefore, the presented model allows simulation of a cloud passing a certain volume by imitating on- and offset of precipitation. The implementation in MATLAB allows adjustment of the simulation volume comfortably. To this end, the user modifies the volume extension in all three dimensions by defining size limits.

Thus, supplementary to the attenuation of rain fields, this work takes the whole scattering pattern into account. Depending on its size, every drop observes a differnt scattering behaviour. Thus, amplitudes at different observation angles vary. The combination of the scattering amplitudes of the individual rain drops provides the final signal recorded at the receiver after passing the whole rain field. Therefore drops whose locations are diagonal to the direct path also contribute to the total signal. This contrasts former approaches, which only consider drops in the direct path between transceiver and receiver, denoted by direct forward scattering.

The application of the scattering pattern gives rise to a new effect. The scattering pattern of large drops shows side lobes. At these angles, the scattered power has a maximum in addition to the forward scattering amplitude. Thus, at these specific angles the drops contribute a larger amount of power to the incoherent signal.

The explicit derivation of the scattering pattern is of interest in radar research. A radar emits waves focused in a beam and records the reflected power. Thus, the backscattering amplitudes returned by this model directly accumulate to the radar signal. Furthermore, the transmitting and receiving antennas have radiation patterns themselves. The model is capable of implementing these patterns. In conclusion, the approach yields results for transmission and reflection.

While contemporary models using extinction focus on co-polarisation results of horizontal and vertical linear polarised waves, the presented model yields a variety of polarisation results. By defining the input waves, it is able to model linear as well as circular or elliptical incident polarisation and returns values for the co- and the cross-polarised component. The result section shows an analysis of examples of linear horizontal polarisation. Additionally, it presents results of first simulations evaluated with a variety of spectral and statistical methods.

A major contribution of this thesis was the implementation of the presented model in MATLAB to demonstrate the versatility of the model (Hipp et al. 2010; Hipp et al. 2011d; Hipp et al. 2011b; Siart et al. 2012). Chapter 5 presents the program flow including definitions of variables. In short, the simulation model performs the following operations. Drops are created and distributed over a scattering volume according to given specifications. These drops serve as scatterers for incident waves. Accumulating all contributions by the individual drops gives a time sample of the received field. For the next time sample, the drops fall and the algorithm starts over.

An analysis of results obtained with the model for a simulation of the purpose-built experiment of the PROCEMA project shows the potential of the algorithm.

During the design process commercial products served for the verification of the simulation results (Hipp et al. 2010). Following the design and implementation process the MATLAB algorithms were optimised concerning memory and time consumption. Appropriate strategies lead the development to success (Hipp et al. 2011c).

2 Basic Electromagnetics

One of the main goals of this work is to shed light on the electromagnetic principles of the propagation of microwaves through rain. The electromagnetic theory is based on Maxwell's equations, describing the interaction of electric and magnetic fields. The Helmholtz equation, derived by merging Maxwell's equations, mathematically expresses the propagation of electromagnetic waves in free space or in a medium. Waves cross both, free space and medium, when travelling through a rain field.

This chapter outlines Maxwell's equations as well as the material equations. These allow the definition of scalar and vector potentials and different gauges for the remaining degrees of freedom. Merging all equations yields the wave equations and the Helmholtz equations for the potentials, describing the propagating waves. Applying the solution of the Helmholtz equations returns electric and magnetic fields in general.

2.1 Maxwell's Equations

Maxwell's equations, published between 1861 and 1862, describe the theory of electromagnetism (or electrodynamics) predicting electromagnetic waves, discovered experimentally by Hertz 25 years later. Following Jackson (1998) and van Bladel (2007) they are

$$\text{Coulomb's law} \qquad \nabla \cdot \vec{D} = \rho \,, \qquad (2.1.1)$$

$$\text{modified Ampère's law} \qquad \nabla \times \vec{H} = \vec{J} + \frac{\partial \vec{D}}{\partial t} \,, \qquad (2.1.2)$$

$$\text{Faraday's law of induction} \qquad \nabla \times \vec{E} = -\frac{\partial \vec{B}}{\partial t} \,, \qquad (2.1.3)$$

$$\text{absence of magnetic monopoles} \qquad \nabla \cdot \vec{B} = 0 \,. \qquad (2.1.4)$$

These four equations relate electric field $\vec{E}$, electric displacement or electric flux density $\vec{D}$, magnetic field $\vec{H}$, magnetic flux density $\vec{B}$, electric current density $\vec{J}$ and charge density ρ, which in general depend on space and time. Apparently, this work discusses propagation in water or free space. Therefore, it is sufficient to restrict the derivations in this overview to linear, isotropic and homogeneous media.

The material equations describe the connection between the different electric as well as magnetic field quantities. While the permittivity ε relates the electric field to the

displacement by

$$\vec{D} = \varepsilon \vec{E}\,, \tag{2.1.5}$$

the permeability μ relates magnetic field and magnetic flux density by

$$\vec{B} = \mu \vec{H}\,. \tag{2.1.6}$$

The quantities ε and μ account for effects of the electric and/or the magnetic fields on a propagation medium, such as polarisation or magnetisation, and equal ε_0 and μ_0 in vacuum. For anisotropic materials ε and μ are tensors of second order.

Examining equation (2.1.2) more closely shows an additional term including the time derivative of the displacement compared to the original law of Ampère. In magnetostatics, where Ampère's law relates magnetic field and electric current density, the relation $\nabla \cdot \vec{J} = 0$ is valid. However, the continuity equation

$$\nabla \cdot \vec{J} + \frac{\partial \rho}{\partial t} = 0 \tag{2.1.7}$$

is mandatory in electrodynamics. Thus, equation (2.1.7) combined with Coulomb's law of equation (2.1.1) modifies the original law of Ampère.

2.2 Potentials

In electrostatics $\left(\frac{\partial \vec{B}}{\partial t} = 0 \right)$ Faraday's law

$$\nabla \times \vec{E} = 0 \tag{2.2.1}$$

allows the definition of a scalar potential whose gradient is the electric field. The difference of the scalar potential between two points in space denotes the voltage. In the electrodynamic case Faraday's law contains the time derivative of the magnetic flux density. Thus, the electric field is no longer irrotational. However, equation (2.1.4) permits the definition of a vector potential $\vec{A}$ with

$$\nabla \times \vec{A} = \vec{B}\,. \tag{2.2.2}$$

Inserting this relation into Faraday's law yields

$$\nabla \times \left(\vec{E} + \frac{\partial \vec{A}}{\partial t} \right) = 0\,. \tag{2.2.3}$$

This equation again is analogous to the static Faraday's law (2.2.1), thus there exists a scalar potential Ψ with

$$\vec{E} + \frac{\partial \vec{A}}{\partial t} = -\nabla \Psi\,. \tag{2.2.4}$$

Combining equation (2.2.4), the material equation for the electric field (2.1.5) and Coulomb's law (2.1.1) returns

$$\nabla^2 \Psi + \frac{\partial}{\partial t}(\nabla \cdot \vec{A}) = -\frac{\rho}{\varepsilon}\,. \tag{2.2.5}$$

In the following, the Laplace operator Δ replaces the square of the Nabla operator ∇^2. Applying equations (2.1.5), (2.1.6), (2.2.2) and (2.2.4) to the modified Ampère's law and using the vector relation

$$\nabla \times (\nabla \times \vec{a}) = \nabla(\nabla \cdot \vec{a}) - \Delta \vec{a} \tag{2.2.6}$$

gives

$$\nabla(\nabla \cdot \vec{A}) - \Delta \vec{A} + \mu \varepsilon \nabla \frac{\partial \Psi}{\partial t} + \mu \varepsilon \frac{\partial^2}{\partial t^2} \vec{A} = \mu \vec{J} \tag{2.2.7}$$

or, rearranged

$$\Delta \vec{A} - \mu \varepsilon \frac{\partial^2}{\partial t^2} \vec{A} - \nabla(\nabla \cdot \vec{A} + \mu \varepsilon \frac{\partial \Psi}{\partial t}) = -\mu \vec{J}\,. \tag{2.2.8}$$

The definition of the speed of light (in medium) $c = \frac{1}{\sqrt{\mu \varepsilon}}$ abbreviates equation (2.2.8).

2.3 Gauge Transformations and Wave Equation

The definition of $\vec{A}$ by equation (2.2.1) leaves a degree of freedom. Thus, the Coulomb gauge simplifies equation (2.2.5) by setting

$$\nabla \cdot \vec{A} = 0\,. \tag{2.3.1}$$

Alternatively equation (2.2.8) motivates the definition of the Lorenz gauge

$$\nabla \cdot \vec{A} + \frac{1}{c^2} \frac{\partial \Psi}{\partial t} = 0\,, \tag{2.3.2}$$

which decouples equations (2.2.5) and (2.2.8) yielding the inhomogeneous wave equations for the scalar and the vector potential

$$\Delta \Psi - \frac{1}{c^2} \frac{\partial^2 \Psi}{\partial t^2} = -\frac{\rho}{\varepsilon} \tag{2.3.3}$$

and

$$\Delta \vec{A} - \frac{1}{c^2} \frac{\partial^2 \vec{A}}{\partial t^2} = -\mu \vec{J}\,. \tag{2.3.4}$$

As mentioned before, the sources on the right-hand side of both equations and the potentials may depend on time and space.

2.4 The Homogenous Helmholtz Equation and its Solutions

Assuming a mono-frequent time dependence of the scalar potential Ψ

$$\Psi(t, \vec{r}) = \Psi_0(\vec{r})e^{j\omega t} \tag{2.4.1}$$

with the angular frequency ω transforms the homogeneous constituent of the scalar wave equation (2.3.3) which reads

$$\Delta\Psi - \frac{1}{c^2}\frac{\partial^2\Psi}{\partial t^2} = 0 \tag{2.4.2}$$

into

$$\Delta\Psi_0 - \frac{(j\omega)^2}{c^2}\Psi_0 = 0\,. \tag{2.4.3}$$

Substituting $\frac{\omega}{c}$ with the wave number k yields the scalar Helmholtz equation

$$\Delta\Psi_0 + k^2\Psi_0 = 0 \tag{2.4.4}$$

and in analogy the vector Helmholtz equation from equation (2.3.4)

$$\Delta\vec{A} + k^2\vec{A} = 0\,. \tag{2.4.5}$$

Following Stratton (2007) three independent vectors based on the solution of the scalar Helmholtz equation (2.4.4) and a constant vector $\vec{a}$ solve the vector Helmholtz equation (2.4.5). These solutions are

$$\vec{L} = -\nabla\Psi_0\,, \tag{2.4.6}$$

$$\vec{M} = -\vec{a} \times \nabla\Psi_0 \qquad \text{and} \tag{2.4.7}$$

$$\vec{N} = \frac{1}{k}\nabla \times \vec{M}\,. \tag{2.4.8}$$

The knowledge of the solution of the homogeneous Helmholtz equation allows construction of the particular solution of $\vec{A}$ derived from the wave equation (2.3.4) by the series ansatz

$$\Psi_0 = \sum_n c_n\Psi_n \tag{2.4.9}$$

for the scalar potential and

$$\vec{A} = \frac{1}{j\omega} \sum_n (a_n \vec{M}_n + b_n \vec{N}_n + c_n \vec{L}_n) \tag{2.4.10}$$

for the vector potential.

Finally, equation (2.2.4) combines scalar and vector potential as well as equation (2.2.4) resulting in the electric field

$$\begin{aligned}
\vec{E} &= -\nabla \Psi_0 - \frac{\partial \vec{A}}{\partial t} \\
&= \sum_n c_n \vec{L}_n - j\omega \frac{1}{j\omega} \sum_n (a_n \vec{M}_n + b_n \vec{N}_n + c_n \vec{L}_n) \\
&= -\sum_n (a_n \vec{M}_n + b_n \vec{N}_n) \,.
\end{aligned} \tag{2.4.11}$$

Furthermore, applying the current free version of equation (2.1.2) returns the magnetic field

$$\begin{aligned}
\vec{H} &= \frac{j}{\omega \mu} \nabla \times \vec{E} \tag{2.4.12} \\
&= -\frac{jk}{\omega \mu} \sum_n (a_n \vec{N}_n + b_n \vec{M}_n) \,. \tag{2.4.13}
\end{aligned}$$

3 The Physical Structure of Rain

Within PROCEMA precipitation is measured using point-to-point links. Globally the most dominant type of precipitation is rain, which is the subject of interest in this work. This chapter illustrates different aspects concerning rain specific attributes. Section 3.1 deals with the individual particles of rain, namely the rain drops. Two parameters of particular interest are the drop shape and the motions of the drops in natural rain. Afterwards, this section describes models for the refractive index of water influencing the propagation of electromagnetic waves.

Rain ranges from light drizzle to monsoon-like rates, although the latter is rare in central European countries. Section 3.2 investigates these rain types and their corresponding rain rates. The drop size distribution, explained afterwards, depends on both of these characteristics. The properties presented in this chapter serve as input for investigations about the influence of rain fields on microwaves.

3.1 Rain Drop Parameters

3.1.1 Drop Shape

When people think about a rain or a tear drop, they imagine a certain shape usually referred to as "drop". However, this image is incorrect for rain. Measurements shown in figure 3.1 illustrate a contour that can be described as Hamburger shaped, i. e. an oblate spheroid with flattened base. However, mechanical forces such as hydrostatic pressure, outlined in section 3.1.1, acting on the rain drops split them for radii larger than 4 mm.

Szakáll et al. (2009) recorded video sequences of falling drops and compared the observed shapes with already established models. Raindrops up to a radius of 1 mm are typically approximated by spheres. More complex shapes, such as given in the following, better describe drops exceeding this size limit (Oguchi 1983).

Spherical

A very simple shape, which is valid for small drops up to a diameter of 0.3 cm, according to Andsager, Beard, and Laird (1999), is a simple sphere. Furthermore, this shape can be used as first order approximation for larger drops. In 1908, Gustav Mie presented an approach for the scattering of microwaves by spheres (Mie 1908). This work outlines this widely known theory in section 4.1.3. Although the spherical model may be inaccurate
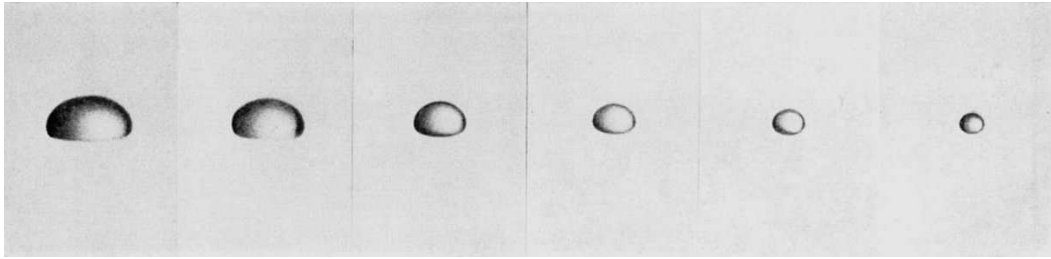
Figure 3.1: Photo series of drops with equivolume radii of 4.00 mm, 4.675 mm, 2.90 mm, 1.725 mm and 1.35 mm (taken from Pruppacher and Beard (1970)).

due to its neglect of any deformation of the drop, it is often applied and serves as initial model for this present work. Simulations implementing this simple shape already yield considerable information about the influence of rain on electromagnetic waves.

Spheroidal Shape

A further step towards advanced shapes away from the simple spherical shape leads to an oblate spheroidal contour. The recipe to calculate scattering by spheroids resembles Mie theory. While Mie theory derives the solution of the Helmholtz equation in spherical coordinates, spheroidal shapes are best solved in a boundary adopted system. The solution to the spherical problem is composed by a polynomial expansion of the spherical functions. Unlike for spheres, which are rotationally invariant, canting of spheroidal drops (compare section 3.1.3) varies the drops position in space.
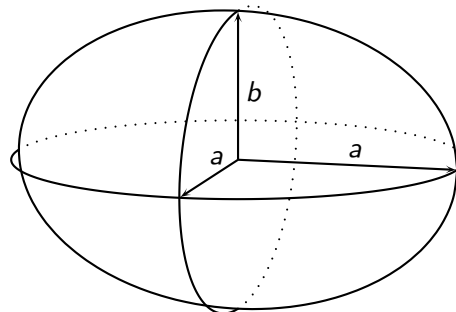
Figure 3.2: Image of an oblate spheroid with the major semi-axes *a* and *b*.

Tchebycheff Shape

For large drops, the ratio α of the semi-axes *a* and *b* (see Figure 3.2) extends according to Andsager, Beard, and Laird (1999) between $3/4$ and 1 where a ratio of 1 denotes a spherical shape. Andsager, Beard, and Laird (1999) combined data from measurements and those published by other groups. A comparison of this data with models for the

axis ratio showed that the models by Beard and Chuang (1987), Goddard and Cherry (1984) and a model composed by the group itself matched the data accurately. In contrast, the formulation suggested by Pruppacher and Beard (1970) differs from the measurements.

The model proposed by Beard and Chuang (Beard and Chuang 1987; Chuang and Beard 1990) balances influencing forces to derive the drop shape. These forces are surface tension, hydrostatic and aerodynamic pressure, internal circulation and electric stress resulting in a semi-axis ratio of

$$\alpha_N = 1.0048 + 0.0057D - 2.628D^2 + 3.682D^3 - 1.6177D^4 \tag{3.1.1}$$

with the equivolume diameter D in cm. Szakáll et al. (2009) and Leijnse (2007) proposed to use this model to describe rain drops as spheroids.

The aforementioned model by Goddard and Cherry (1984) is derived from radar disdrometer measurements. Andsager, Beard, and Laird (1999) present a model giving the mean axis ratio considering oscillation of rain drops as

$$\alpha_A = 1.012 - 0.1442D - 1.03D^2 \,. \tag{3.1.2}$$

Further information on the oscillation is considered in section 3.1.3.

Pruppacher and Pitter (1971) proposed a semi empirical model evaluated by the perturbation approach. This theory describes a sphere with perturbed radius

$$r_p = r_0(1 + \delta f_1(\theta, \varphi) + \delta^2 f_2(\theta, \varphi) + \dots) \tag{3.1.3}$$

manipulating the unperturbed spherical radius r_0 with variations f of order δ in the spherical coordinates θ and φ. Tchebycheff polynomials for the radius with matching coefficients c_n describe both the Pruppacher and Pitter as well as Beard and Chuang shape model in the form of

$$r = r_0 \left[1 + \sum_{n=0}^{\infty} c_n \cos(n\theta) \right] \,. \tag{3.1.4}$$

In summary, this subsection listed potential realisations to authentically model rain drops. While Tchebycheff polynomials are able to represent spheroidal or advanced contours like the Hamburger shape, most publications and also this work apply Mie theory related to spherical shapes due to its handability.

3.1.2 Drop Medium

The refractive index of a dielectric medium m changes propagation attributes of penetrating waves. This subsection introduces two models for the refractive index of water. Both models describe the dependence of the refractive index on frequency and temperature. While the influence of frequency is significant, the effect of temperature is less important. Oguchi (1983) cites measurements at 60 GHz for two temperature ranges

from 2 °C to 5 °C as well as from 25 °C to 28 °C showing negligible impact on the refractive index. Additionally, Setijadi et al. (2009) analysed this relation in theory, yielding analogue results.

Electromagnetics commonly deals with the permittivity ϵ_r related to the refractive index by

$$m = \sqrt{\varepsilon_r}\,. \tag{3.1.5}$$

Ray (1972) as well as Liebe, Hufford, and Manabe (1991) described the permittivity by models derived from the standard Debye model. Both verified their models with published measurements. The Debye model expresses the permittivity depending on frequency,

$$\varepsilon_D(f) = \frac{\varepsilon_0 - \varepsilon_\infty}{1 + \mathrm{j}\frac{f}{\gamma_D}} + \varepsilon_\infty \tag{3.1.6}$$

with ε_0 denoting the static and ε_∞ the high frequency permittivity. γ_D denotes the relaxation frequency.

Ray (1972) evaluates real and imaginary parts accordint to $\varepsilon_r = \varepsilon' - \mathrm{j}\epsilon''$ of the Debye model to be

$$\varepsilon' = \varepsilon_\infty + \frac{(\varepsilon_s - \varepsilon_\infty)[1 + (\lambda_s/\lambda)^{1-\alpha}\sin(\alpha\pi/2)]}{1 + 2(\lambda_s/\lambda)^{1-\alpha}\sin(\alpha\pi/2) + (\lambda_s/\lambda)^{2(1-\alpha)}} \tag{3.1.7}$$

and

$$\varepsilon'' = \frac{(\varepsilon_s - \varepsilon_\infty)(\lambda_s/\lambda)^{1-\alpha}\cos(\alpha\pi/2)}{1 + 2(\lambda_s/\lambda)^{1-\alpha}\sin(\alpha\pi/2) + (\lambda_s/\lambda)^{2(1-\alpha)}} + \frac{\sigma\lambda}{18.8496 \cdot 10^{10}} \tag{3.1.8}$$

using the conductivity σ, the spread parameter α and the relaxation wavelength λ_s related to γ_D by $\lambda_s = {2\pi}/{\gamma_D}$.

The variables partially depending on temperature T (in °C) are

$$\sigma = 12.5664 \cdot 10^8 \,{}^1\!/_\mathrm{m}\,, \tag{3.1.9}$$

$$\alpha(T) = -\frac{16.8129}{T + 273} + 0.0609265\,, \tag{3.1.10}$$

$$\varepsilon_\infty(T) = 5.27137 + 0.0216474\,T - 0.00131198\,T^2\,, \tag{3.1.11}$$

$$\varepsilon_s(T) = 78.54[1.0 - 4.579 \cdot 10^{-3}(T - 25.0) + 1.19 \cdot 10^{-5}(T - 25.0)^2$$
$$- 2.8 \cdot 10^{-8}(T - 25.0)^3]\,, \tag{3.1.12}$$

$$\lambda_s(T) = 0.00033836\exp\left(\frac{2513.98}{T + 273}\right)\mathrm{cm}\,. \tag{3.1.13}$$

Figure 3.3 illustrates real and imaginary parts of ϵ_r.

Liebe, Hufford, and Manabe (1991) describe an advanced model plotted in figure 3.4
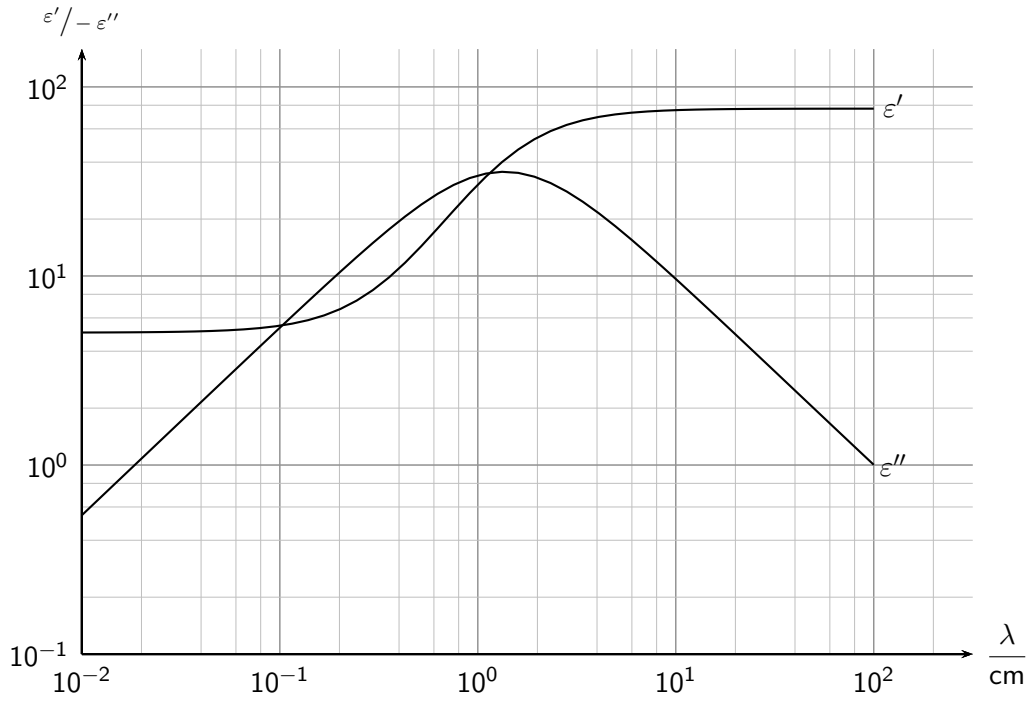
Figure 3.3: Plot of real (ε') and imaginary parts (ε'') of the permittivity over wavelength according to Ray (1972) at 30 °C.

based on equation (3.1.6) with

$$\varepsilon_0(\vartheta) = 77.66 - 103.3\vartheta\,, \tag{3.1.14}$$

$$\varepsilon_\infty(\vartheta) = 0.066 \cdot \varepsilon_0\,, \tag{3.1.15}$$

$$\gamma_D(\vartheta) = 20.27 + 146.5 \cdot \vartheta + 314\vartheta^2 \qquad \text{(in GHz)}\,. \tag{3.1.16}$$

introducing the temperature dependent parameter

$$\vartheta(T) = 1 - \frac{300}{273.15 + T}\,. \tag{3.1.17}$$

The refractive index significantly modifies wave properties inside a medium. The two presented theoretical models by Ray (1972) and Liebe, Hufford, and Manabe (1991) serve for calculations of this quantity.

3.1.3 Drop Motion

The subject of drop motion is of great importance in this work. In most publications, the authors consider a rain field to be a static statistical medium. Nevertheless, rain motion occasionally is included in derivations of the Doppler spectrum. This work explicitly considers the individual spatial variation of drops, for instance caused by gravitational
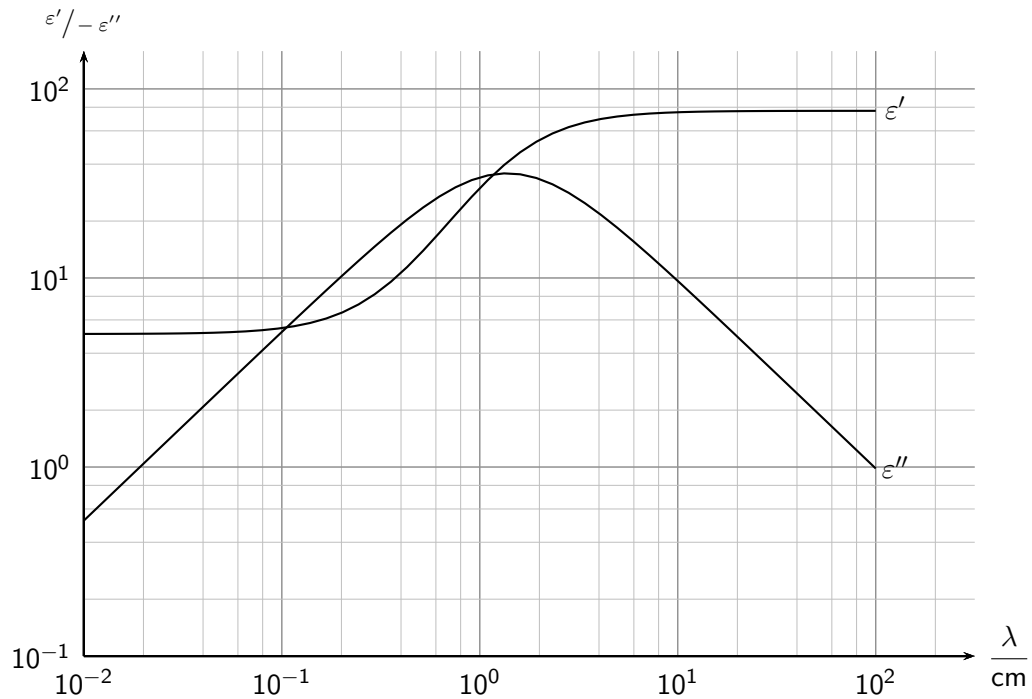
Figure 3.4: Plot of real (ε') and imaginary part (ε'') of the permittivity over wavelength according to Liebe, Hufford, and Manabe (1991) at 30 °C.

forces or wind. Furthermore, drops are observed to cant while falling and to oscillate internally.

The dominant motion results from gravitational forces. Gunn and Kinzer (1949) modelled the terminal velocity v of drops as

$$v(r) = 615.109 \cdot r^{0.67} \qquad \text{(in m/s)} \tag{3.1.18}$$

with radius r in m. Figure 3.5 illustrates the given equation. This work disregarded any influence of atmospheric pressure, humidity and temperature on the terminal fall velocity.

During normal conditions, wind in central Europe observes a velocity in the range from 0 km/h to 13 km/h on average. For instance, the windfinder website (*Windfinder - Wind Statistics Map Europe* (2012): `http://www.windfinder.com`) lists a mean wind speed in Munich of 11 km/h between 2009 and 2012. Wind velocities reach up to 335 km/h, as observed on the mount Zugspitze in 1985 (*Deutscher Wetterdienst: Weather Extremes - Wind* (2012): `http://www.dwd.de`).

Influenced by wind and normal decline, drops start to cant. Canting possibly affects the phase of the incident waves. A Gaussian curve describes the distribution of the
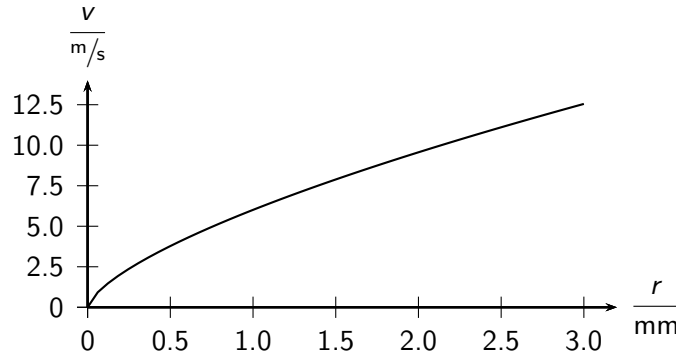
Figure 3.5: Plot of terminal velocity depending on radius according to Gunn and Kinzer (1949).

canting angles δ as

$$t(\delta) = \frac{1}{\sigma_\delta \sqrt{2\pi}} \exp\left(-\frac{(\delta - \bar{\delta})^2}{2\sigma_\delta^2}\right) . \tag{3.1.19}$$

Several groups observed the mean angle $\bar{\delta}$ to be zero (Marzano, Botta, and Montopoli 2010; Oguchi 1983) or near zero (Leijnse 2007; Russchenberg and Ligthart 1992). These groups published standard deviations σ_δ between 5° and 12°. A physical model by Brussaard (1976) and Russchenberg and Ligthart (1992), relates the canting of one drop to vertical variations in horizontal wind fields (= wind shear). Here, the canting angle is calculated as

$$\tan(\delta) = \frac{vU_v}{g} \tag{3.1.20}$$

with the fall velocity v, the gravitation constant g and the height gradient U_v which is small above 100 m. Additionally, an article published by Beard and Jameson (1983) specialises on raindrop canting. Beard and Jameson (1983) varied Brussards model to account for alternating wind shear and compared this theory with microwave, especially radar, measurements.

A fourth movement likely to influence a passing electromagnetic wave is internal oscillation. Szakáll et al. (2009) studied oscillation of rain drops in wind tunnel measurements. They observed frequencies of oscillations and internal circulation. Oguchi (1983) cites Hasworth et al. who examined Doppler spectra concerning the vibration of raindrops. Hasworth et al. observed frequency components due to these oscillations above those commonly detected in the spectrum such as the Doppler broadening effected by the fall velocity. Andsager, Beard, and Laird (1999) derived a model for the mean axis ratio around which the drop oscillates (compare equation (3.1.2)).

Additional to the obvious sources of motion, gravitation and wind, rain drops observe unfamiliar dynamics. All motion types affect or are expected to affect the propagation

of microwaves.

3.2 Rain Field Parameters

3.2.1 Rain Types

This section deals with the assembly of individual rain drops to compose a rain field. Since rain drops develop in clouds, the corresponding rain field inherits the name of it source type: stratiform or convective rain. Fiser and Rezacova (2007) depict stratiform rain as widespread rainfall with long duration. This type develops in horizontally extended clouds and exhibits a moderate rain rate. Convective rain denotes local heavy rainfall lasting 10 min to 1 h. Convective clouds, which reach a large vertical extension produce this type of precipitation. The classification of both rain types individually depends on their location. While in European countries large rain drops indicate convective rain, tropical rain shows the opposite behaviour. Furthermore, different DSDs express the radii of drops belonging to both rain types. Even equal rain rates may have different distributions depending on their origin.

3.2.2 Rain Rate

Rain rate is the most familiar measure for rain. This value is both made public by the weather services and used by scientists of weather-related subjects. Table 3.1 classifies different rain rates together with their common terms. DSD (see next subsection) and

rain rate	
0.25	drizzle
1	light rain
4	moderate rain
16	heavy rain
100	extremely heavy rain

Table 3.1: Rain categories and corresponding rates in $^{mm}/_h$.

terminal velocity calculate the rain rate R in $^{mm}/_h$ (Ishimaru 1997; Townsend, Watson, and Hodges 2009)) by

$$R = 3600 \cdot 10^3 \cdot \frac{4\pi}{3} \int_0^\infty v(r) r^3 n(r) dr \,, \tag{3.2.1}$$

with radius r in m, DSD $n(r)$ in $^1/_{m^3\,m}$ and terminal velocity $v(r)$ from equation (3.1.18) in $^m/_s$. Different models of DSDs thus may yield the same rain rate (Oguchi 1983).

Name	N_0 in $1/\text{m}^3\,\text{m}$	Λ in $1/\text{m}$	used for R
Marshall and Palmer (1948)	$16 \cdot 10^6$	$8.2 \cdot 10^3\ R^{-0.21}$	$\leq 100\,\text{mm}/\text{h}$
Laws and Parsons (1943)	$102 \cdot 10^6$ $R^{-0.03}$	$7.6 \cdot 10^3\ R^{-0.20}$	widespread, R low convective, R high
Joss-Drizzle	$60 \cdot 10^6$	$11.4 \cdot 10^3\ R^{-0.21}$	$< 5\,\text{mm}/\text{h}$
Joss-Widespread	$14 \cdot 10^6$	$8.2 \cdot 10^3\ R^{-0.21}$	
Joss-Thunderstorm	$28 \cdot 10^6$	$6 \cdot 10^3\ R^{-0.21}$	$\leq 150\,\text{mm}/\text{h}$

Table 3.2: Various exponential DSD parameter choices according to Oguchi (1983); Aydin and Lure (1991), for an overview of the Joss Models see Joss, Thams, and Waldvogel (1968).

3.2.3 Drop Size Distribution

The drop size distribution (DSD) describes the number of drops per drop radius in a given volume. The most commonly used type is the exponential distribution implying a large number of small drops and a few large ones. The distribution is written as

$$n(r) = N_0 \exp(-\Lambda r) \tag{3.2.2}$$

with the drop radius r in m. The parameters N_0 and Λ possibly depend on the rain rate R in mm/h (see preceding section). The median drop size r_0 is derived by $r_0 = 3.67/\Lambda$ (Russchenberg and Ligthart 1992). Most publications employ the Marshall-Palmer (MP) distribution. Table 3.2 lists N_0 and Λ used within equation (3.2.2) describing the MP or other distributions used for differing types of rain.

Integration of equation (3.2.2) leads to the total number N of drops in a volume V_{fill} as

$$N = \frac{N_0}{\Lambda} V_{\text{fill}} \,. \tag{3.2.3}$$

Nowadays measurements of drop sizes are extrapolated with enhanced distributions like the Gamma distribution (Ulbrich 1983; Zhang, Vivekanandan, and Brandes 2001; Schleiss, Berne, and Uijlenhoet 2009), written in general as

$$n(r) = N_0 r^\mu \exp(-\Lambda r) \,, \tag{3.2.4}$$

the normalised Gamma distribution (Townsend, Watson, and Hodges 2009)

$$n(r) = N_0 \frac{6}{4^4} \left[\frac{(4+\mu)^{4+\mu}}{\Gamma(4+\mu)} \right] \cdot \left(\frac{r}{r_m} \right)^\mu \cdot \exp\left[-(4+\mu) \cdot \frac{r}{r_m} \right] \tag{3.2.5}$$

or a lognormal distribution. These distributions gave a more accurate description of the real drop size distribution. Especially they solve the former problem of the overes-

timation of the number of small drops with exponential approaches.

Disdrometers determine DSDs of hydrometeors during a rain event in real time. Modern systems operate in the optical regime (Rogers 1976). Furthermore, since the terminal velocity (equation (3.1.18)) varies with drop size, Doppler spectra of electromagnetic signals show the size distribution by applying this relation of drop radius to terminal velocity.

Ulbrich (1983) presents a method to derive rain characteristics with the pth moment of the radius in combination with the drop size distribution

$$P = a_p \int_0^\infty r^p n(r) dr \,.$$

(3.2.6)

This integration leads to meteorological and scattering related characteristics using the moment p and the normalisation parameter a_p listed in table 3.3.

rain characteristic	P	p	a_p
radar reflectivity factor (mm^6/m^3)	Z	6	$2 \cdot 10^6$ mm^6/cm^6
liquid water content (g/m^3)	W	3	1.048 g/cm^3
optical extinction ($1/km$)	Σ	2	0.314 $m^3/km\,cm^2$
rainfall rate (mm/h)	R	3.67	66.62 $mm{\cdot}m^3/h/cm^{3.67}$
Microwave attenuation ($1/km$)	A	n	$0.4343 C_A$ $m^3/km/cm^n$

Table 3.3: Moments of radius and normalisation parameters to derive special rain characteristics applying equation (3.2.6)

The assembly of individual rain drops creates a rain field. The occurrence of a rain field is called rain event, which may be characterised by the three measures as explained in detail in the previous section.

A coarse classification results from the type of clouds emitting the rain, leading to stratiform and convective rain. Moreover, the rain rate used in everyday life expresses a finer categorisation of rain. It describes the amount of rain per time interval. Finally, the DSD, the distribution of drop radii, yields a detailed description of rain in a certain time interval. Rain rate and DSD vary during the rain event, especially in the beginning and towards the end of the rain event.

4 Microwave Scattering in Rain Fields

Rain influences the propagation of electromagnetic waves. Each individual rain drop contributes to the total perturbation of the waves. This disturbance of the incident electromagnetic waves by obstacles is called scattering. The goal of this work is to investigate the scattering mechanisms effected by the drops when a wave propagates through rain.

In order to understand the underlying physical effects, section 4.1 explains general mechanisms of scattering. Afterwards, the section illustrates the special case of scattering by a sphere and introduces the concept of coherent and incoherent scattering.

Section 4.2 derives the coherent scattered field of waves propagating through a rain field resulting in calculations for feasible estimates of attenuation and phase influences. In addition, the section sheds light on multiple scattering and alternative modelling methods.

The very next section extends the scattering basics given in section 4.1 towards scattering at rain drops. This mechanism happening on drop scale accumulates to the incoherent part of the total signal. Finally, this chapter verifies computations performed using the numerical implementation in MATLAB with results from commercial field solvers.

4.1 Electromagnetic Scattering

This section introduces the scattering by an arbitrary object. After deriving absorption and extinction of the scattering object, the energy passing through the scatterer helps to define cross sections. These relate a specified energy to the the incident energy.

The second subsection describes the scattering matrix relating the different polarisations of incident and scattered electromagnetic waves. This matrix serves for the derivations of the cross sections defined before. These calculations are concluded by applying the equations derived in this chapter to the spherical rain drops. Finally, section 4.1.4 introduces the concept of coherent and incoherent scattering.

4.1.1 Scattering Principles

Incident plane waves[1] in free space with angular frequency ω and free space wave vector $\vec{k}_0$ are denoted as

$$\vec{E}_{\mathrm{i}}(\vec{r}, t) = \vec{E}_0 e^{\mathrm{j}(\omega t - \vec{k}_0 \cdot \vec{r})} \tag{4.1.1}$$

with the amplitude $|\vec{E}_0|$ and a polarisation direction $\widehat{E}_0$, where the hat denotes the unit vector of the appropriate electric field vector $\vec{E}_0$. Frequency f and wavelength λ are related to angular frequency and wave number by $f = {}^\omega\!/_{2\pi}$ and $\lambda = {}^{2\pi}\!/_{k_0}$. The absolute value of the wave vector $|\vec{k}_0| = k_0$ denotes the propagation constant. Electromagnetic waves in free space proceed with the speed of light $c_0 = {}^1\!/_{\sqrt{\varepsilon_0 \mu_0}}$ relating frequency and wavelength by $\lambda = {}^{c_0}\!/_f$. This work omits the time dependence of the wave for comprehensibility, all further equations are based on single frequency waves.

The electric field of spherical waves under farfield conditions originating from a source point decreases in space with $^1\!/_r$ (van Bladel 2007) yielding

$$\vec{E}_{\mathrm{i}}(\vec{r}) = \vec{E}_0 \frac{e^{-\mathrm{j}\vec{k}_0 \cdot \vec{r}}}{|\vec{r}|} \ . \tag{4.1.2}$$

An object inside a volume affects a propagating electromagnetic wave by the constitution of the "scattered field" which is defined as illustrated in the following. The left image of figure 4.1 shows the field distribution including a scattering object. This field is called the total field $\vec{E}_{\mathrm{t}}$. The second image gives the incident field $\vec{E}_{\mathrm{i}}$ passing the volume without disturbance. To obtain the scattered field $\vec{E}_{\mathrm{s}}$, the incident field is subtracted from the total field. Mishchenko (2008) issues the theoretical background of the mathematical conception of this scattered field. From a signal point of view, it denotes the response of the system to the incident waves.

Consequently, to understand the principle of scattered waves the derivation of the expression for the field scattered by a single particle is illustrated in Figure 4.2, following

Field including scatterer   Field without disturbance

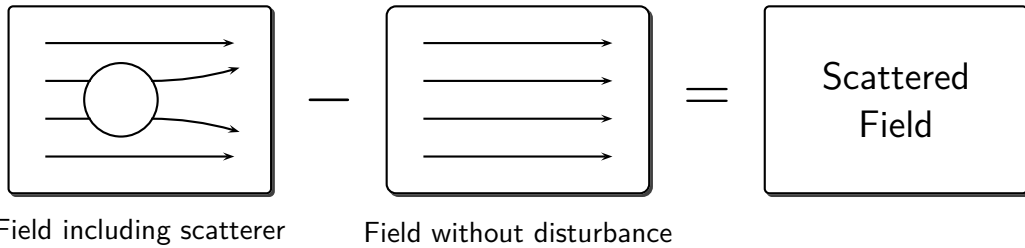Figure 4.1: Illustration of the subtraction of the incident field from the total field yielding the scattered field.

---

[1]In the following, this work uses the notation common in electrical engineering for electric fields and waves. In physics the field mathematically turns reverse $e^{\mathrm{i}(kr - \omega t)}$. Therefore, the imaginary unit j is the negative of i. Please note: The refractive index changes accordingly.

Ishimaru (1997) and others (Ishimaru 1997; van Bladel 2007; Stratton 2007; Bohren and Huffman 1983; Kerker 1969; van de Hulst 1981).

If one assumes an object to be located at a distance r_k from the receiver, the field incident on this object is given in analogy to equation (4.1.2) by

$$\vec{E}_{\text{i}}(\vec{r}_k) = \vec{E}_0 \frac{e^{-\text{j}\vec{k}_0 \cdot \vec{r}_k}}{r_k} \,. \tag{4.1.3}$$

To derive the influence of the drop on the incident waves, the Helmholtz equation has to be solved. This leads to the scattering amplitude or radiation vector $\vec{f}_k(\widehat{k}_0, \widehat{k}_k)$, relating the incident field amplitude for a wave propagating along the direction $\widehat{k}_0$ to the amplitude and phase of the scattered field propagating in $\widehat{k}_k$ direction with $\widehat{k}_0$ and $\widehat{k}_k$ denoting the unit vectors in the appropriate directions. In the farfield region, waves emitted from the object may be approximated as spherical waves, thus leading to

$$\vec{E}_{\text{s}}(\vec{r}) = \vec{f}_k(\widehat{k}_0, \widehat{k}_k) \frac{e^{-\text{j}\vec{k}_k \cdot (\vec{r} - \vec{r}_k)}}{|\vec{r} - \vec{r}_k|} E_{\text{i}} \tag{4.1.4}$$

$$= \vec{f}_k(\widehat{k}_0, \widehat{k}_k) \frac{e^{-\text{j}(\vec{k}_0 \cdot \vec{r}_k + \vec{k}_k \cdot (\vec{r} - \vec{r}_k))}}{r_k |\vec{r} - \vec{r}_k|} E_0 \tag{4.1.5}$$

for the expression of the scattered field at the point of the receiver.

In the case of spherical waves, the wave vector $\vec{k}_k$ always is parallel to any vector starting at the origin of the object (compare with figure 4.2). The value of the propagation constant remains fixed if scattering by the corresponding object leaves the frequency unchanged. Therefore, equation (4.1.4) (Oguchi 1983) is modified by using the moduli of the vectors

$$\vec{E}_{\text{s}}(\vec{r}) = \vec{f}_k(\widehat{k}_0, \widehat{k}_k) \frac{e^{-\text{j}(\vec{k}_0 \cdot \vec{r}_k + k_0 |\vec{r} - \vec{r}_k|)}}{r_k |\vec{r} - \vec{r}_k|} E_0 \,. \tag{4.1.6}$$

The scattering system may be extended by taking the antennas for transmission and reception into account. Thus, the equations need to be extended by considering the field pattern of transmission and receiving antenna.
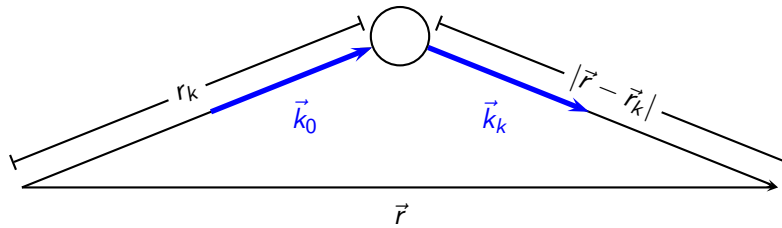

Figure 4.2: Image of field and space vectors of incident waves and the waves scattered by an object.

Energy Flux

While the energy of undisturbed waves passes the considered volume without interference, an object inside the volume alters the energy flow. Berg, Sorensen, and Chakrabarti (2008a); Ishimaru (1997); Kerker (1969); Stratton (2007); van Bladel (2007) as well as Bohren and Huffman (1983) calculated the energy flow per unit area of the propagating waves in the farfield region using the time dependent Pointing vector

$$\vec{S}(t) = \vec{E}(t) \times \vec{H}(t) \,. \tag{4.1.7}$$

Applying the assumption of mono-frequent waves, the omission of time dependence and averaging over intensity results in the time-averaged Pointing vector denoting the energy flux

$$\vec{S} = \frac{1}{2} \Re(\vec{E} \times \vec{H}^*) \,. \tag{4.1.8}$$

Ishimaru (1997) calculated the incident and scattered Pointing vectors utilising the free space impedance $Z_0 = \sqrt{\varepsilon_0/\mu_0}$, which relates the amplitudes of magnetic and electric field in vacuum. Thus,

$$\vec{S}_\mathsf{i} = \frac{1}{2} \Re(\vec{E}_\mathsf{i} \times \vec{H}_\mathsf{i}^*) = \frac{|\vec{E}_\mathsf{i}|^2}{2Z_0} \widehat{k}_0 \overset{(4.1.3)}{=} \frac{1}{2Z_0} \frac{|E_0|^2}{r_k^2} \widehat{k}_0 \tag{4.1.9}$$

and

$$\begin{aligned}
\vec{S}_\mathsf{s} &= \frac{1}{2} \Re(\vec{E}_\mathsf{s} \times \vec{H}_\mathsf{s}^*) = \frac{|\vec{E}_\mathsf{s}|^2}{2Z_0} \widehat{k}_k \\
&\overset{(4.1.4)}{=} \frac{1}{2Z_0} \frac{|\vec{f}_k(\widehat{k}_o, \widehat{k}_k)|^2}{|\vec{r} - \vec{r}_k|^2} |\vec{E}_\mathsf{i}|^2 \widehat{k}_k = \frac{E_0^2}{2Z_0} \frac{|\vec{f}_k(\widehat{k}_0, \widehat{k}_k)|^2}{r_k^2 |\vec{r} - \vec{r}_k|^2} \widehat{k}_k \,.
\end{aligned} \tag{4.1.10}$$

Applying spherical vector components, the radial component of the Pointing vector of the total field is given by

$$S_{\mathsf{t},r} = \frac{1}{2} \left(E_{\mathsf{t},\theta} H_{\mathsf{t},\varphi}^* - E_{\mathsf{t},\varphi} H_{\mathsf{t},\theta}^* \right) \,. \tag{4.1.11}$$

Separating this radial component into incident and scattered field ($\vec{E}_\mathsf{t} = \vec{E}_\mathsf{i} + \vec{E}_\mathsf{s}$, as illustrated in figure 4.1) yields

$$\begin{aligned}
S_{\mathsf{t},r} =\ & \frac{1}{2} \Re(E_{\mathsf{i},\theta} H_{\mathsf{i},\varphi}^* - E_{\mathsf{i},\varphi} H_{\mathsf{i},\theta}^*) \\
& + \frac{1}{2} \Re(E_{\mathsf{s},\theta} H_{\mathsf{s},\varphi}^* - E_{\mathsf{s},\varphi} H_{\mathsf{s},\theta}^*) \\
& + \frac{1}{2} \Re(E_{\mathsf{i},\theta} H_{\mathsf{s},\varphi}^* + E_{\mathsf{s},\theta} H_{\mathsf{i},\varphi}^* - E_{\mathsf{i},\varphi} H_{\mathsf{s},\theta}^* - E_{\mathsf{s},\varphi} H_{\mathsf{i},\theta}^*) \,. \tag{4.1.12}
\end{aligned}$$

Berg, Sorensen, and Chakrabarti (2008a) denote the Pointing terms on the right of equation (4.1.12) in the following way: The term in the first line is named incident $S_{i,r}$, in the second scattered $S_{s,r}$ and in the third line cross $S_{\text{cross},r}$ component of the radial part.

The net energy flow is considered by integrating the radial component of the Pointing vector given in equation (4.1.11) over a sphere with radius r circumscribing the scattering object, thus leading to the total absorbed energy

$$W_{\text{a}} = - \iint_{r=\text{const}} S_{\text{t},r} r^2 \text{d}A \,. \tag{4.1.13}$$

If the sign of W_{a} is negative, this amount of energy gets absorbed and the object temperature rises. Otherwise, if the sign is positive, the closed surface contains an active element. Under normal conditions, this is invalid for rain drops.

The overall net energy flow of the *incident* field via a volume W_{i} is zero (integration of the first term of equation (4.1.12)), because the waves transverse the volume without modification. Integration of the second term of equation (4.1.12) yields the *scattering* energy flow

$$W_{\text{s}} = \frac{1}{2} \Re \iint_{r=\text{const}} (E_{\text{s},\theta} H^*_{\text{s},\varphi} - E_{\text{s},\varphi} H^*_{\text{s},\theta}) r^2 \text{d}A \,. \tag{4.1.14}$$

Combining scattering and absorption yields the energy removed from the waves propagating in forward direction. This energy, called extinction, corresponds to the integration over $S_{\text{cross},r}$

$$\begin{aligned} W_{\text{ext}} &= W_{\text{a}} + W_{\text{s}} + W_{\text{i}} \\ &= -\frac{1}{2} \Re \iint_{r=\text{const}} (E_{\text{i},\theta} H^*_{\text{s},\varphi} + E_{\text{s},\theta} H^*_{\text{i},\varphi} - E_{\text{i},\varphi} H^*_{\text{s},\theta} - E_{\text{s},\varphi} H^*_{\text{i},\theta}) r^2 \text{d}A \,. \end{aligned} \tag{4.1.15}$$

Cross Sections

Measures relating the various energies discussed in the last paragraph to the incident energy are called cross sections. Literature (Ishimaru 1997; Berg, Sorensen, and Chakrabarti 2008a; Oguchi 1983; van de Hulst 1981; van Bladel 2007) defines the incident waves used for their calculations to be plane and of unit power per unit area. The *differential* cross section σ_{d} (in m^2/rad) that applies to the energy scattered by an object in the specified direction $\widehat{k}_k$ is defined to be

$$\sigma_{\text{d}}(\widehat{k}_0, \widehat{k}_k) = \lim_{r \to \infty} \frac{r^2 S_{\text{s}}}{S_{\text{i}}} \,.$$

The incident and scattered Pointing vectors are given in equations (4.1.9) and (4.1.10). Choosing the radius r to be $|\vec{r} - \vec{r}_k|$ yields

$$\sigma_{\mathrm{d}}(\widehat{k}_0, \widehat{k}_k) = |\vec{f}_k(\widehat{k}_0, \widehat{k}_k)|^2 \,. \tag{4.1.16}$$

In contrast to the differential cross section in $^{\mathrm{m}^2}/\mathrm{rad}$, the cross sections discussed in the following are normalised over all angles. A simple multiplication with 4π to account for azimuthal and polar angles transforms the differential cross section into the *bistatic* cross section σ_{bi}. Using an arbitrary scattering direction $\widehat{k}_k$ results in

$$\sigma_{\mathrm{bi}} = 4\pi\sigma_{\mathrm{d}} = 4\pi|\vec{f}_k(\widehat{k}_0, \widehat{k}_k)|^2 \,, \tag{4.1.17}$$

named *backscattering, monostatic or radar* cross section σ_{b} for the backward direction

$$\sigma_{\mathrm{b}} = 4\pi|\vec{f}_k(\widehat{k}_0, -\widehat{k}_0)|^2 \,. \tag{4.1.18}$$

While the bistatic cross section in principle denotes the energy ratio with respect to the scattering by an isotropic scatterer, the *scattering* cross section σ_{s} relates to the energy of an object with a specific scattering pattern

$$\sigma_{\mathrm{s}} = \iint\limits_{r=\mathrm{const}} \sigma_{\mathrm{d}} \mathrm{d}A = \iint\limits_{r=\mathrm{const}} |\vec{f}_k(\widehat{k}_0, \widehat{k}_k)|^2 \mathrm{d}A \,. \tag{4.1.19}$$

Accordingly, the total energy removed from the incident wave is considered with the *extinction* or *total* cross section σ_{ext}

$$\sigma_{\mathrm{ext}} = (4\pi/k)\Im[\widehat{k}_0 \cdot \vec{f}_k(\widehat{k}_0, \widehat{k}_0)] \,. \tag{4.1.20}$$

A derivation of this term is given by Born, Wolf, and Bhatia (1999) and relates the extincted energy W_{ext} from equation (4.1.15) to the incident energy.

The extinction of the energy at an object is caused by absorption and scattering, therefore the *absorption* cross section σ_{abs}, denoting the energy absorbed by a scatterer, results from $\sigma_{\mathrm{ext}} - \sigma_{\mathrm{s}}$. Furthermore, to complete the quantities related to energy cross sections: The so called albedo relates the amount of scattering to the total removed energy by $\sigma_{\mathrm{s}}/\sigma_{\mathrm{ext}}$.

4.1.2 Polarisation of the Scattered Field

Depending on the utilised coordinate system, the vector components of the field $\vec{E}_0$ may be separated (compare with equation (4.1.1)) into amplitude and direction of unit vectors. In Cartesian components this yields

$$\vec{E}_0 = E_{0x}\vec{e}_x + E_{0y}\vec{e}_y + E_{0z}\vec{e}_z \,. \tag{4.1.21}$$

Assuming the propagation to be in z-direction one obtains components in $\vec{e}_x$ and $\vec{e}_y$ direction, which are called horizontal and vertical polarisation. E_{0x} and E_{0y} denote the amount of polarisation in both directions.[2] Thus, applying this propagation vector, the coefficients of the general wave vector

$$\vec{k}_0 = k_x \vec{e}_x + k_y \vec{e}_y + k_z \vec{e}_z \tag{4.1.22}$$

yield zero except for k_z.

Expressing horizontal and vertical polarisation of incident and scattering waves as a two-port network, the scattering matrix relates the complex incident field amplitudes to the complex scattered field. The entire field is obtained by (compare to equation (4.1.4))

$$\begin{pmatrix} E_{s,v} \\ E_{s,h} \end{pmatrix} = \begin{pmatrix} S_{vv} & S_{hv} \\ S_{vh} & S_{hh} \end{pmatrix} \begin{pmatrix} E_{i,v} \\ E_{i,h} \end{pmatrix} \frac{e^{-j\vec{k}\cdot(\vec{r}-\vec{r}_k)}}{jkr} \ . \tag{4.1.23}$$

Literature further denotes the matrix elements S_{vv} and S_{hh} as S_1 and S_2, respectively, while S_{hv} and S_{vh} are named S_3 and S_4. Furthermore, the scattering function $\vec{f}(\widehat{k}_0, \widehat{k}_k)$ as used by e.g. Ishimaru (1997) is considered together with the S-matrix leading to

$$\begin{pmatrix} f_{11} & f_{12} \\ f_{12} & f_{22} \end{pmatrix} = -\frac{j}{k} \begin{pmatrix} S_1 & S_4 \\ S_3 & S_2 \end{pmatrix} \ . \tag{4.1.24}$$

Assuming a spherical coordinate system, horizontal and vertical polarisation corresponds to E_φ and E_θ. There, the coefficients of the amplitude scattering matrix S_1 to S_4 depend on the angles φ and θ. Additionally, the highly symmetrical nature of a spherical configuration induces S_3 and S_4 to be zero.

This allows transformation of the cross sections (given in equations (4.1.16) to (4.1.20)) into a formulation by applying the S-matrix $S(\theta, \varphi)$. However, the definition of the angle φ is problematic for forward or backward scattering ($\theta = 0°$ or $180°$). Therefore, these S-matrix elements and consequently equation (4.1.27) and equation (4.1.29) lack any φ dependence along these directions.

Differential Cross Section

$$(4.1.16): \qquad \sigma_d(\vec{k}_0, \vec{k}_k) = \frac{|S(\theta, \varphi)|^2}{k^2} \tag{4.1.25}$$

Bistatic Cross Section

$$(4.1.17): \qquad \sigma_{bi}(\vec{k}_0, \vec{k}_k) = \frac{4\pi}{k^2} |S(\theta, \varphi)|^2 \tag{4.1.26}$$

---

[2]Especially in publications dealing with scattering in the optical regime, the Stokes formulation, briefly described in section 4.2.4 substitutes a field description. The Stokes parameter denote intensity and other measurable variables and they are also capable of determining different polarisation states. Transformation rules can be found in literature (e.g. Ishimaru (1997); van de Hulst (1981)).

Backscattering Cross Section

$$(4.1.18): \qquad \sigma_\mathrm{b} = \frac{4\pi}{k^2}|S(\pi)|^2 \qquad\qquad (4.1.27)$$

Scattering Cross Section

$$(4.1.19): \qquad \sigma_\mathrm{s} = \frac{1}{k^2}\iint\limits_{r=\mathrm{const}} |S(\theta,\varphi)|^2 \mathrm{d}A \qquad\qquad (4.1.28)$$

Extinction/Total Cross Section

$$(4.1.20): \qquad \sigma_\mathrm{ext} = \frac{4\pi}{k^2}\Re S(0) \qquad\qquad (4.1.29)$$

4.1.3 Scattering by Spheres

In general, the derivation of the scattering amplitude $\vec{f}_k(\widehat{r}_0,\widehat{r}_k)$ used in equation (4.1.4) is rather complicated. The Helmholtz equation (compare with section 2.4)

$$\Delta\Psi + k^2\Psi = 0 \qquad\qquad (4.1.30)$$

expresses the differential equation for the solution Ψ in general. The equation can be solved applying problem adjusted boundary conditions. However, the solution is only feasible in certain coordinate systems. Textbooks (Oguchi 1983; Kerker 1969; Kahnert 2003) solve the Helmholtz equation in spherical coordinates. The solution was first proposed by and is named after Mie (1908). Appendix A.1 resumes the solution of the Helmholtz equation for coordinate systems with separable solutions. Appendix A.2 outlines the recipe for the derivation in spherical coordinates.

In short, the Helmholtz equation is solved by separation using

$$\Psi(r,\theta,\varphi) = \Theta(\theta)\Phi(\varphi)z(r)\,, \qquad\qquad (4.1.31)$$

where sine and cosine of multiple-angle m determine a solution of equation (4.1.30) for the φ dependence and Legendre functions of degree m and order n for the θ dependence:

$$\begin{aligned} \Theta &= P_n^m(\cos\theta), \\ \Phi_e &= \cos(m\varphi), \qquad \Phi_o = \sin(m\varphi)\,. \end{aligned} \qquad\qquad (4.1.32)$$

using the spherical coordinates φ and θ as illustrated in figure 4.3. Spherical Bessel and Hankel functions construct the solution $z(r)$ for the radius r with the argument denoting the size parameter x, relating the size of the scattering object to the wavelength by

$x = kr$

$$
\begin{aligned}
j_n(x) &= \sqrt{\frac{\pi}{2x}}\, J_{n+\frac{1}{2}}(x)\,, \\
y_n(x) &= \sqrt{\frac{\pi}{2x}}\, Y_{n+\frac{1}{2}}(x)\,, \\
h_n^{(1)}(x) &= j_n(x) + j\, y_n(x)\,, \\
h_n^{(2)}(x) &= j_n(x) - j\, y_n(x)\,.
\end{aligned}
\tag{4.1.33}
$$

Following the computations in the appendix for an incident electromagnetic wave propagating along z direction, the degree m yields zero and the scattering matrix of a
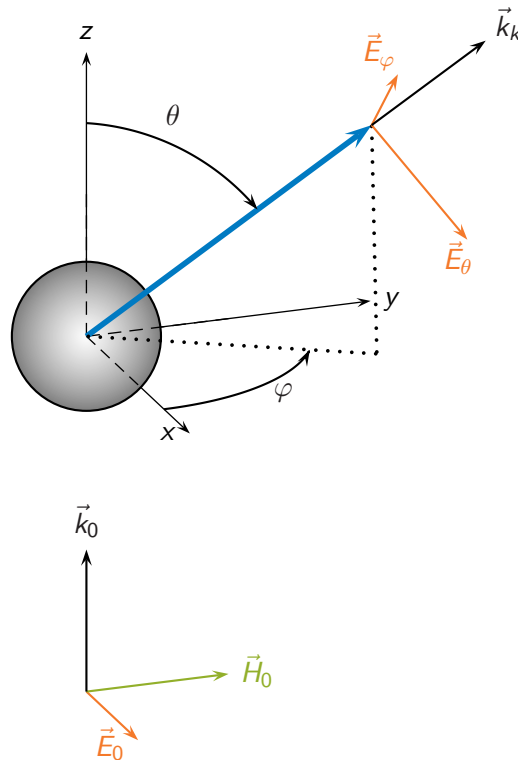

Figure 4.3: Incidence of a wave propagating in z direction and polarised in x direction on a spherical scatterer. Drawn are wave vector $\vec{k}_0$, electric field vector $\vec{E}_0$ and magnetic field vector $\vec{H}_0$. The blue vector indicates the vector from the scattering object towards the observation point. This vector spans the scattering plane with the angles θ and φ. The wave vector $\vec{k}_k$ the horizontal $\vec{E}_h$ and the vertical electric field component $\vec{E}_v$ express the scattered field. Co- and crosspolarization recorded at the receiver depend on the scattering angle φ. (5.2.1) and (5.2.2) transforms between Cartesian and spherical coordinates.

sphere is diagonal. Therefore the scattering matrix entries for horizontal and vertical polarisation result in

$$S_1(\theta, x) = \sum_n \frac{2n+1}{n(n+1)}[a_n(x)\pi_n(\cos\theta) + b_n(x)\tau_n(\cos\theta)]$$

$$S_2(\theta, x) = \sum_n \frac{2n+1}{n(n+1)}[a_n(x)\tau_n(\cos\theta) + b_n(x)\pi_n(\cos\theta)]$$

(4.1.34)

with

$$a_n(x) = \frac{m^2\, j_n(mx)[x\, j_n(x)]' - j_n(x)[mx\, j_n(mx)]'}{m^2\, j_n(mx)[x\, h_n^{(2)}(x)]' - h_n^{(2)}(x)[mx\, j_n(mx)]'}$$

$$b_n(x) = \frac{j_n(mx)[x\, j_n(x)]' - j_n(x)[mx\, j_n(mx)]'}{j_n(mx)[x\, h_n^{(2)}(x)]' - h_n^{(2)}(x)[mx\, j_n(mx)]'}$$

(4.1.35)

also depending on the refractive index m and

$$\pi_n(\cos\theta) = \frac{P_n(\cos\theta)}{\sin\theta}$$

$$\tau_n(\cos\theta) = \frac{d\, P_n(\cos\theta)}{d\theta}\ .$$

(4.1.36)

Equation (4.1.34) assumes linearly polarised waves incident on a sphere and scattered in arbitrary directions. The scattering process takes place in the scattering plane spanned by the incident and the scattered propagation vector. Scattering according to equation (4.1.23) applies to horizontal and vertical polarisation, thus equation (4.1.34) lacks any φ dependency. In spherical coordinates horizontal and vertical polarization correspond to E_φ and E_θ. If the scattering plane is rotated by an angle φ relative to the incident field, E_φ and E_θ are adjusted using a rotation matrix. This fulfils the φ dependence. Section 5.2 particularly describes the process in detail.

Following the calculations of the last section using a combination of equation (4.1.29) and equation (4.1.34) derives the cross sections

$$\sigma_s = \frac{2\pi}{k^2} \sum_n (2n+1)(|a_n|^2 + |b_n|^2)$$

(4.1.37)

$$\sigma_{\text{ext}} = \frac{2\pi}{k^2} \sum_n (2n+1)\Re(a_n + b_n)\ .$$

(4.1.38)

Waves propagating along an axis of a specified coordinate system are described by two polarisation amplitudes of the perpendicular unit vectors. For spherical systems in particular, the polarisation vectors point in $\vec{e}_\theta$ and $\vec{e}_\varphi$ direction. Utilising the system to solve the Helmholtz equation for the spherical approximation of the drop shape is preferable. Thus, applying the solution in these coordinates, it is possible to derive the entries of the scattering matrix and cross sections.

4.1.4 Coherent and Incoherent Signal

Before examining the special case of scattering by rain fields, a further issue requires consideration. Waves propagating through a dynamic statistical medium observe fluctuations resulting in a noisy received field. Ishimaru (1997) described the total field recorded at the receiver by a separation in coherent and incoherent part

$$
\begin{aligned}
\vec{E}_t(\vec{r}, t) &= \vec{E}_c(\vec{r}) + \vec{E}_f(\vec{r}, t) \\
&= \overline{\vec{E}_t(\vec{r}, t)} + \vec{E}_f(\vec{r}, t) \,,
\end{aligned}
\tag{4.1.39}
$$

where the coherent part denotes the mean of the total field.[3] The coherent part emerges from regarding the medium as a statistical ensemble, while accumulated field contributions of the individual objects generate the incoherent field.

Figure 4.4 illustrates coherent and incoherent signals. The black arrow represents the coherent attenuated incident waves at the receiver. On the left the red arrows show the contribution of scattering by some individual objects. The red statistical cloud in the right image illustrates contributions of phase and amplitude from a larger number of particles. Averaging in time provides the coherent part, while the signal variation originating from the moving drops causes the incoherent part.
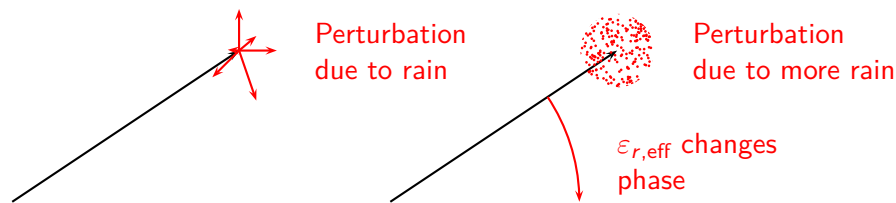

Figure 4.4: Illustration of the coherent (long black arrow) and incoherent (smaller vectors or points) field contributions. The left image exemplarily shows the influence from only few scattering objects, while the right one gives a statistical cloud.

---

[3]A similar concept is the rotation wave approximation used in quantum optics. This approximation averages the fast oscillating frequency components returning the envelope value (such as for the coherent signal part) and emphasises the slowly varying signal (comparable to the fluctuating incoherent part).

4.2 Scattering by Statistical Rain Fields

The previous section outlined the general foundation of the scattering principle. In particular the idea of coherent and incoherent signals is applied in the following. While this section focuses on the coherent part, section 4.3 derives the incoherent contribution.

Dealing with the rain field described as a statistical ensemble is a common concept. This section derives attenuation by applying the extinction cross section. The distribution of radii is a main property to describe the statistical ensemble. Subsection 3.2.3 already discussed the DSD supplying a derivation of rain related parameters applying equation (3.2.6).

Therefore, this section derives not only attenuation by the rain medium, but illustrates the approximation of a power law often applied in literature, as described in the introduction. Furthermore, it mentions the effective refractive index of the rain medium leading to a mean phase shift.

The section concludes the presented aspects with two significant complements. First, the interaction of adjacent drops potentially disturbs the global electromagnetic field. This concern is covered in section 4.2.3 by outlining multiple scattering approaches.

The radiative transfer method represents an alternative method to determine coherent and incoherent signals. In contrast to the approach presented in this work, this method is phenomenologically based. Conventionally, radiometry groups utilise this method for modelling the propagation of waves through atmospheric layers varying along a vertical path.

4.2.1 Calculation of Attenuation

To develop the coherent field, it is common to monitor the reduction of signal intensity of waves propagating through a medium, specifically a rain field (compare Oguchi (1983); Kerker (1969)). The attenuation in propagation direction z is

$$\frac{\mathrm{d}I}{\mathrm{d}z} = -\alpha I \tag{4.2.1}$$

which may be solved by the Lambert-Beer law (Ishimaru 1997)

$$I/I_0 = e^{-\alpha z} \quad \text{or} \quad I = I_0 e^{-\alpha z}. \tag{4.2.2}$$

I_0 defines the intensity at $z = 0$. The variable α denotes the ratio of energy decay inside the medium, corresponding to the extinction cross section σ_{ext} (compare with section 4.1.1, especially equation (4.1.20) accordingly). The total extinction results from accumulating the extinction of all drops and normalising the result by the volume V:

$$\alpha = \frac{\sum \sigma_{\text{ext}}}{V}. \tag{4.2.3}$$

Transforming the discrete accumulation of drops per volume to its statistical equivalent, using the DSD given in section 3.2.3 yields

$$\frac{\sum \sigma_{\text{ext}}}{V} = \int_0^{r_{\text{max}}} \sigma_{\text{ext}}(r) n(r) \mathrm{d}r \tag{4.2.4}$$

thus obtaining the attenuation

$$\alpha = \int_0^{r_{\text{max}}} \sigma_{\text{ext}}(r) n(r) \mathrm{d}r \quad (\text{Np}/\text{m}). \tag{4.2.5}$$

A conversion to dB/km following Aydin and Daisley (2000) yields

$$A = 4.343 \cdot 10^3 \int_0^{r_{\text{max}}} \sigma_{\text{ext}}(r) n(r) \mathrm{d}r \quad (\text{dB}/\text{km}). \tag{4.2.6}$$

Utilising this result, one inserts the attenuation of the signal incident on a drop, when passing a surrounding medium, into equation (4.1.6). Referring to figure 4.2, the attenuation on the path from transmitter to drop is

$$\gamma_1 = \int_0^{r_k} \alpha(s) \mathrm{d}s \tag{4.2.7}$$

and from drop to receiver

$$\gamma_2 = \int_{r_k}^{|\vec{r} - \vec{r_k}|} \alpha(s) \mathrm{d}s, \tag{4.2.8}$$

thus resulting in the modified equation

$$\vec{E}_s(\vec{r_k}) = \vec{f}_k(\widehat{k}_0, \widehat{k}_k) \frac{e^{-j(\vec{k_0} \cdot \vec{r_k} + k_0 |\vec{r} - \vec{r_k}|) - \frac{\gamma_1}{2} - \frac{\gamma_2}{2}}}{r_k |\vec{r} - \vec{r_k}|} E_0. \tag{4.2.9}$$

To apply the attenuation, which is related to the intensity, to a field contribution, γ_1 and γ_2 are divided by two. Consequently, this equation involves the coherent field. Assuming the path between transmitter and receiver to be sufficiently long, the overall contributions from the distances r_k and $|\vec{r} - \vec{r_k}|$ may be approximated by $|\vec{r}|$ (compare with figure 4.2 in section 4.1.1 for nomenclature), thus the field completes to

$$\vec{E}_s(\vec{r_k}) = \vec{f}_k(\widehat{k}_0, \widehat{k}_k) \frac{e^{-j(\vec{k_0} \cdot \vec{r_k} + k_0 |\vec{r} - \vec{r_k}|) - \frac{\gamma}{2}}}{r_k |\vec{r} - \vec{r_k}|} E_0 \tag{4.2.10}$$

41

with

$$\gamma = \int\limits_0^r \alpha(s)\mathrm{d}s\,. \tag{4.2.11}$$

Assuming the rain drops to be spherical, equation (4.1.38) gives the extinction cross section as

$$\sigma_{\text{ext}} = \frac{4\pi}{k^2} \sum_n (2n+1)\Re(a_n + b_n)\,, \tag{4.2.12}$$

where the Mie coefficients a_n and b_n depend on the radius. Including both size dependent measures, extinction cross section and DSD, in equation (4.2.5) allows calculation of the attenuation. The scattering by individual drops transfers energy lost by the decrease of the incident field amplitude to the scattered field. Thus, according to Zurk, Tsang, and Winebrenner (1996), the energy reducing the coherent field is partly shifted to the incoherent field.

Figure 4.5 draws the individual and multiplied terms from equation (4.2.5) with spherical scatterers at 22 GHz for rain rates of 0.1 mm/h and 100 mm/h. The solid lines show the radius dependent scattering coefficient in the forward direction $S(0, r)$, which is proportional to σ_{ext}. The dashed line gives the Marshall-Palmer DSD from equation (3.2.2) with the parameters listed in table 3.2. The dotted line illustrates the argument of the integral of equation (4.2.5). An integration over this curve yields the attenuation. Examining the plots shows maximum power contribution at different radii. For 0.1 mm/h and 100 mm/h the plots show extrema at size parameter of 0.2 and around 0.75, respectively.

Figure 4.6 shows the attenuation derived according to equation (4.2.6) for various rain rates dependent on frequency.

4.2.2 Effective Refractive Index

Maintaining the idea of a rain field as a random medium, it is possible to apply the bulk refractive index for a medium of sparsely distributed spherical scatterers as given by Olsen, Rogers, and Hodge (1978) in the form of

$$\eta = 1 - \mathrm{j}\frac{2\pi}{k^3} \int\limits_0^\infty S(0, r)n(r)\mathrm{d}r\,, \tag{4.2.13}$$

where $S(0, r)$ denotes the radius dependent scattering coefficient in the forward direction. Since the imaginary component of this equation denotes the attenuation, which is calculated as stated in equation (4.2.5) employing the extinction given in equation (4.1.29) depending on the radius, the real part gives the phase change (Oguchi 1973). The effective refractive index is not physical, but allows a more practical description of the medium properties, such as the effective phase shift. An extended theory

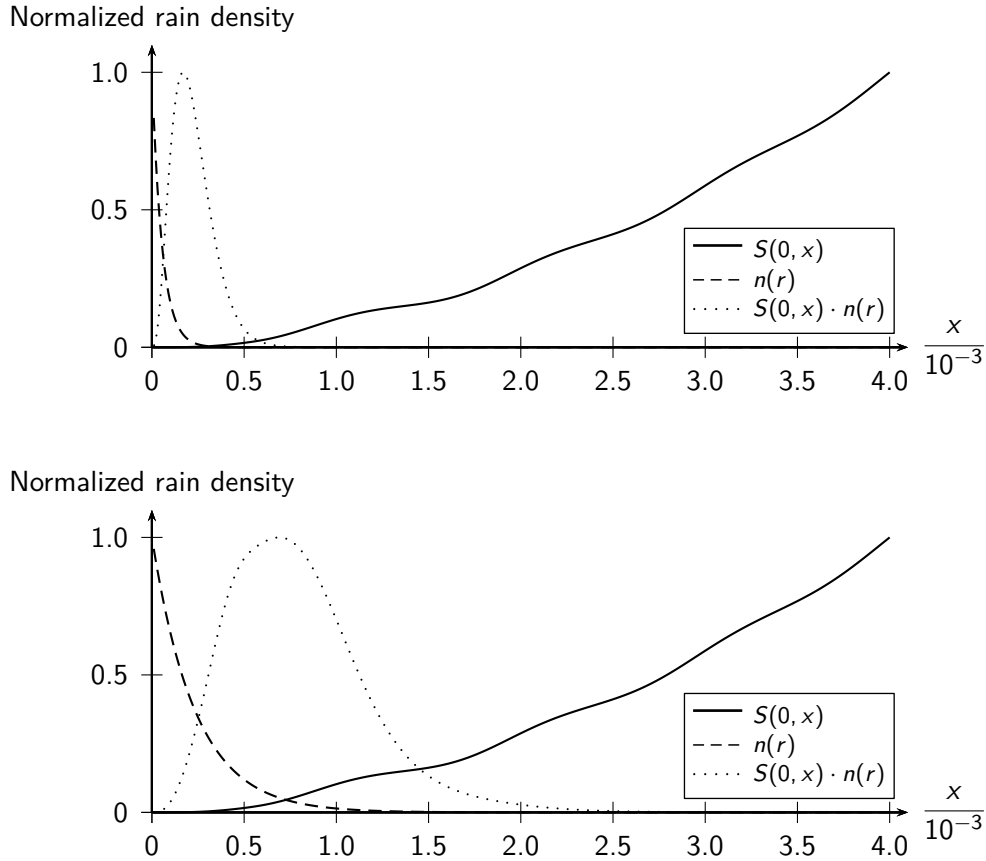Normalized rain density

Normalized rain density

Figure 4.5: Analysis of the intensity of the scattering coefficients in forward direction depending on the size parameter $x = kr$, the DSD and the product of both at 22 GHz. The curves are normalised on their maximum for visibility. While the graph on the top shows values for a rain rate of 0.1 mm/h, the lower gives curves for 100 mm/h.

using T-Matrix formulation and Monte Carlo simulations was given by Siqueira and Sarabandi (1996), while Sihvola and Kong (1988) treated the case of particles with diameter much less than the wavelength.

Analogous to a power law relating rain rate and attenuation, a power law relating a phase change to the rain rate may be derived (Matricciani 2009).
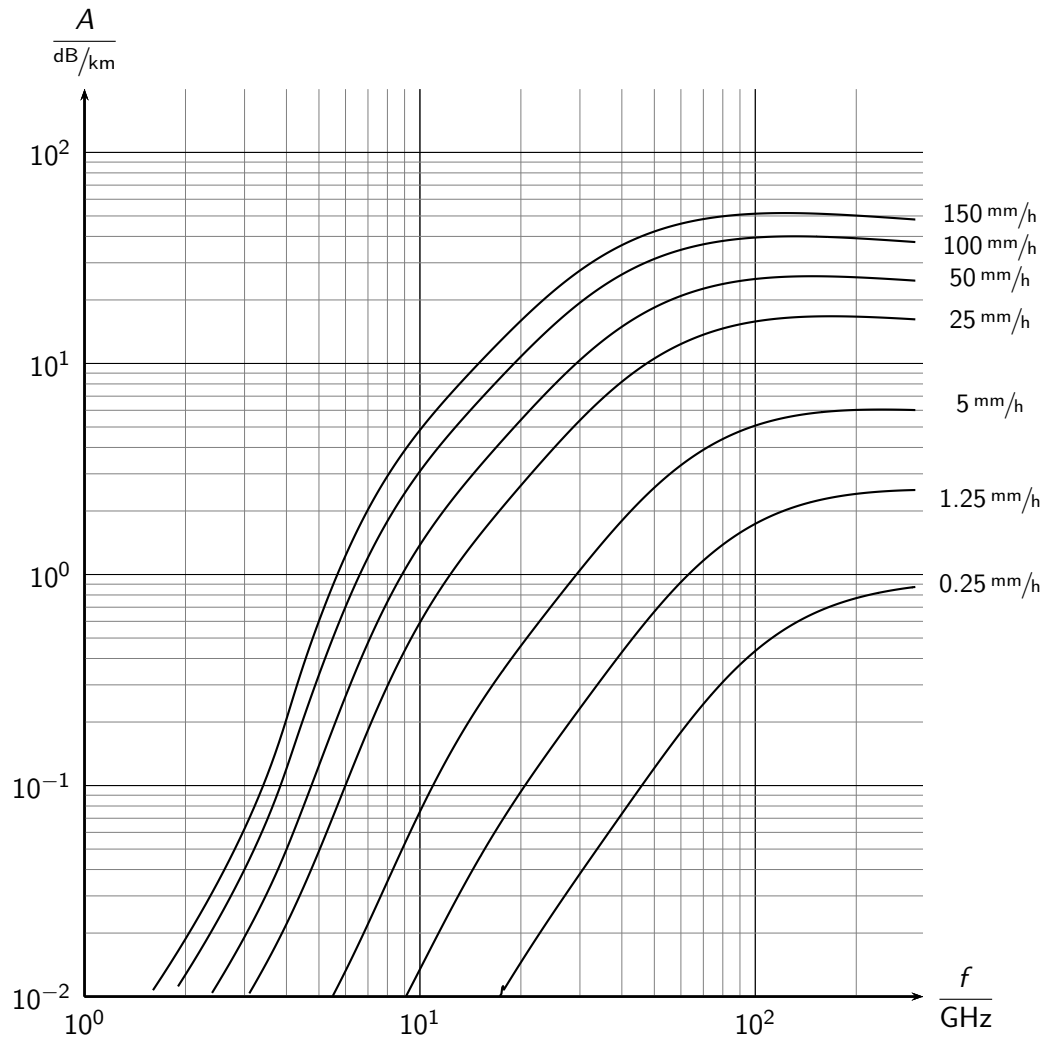
Figure 4.6: Attenuation versus frequency calculated according to equation (4.2.6) for different rain rates.

4.2.3 Multiple Scattering

This work considers scattering by individual drops of a rain field. To this end, it accounts for the influence of the incident waves on each drop. However, the scattering contributions by the drops may interact, leading to multiple scattering. Thus, this subsection gives an overview of literature discussing this topic.

Delimiting investigations to single scattering is valid at low frequencies. Section 4.3 presents the single scattering approach in detail. Higher frequencies require consideration of multiple scattering. Literature suggests the calculation of attenuation, presented in the last section, as the first order approximation of multiple scattering.

Single scattering denotes the synthesis of scattering contributions by individual drops, thus resulting in the incoherent noisy signal. According to Ishimaru (1997), this approach is valid in tenuous media. Battan (1973) verified this condition for weather radar. Other publications (Ishimaru and Cheung 1980; Tsolakis and Stutzman 1982; Setijadi et al. 2009) restricted single scattering to frequencies below 30 GHz. Following Ishimaru and Cheung (1980) the absorbed power, determined using the absorption cross section σ_{abs}, exceeds the scattering power, denoted by the scattering cross section σ_{scat} in this frequency range. Thus, the power present for drop interaction is small.

A second criterion for single scattering is the distance between two drops. According to Ryde and Ryde (1944) and Medhurst (1965) minor interaction is feasible for drops with a distance larger than ten times of their radius. Ishimaru (1997) converted this condition to be applicable to a rain field. He calculated an average density ρ constant along the link length L. Accordingly, equation (4.2.5) approaches $\rho\sigma_{\mathrm{ext}}L$. Single scattering is accurate if the resulting value is smaller than one.

For high rain rates the density of the rain medium increases, although the medium itself remains tenuous. Thus, neighbouring rain drops likely influence each other. As a consequence Ishimaru (1997) and Oguchi (1983) proposed to use a first order scattering approximation, valid in the considered frequency range (Rogers and Olsen 1983). This approach extincts the waves while passing the rain field. Thus, a scattering rain drop exhibits a signal attenuated by the already passed amount of rain. Accordingly, this work implements the proposed method described by equation (4.2.10).

In addition to the presented methods one could account for interaction between adjacent drops. This influence may be included by utilising translation operators of multipole extensions (Berg, Sorensen, and Chakrabarti 2008b; Kahnert 2003; Mishchenko et al. 2007; Bruning and Yuen Lo 1971a; Bruning and Yuen Lo 1971b; Zurk, Tsang, and Winebrenner 1996).

4.2.4 Radiative Transfer

Due to the importance of radiative transfer (RT) in related fields, this chapter ends with a very brief view on this technique, which is also known as transport theory. The theory is based on the conservation of energy (equation of transfer) (Ishimaru 1997;

Chandrasekhar 1960) according to

$$\hat{n}\nabla\vec{I} + \gamma\vec{I} = \iint\limits_{r=\text{const}} \overline{P} \cdot \vec{I}\mathrm{d}A \qquad (4.2.14)$$

applied to the intensity Stokes vector $\vec{I}$. This intensity vector consist of four parameters which are related to the horizontal and vertical electric field by

$$\vec{I} = \begin{bmatrix} I \\ Q \\ U \\ V \end{bmatrix} = \begin{bmatrix} |E_x|^2 + |E_y|^2 \\ |E_x|^2 - |E_y|^2 \\ 2\Re\{E_x E_y^*\} \\ 2\Re\{E_x E_y^*\} \end{bmatrix}. \qquad (4.2.15)$$

Extinction and scattering are given by γ and the phase matrix $\overline{P}$, respectively. The phase matrix relates incident and scattered quantities related to the Stokes parameters in a similar way as the scattering matrix. It is possible to derive the phase matrix from the scattering matrix, analogous to the derivation of the Stokes parameters, while the other way round is complicated. All parameters possibly depend on space and time. Researchers using radiometers exploit RT for its ability to model the propagation through heterogeneous atmospheric layers in particular. Analogous to the present work, the method accounts for coherent and incoherent intensities. However, while the RT yields results for the rain ensemble, this work deals with individual rain drops.

An interesting point is the construction of the phase matrix. Ishimaru and Cheung (1980) showed calculations for spherical drops, Deiveegan, Balaji, and Venkateshan (2008) added the Marshall-Palmer DSD. Czekala and Simmer (1998) used a Beard-Chuang model and a Marshall-Palmer DSD. Evans and Stephens (1991) considered arbitrarily shaped particles in general. A European project (Sreerekha et al. 2006) developed a computer program utilising T-Matrix and direct dipole approximation methods to derive the phase matrix for 200 to 1000 GHz.

To summarise, this section applied the basics explained in section 4.1 to derive the influence of a rain field as statistic tenuous medium on propagating waves. The medium influences amplitude and phase of the propagating waves yielding attenuation and its effective refractive index.

Objects inside a medium are likely to mutually influence each other. This section reported about analyses concerning the multiple scattering. In summary, considering the attenuation of the entire field, as included in the coherent signal, is sufficient.

4.3 Scattering at Drop Scale

So far this thesis has considered the influence of rain—interpreted as tenuous medium—on propagating waves. Additionally, each individual drop influences the resulting field. Section 4.1.4 denoted this part an incoherent signal.

To shed light on the origin of the incoherent signal, this section follows Mishchenko 2008. Figure 4.7 schematically illustrates a field incident on an object. The object scatters the incident waves according to its scattering pattern. Only a part of the scattered energy reaches the receiver. Section 4.2.3 considers further interference of these waves with the incident waves and other objects.

Approximating the rain drops as spheres allows the use of equations already derived in section 4.1.3. This section introduced the size parameter x, crucial for the calculation of the Bessel and Hankel functions. The parameter x denotes the ratio of the size of the scattering object to the wavelength.

This work deals with electromagnetic waves in the GHz regime. In order to get an impression, figure 4.8 plots the equation $x = kr$ for selected frequencies and rain drop radii from $0\,\text{mm}$ to $4\,\text{mm}$. Apparently the size parameter is in the range of one. While for large or small objects approximations such as Rayleigh scattering or ray optics are valid, the value around one requires the Mie solution as derived in section 4.1.3.

The solution returns scattering patterns depending on the scattering angle. Figure 4.9 presents scattering patterns for selected values of x. Scattering is shown by a sphere normalised to the value at $\varphi = 0°$ or $180°$. The upper part denotes the scattering matrix entry S_1, the lower part S_2, In the left plot the solid line is calculated with a size coefficient x of 0.1, the dashed line denotes x equal to 0.6, while the dotted line stands for a size coefficient of 1.5. On the right hand side the lines denote the following size coefficients: solid: $x = 1.8$; dashed: $x = 2$; dotted: $x = 3$.

Figure 4.10 and figure 4.11 illustrate the first five expansion terms of the Mie coefficients a and b as well as the θ dependent functions π and τ. While figure 4.10 displays
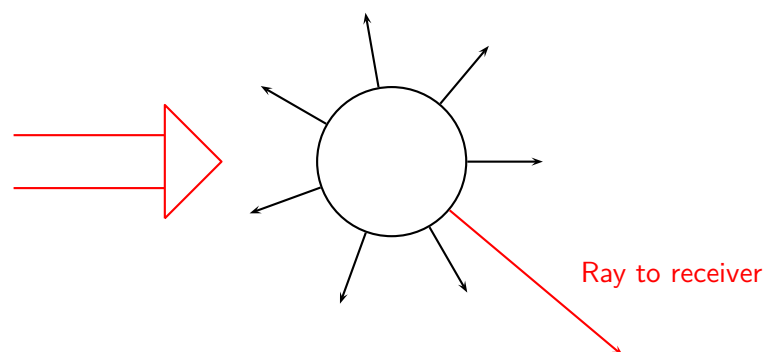

Figure 4.7: Illustration of the scattering principle. Shown are the incident ray and rays scattered in all directions. The image indicates the ray to the receiver in particular.
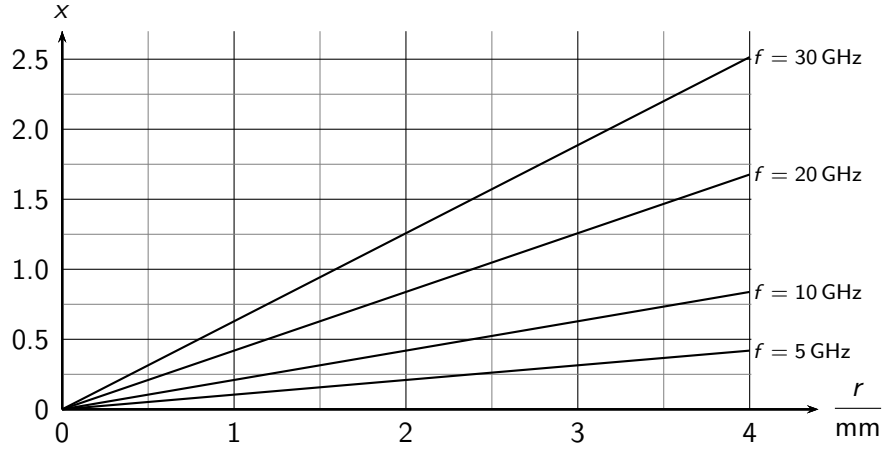
Figure 4.8: Graph giving the size parameter of a certain radius depending on the wavelength.

π_n and a_n, figure 4.11 shows b_n and τ_n.

Numerical computations fail to perform the infinite summation of the scattering coefficients in equation (4.1.34). Wiscombe 1980 suggested a limitation to $N = x + 4x^{1/3} + 1$ terms depending on the size parameter. This approximation is valid for x ranging from 0.02 to 8. Increased orders yield $|a_n|^2 + |b_n|^2$ smaller than 10^{-14} (compare with figure 4.10 and figure 4.11 for classifying this quantity) leading to negligible contributions.

Thus, every individual rain drop contributes a wave vector dependent on size and scattering angle to the total field (see figure 4.7). Therefore, the total incoherent field is an accumulation of the individual field contributions of the individual drops indexed with k:

$$\vec{E}_f(\vec{r}, t) = \frac{\sum\limits_{k=1}^{K} \vec{E}_k(\vec{r}, \vec{r}_k, t)}{K(t)} \, , \tag{4.3.1}$$

where the total number of drops K may vary with time.

Additionally, inserting the derived angle dependent scattering parameters shown in figure 4.9 into equations (4.1.28) and (4.1.29) as well as considering their difference returns extinction, scattering and absorption cross section. Figure 4.12 shows their magnitudes depending on the size parameter. Furthermore, the figure helps to quickly evaluate values for different radii depending on frequency.
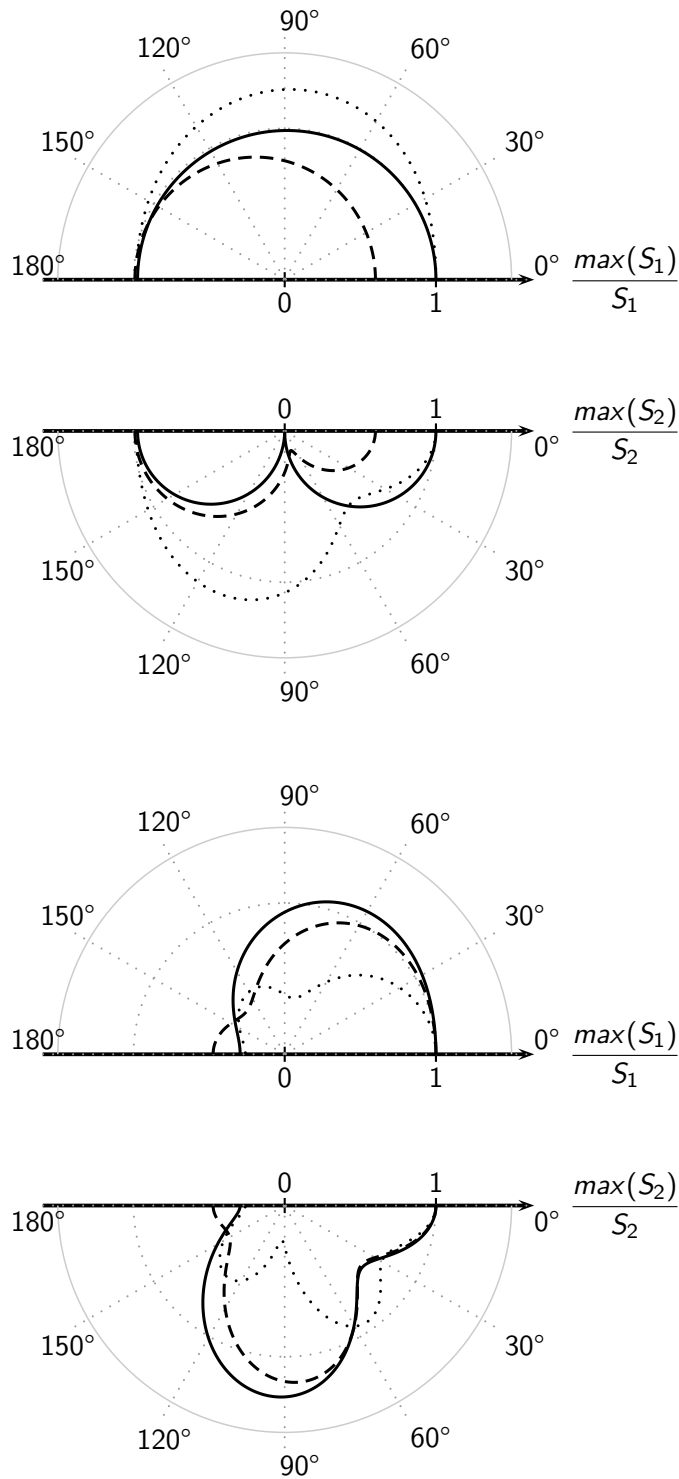
Figure 4.9: Scattering pattern of spheres with different line styles indicating different size parameters x. Left: solid: 0.1, dashed: 0.6, dotted: 1.5; right: solid: 1.8; dashed: 2; dotted: 3. S_1 relates the vertical field components (in θ direction), S_2 relates the horizontal ones (in φ direction).
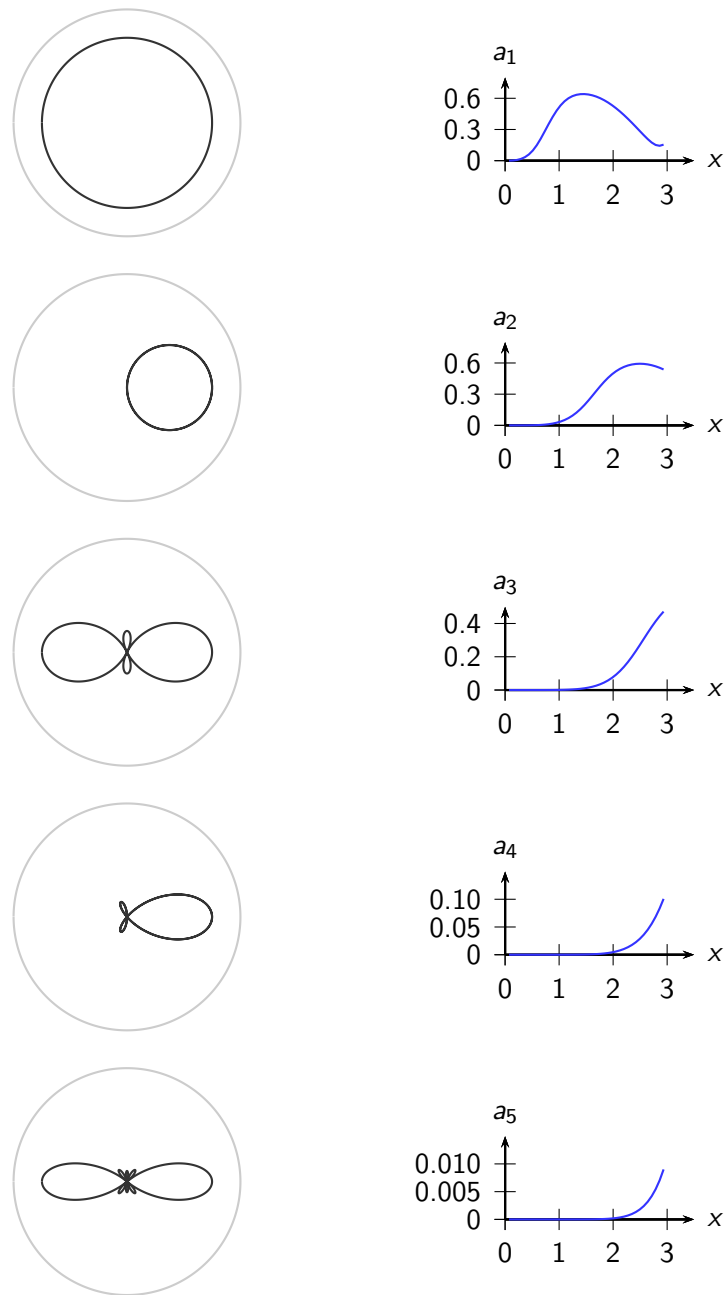
Figure 4.10: Illustration of contributions to the scattering matrix of equation (4.1.34). The left figures show the first five π functions of equation (4.1.36). On the right hand side the absolute value of the a_n coefficients as given in equation (4.1.35) are plotted. The coefficients and/or the refractive index m of water are calculated for a frequency of 35 GHz at 25 °C (compare with section 3.1.2).
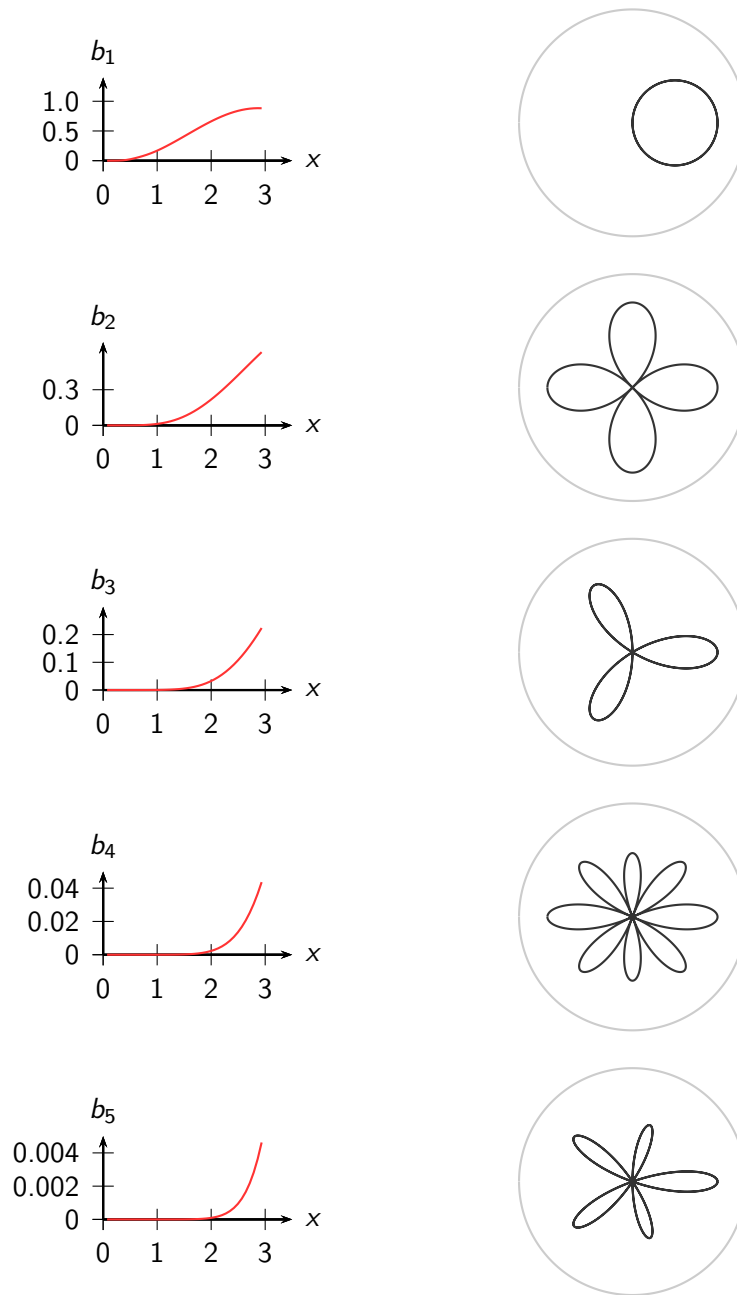
Figure 4.11: Illustration of contributions to the scattering matrix of equation (4.1.34). The right figures show the first five τ functions of equation (4.1.36). On the left hand side the absolute value of the b_n coefficients as given in equation (4.1.35) are plotted. The coefficients and/or the refractive index m of water are calculated for a frequency of 35 GHz at 25 °C (compare with section 3.1.2).
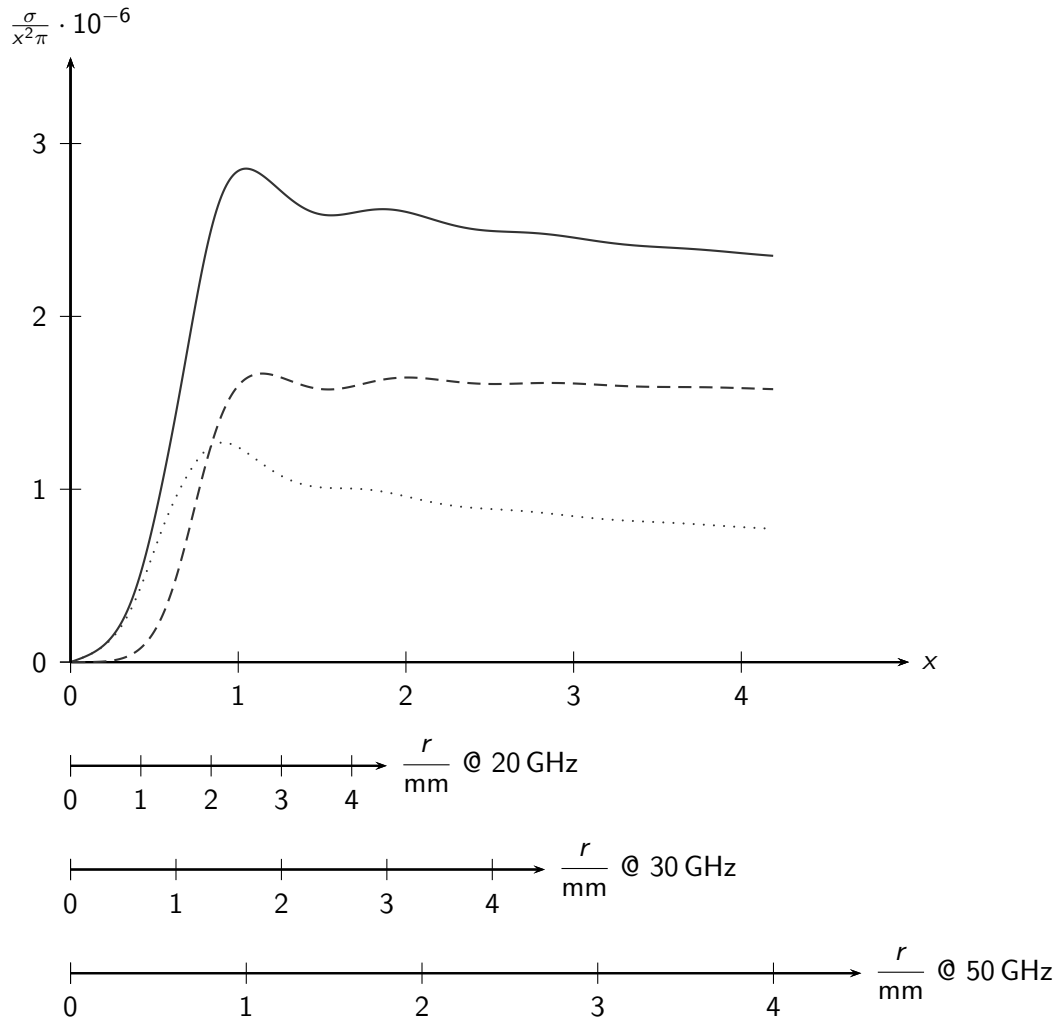
Figure 4.12: Illustration of extinction (solid line), scattering (dashed) and absorption (dotted) cross section normalised on the size parameter x and related to it. Additional x-axes give the relation relative to the radius for different frequencies.

4.4 Verification

Figure 4.13 shows a comparison study performed with values returned by the presented approach coded in MATLAB versus results returned by the two commercial software packages CST Microwave Studio and FEKO. The image illustrates field values for large ($r = 5 \cdot 10^{-3}$ m) rain drops at a frequency of 22 GHz. Drawn are absolute values of the two spherical polarisations $|E_\theta|$. Additionally $|E_\varphi|$ and the total field amplitude $|E_\theta^2 + E_\varphi^2|$ were calculated. All the scattering patterns calculated by the three methods show excellent agreement.

To summarise, this chapter introduced background knowledge for the modelling of the propagation of electromagnetic waves throughy rain. The implementation of the principles discussed in this and the previous chapter is addressed in the following ones.
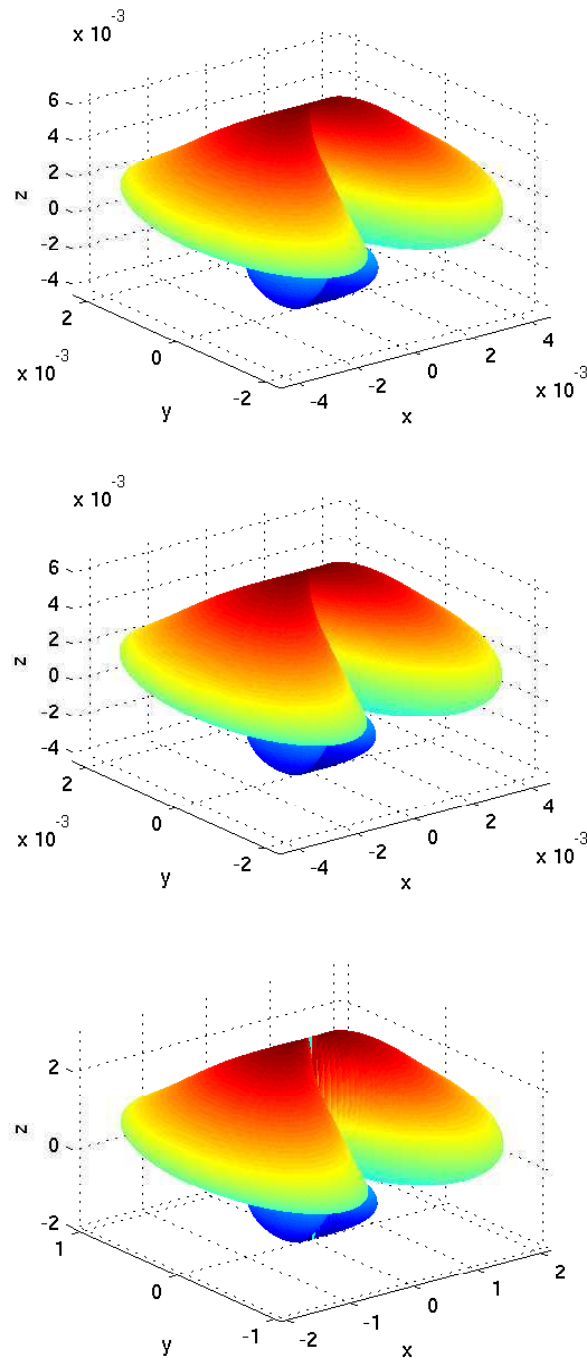
Figure 4.13: Plots of farfields calculated with the Mie based code (in the third row) and for verification purposes with CST (first row) and with FEKO (second row). Shown is $|E_\theta|$ for the considered drop size of $r = 5 \cdot 10^{-3}$ m calculated at a frequency of 22 GHz and a permittivity ε_r of 81 matching the static values of CST Microwave Studio (`www.cst.com`) and FEKO (`www.feko.info`).

5 Numerical Implementation Principles

Recently, different groups established synthetic rain fields. Among them are Luini and Capsoni (2009) with the MultiEXCELL approach, Matricciani (1996) using the synthetic storm technique and Schleiss, Berne, and Uijlenhoet (2009). The methods create realistic rain parameters over a wide spatial extent with a resolution in the kilometre range.

In contrast to these macroscopic rain fields, this work designs a synthetic rain field on a microscopic scale. The purpose of the presented approach is to model rain in great detail by composing the field of individual drops according to statistical rain parameters.

The framework of the proposed model allows adjustments to account for any property discussed in the last chapter. Thus, the model offers the possibility to closely mimic reality. This potential can be put into use by a comparison between real measurement data, obtained with the purpose-built link setup in the PROCEMA project, and simulations resulting from the outlined approach. To this end, the simulation setup, whose results are presented in the next chapter, follows the specification of this link. Consequently, the simulation volume extends 500 m in the propagation direction, while the frequency emitted by the transceiver is 22 GHz, according to the experiment.

Applying these dimensions, 6 to 12 million drops, depending on the rain rate, populate the simulation volume. However, processing this number of objects is, without optimisation and depending on the amount of operations per object, time consuming. In particular, the execution of Mie scattering takes computational effort, depending on the required expansion order of Bessel functions. Section 4.1.3 supplies a rule of thumb to determine this order while ensuring acceptable accuracy. Applying a drop radius limit of 4 mm, the maximum size parameter at 22 GHz is 1.84 yielding an expansion order of 5.

This chapter presents the composition of coherent and incoherent signals of simulated waves propagating through the synthetic rain field. After outlining the simulation cycle, the chapter first sheds light on the predominant scattering step. Subsequently, the third section describes the initial parameters and explains the particular steps, referring to the preceding chapters for further information on the theoretical background.

5.1 Random Rain Field Generation

The background knowledge of the preceding chapters allows simulation of electromagnetic propagation through a synthetic rain field. The calculations necessary to perform

this task were implemented in MATLAB. Figure 5.1 illustrates the individual simulation steps.
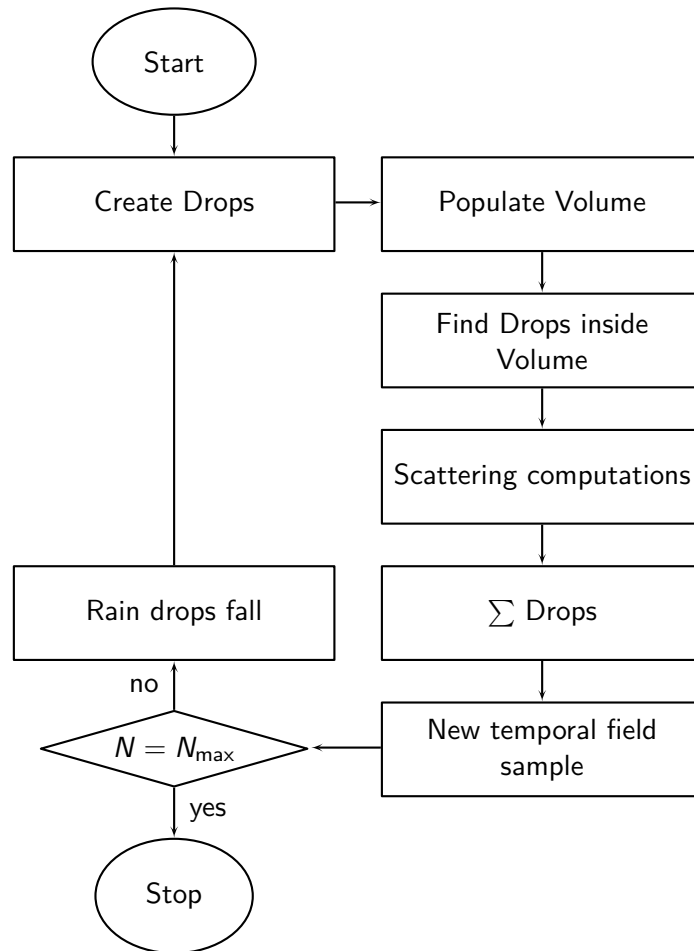

Figure 5.1: Flowchart of the simulation process.

Prior to the simulation cycle initial parameters regarding the electromagnetic and rain properties are quantified and stored in a struct variable to allow their easy manual adjustment or modification by the program modules.

The simulation starts by creating drops with radii according to the chosen DSD. Subsequently, these drops populate a desired volume. In the first step, this equals the full simulation volume. The algorithm then goes on to generate drops inside a volume on top of the simulation volume to sustain continuous rain fall. Following, a selection process indexes drops located inside the specified simulation volume. Non indexed drops are defined either as yet to enter the volume or as no longer present in the volume. Next, the algorithm performs calculations of the scattering of the incident electromagnetic waves by the selected drops and determines the individual extinction contributions. Finally, accumulation of the scattering and extinction components yields

a new field sample. After moving the drops according to the considered motion types, the simulation run proceeds until stop criteria are met.

To begin with, the next section describes the scattering process due to its dominance and importance in the simulation algorithm. In the following, section 5.3 illustrates the remaining steps including a description of initialisation parameters.

5.2 Calculation of the Scattered Field

The central and most dominant process of the simulation cycle is the scattering of incident waves by rain drops. Section 4.1.3 and the appendix provide its theoretical fundamentals. The scattering stage includes coordinate transformation of the fields and scattering by the drop.

Prior to the scattering process, the incident field requires a transformation to the drop adjusted coordinate system. Therefore, a rotation matrix converts the Cartesian incident field components to spherical ones. After this process, another matrix performs the back-conversion of the scattered field into Cartesian coordinates. The scattering plane of the specific drop defines the reference for the spherical components. The vectors source - object and object - drain span this plane. Thus, the angles φ and θ relate the global coordinate system and the drop specific system defined by the scattering plane.

The following matrix rotates the incident field from Cartesian coordinates to spherical coordinates

$$\begin{pmatrix} E_{i,\parallel} \\ E_{i,\perp} \end{pmatrix} = \begin{pmatrix} E_{i,\theta} \\ E_{i,\varphi} \end{pmatrix} = \begin{bmatrix} \cos\varphi & \sin\varphi \\ -\sin\varphi & \cos\varphi \end{bmatrix} \begin{pmatrix} E_{i,x} \\ E_{i,y} \end{pmatrix}. \tag{5.2.1}$$

Accordingly, the scattered field is re-transformed by

$$\begin{pmatrix} E_{s,x} \\ E_{s,y} \\ E_{s,z} \end{pmatrix} = \begin{bmatrix} \cos\theta\cos\varphi & -\sin\varphi \\ \cos\theta\sin\varphi & \cos\varphi \\ -\sin\theta & 0 \end{bmatrix} \begin{pmatrix} E_{s,\theta} \\ E_{s,\varphi} \end{pmatrix}. \tag{5.2.2}$$

The scattering computations follow equation (4.1.34). This equation shows the dependence of the scattering matrix entries S_1 and S_2 on a combination of the Mie coefficients a and b as well as of π and τ functions, presented later in this work.

5.2.1 Mie Coefficients *a* and *b*

Equation (4.1.35) describes the calculations required to derive a and b. A recursion concerning the order n, as given by Abramowitz and Stegun (1964), serves to efficiently compute the corresponding derivatives of Bessel and Hankel functions according to

$$[xz_n(x)]' = xz_{n-1}(x) - nz_n(x). \tag{5.2.3}$$

Accordingly, further approaches accelerate the derivation of the Mie coefficients while increasing the required memory. The Mie coefficients related to an individual drop, which depend on its radius and refractive index, remain constant during the drops simulation time. When a drop enters the simulation volume, the algorithm computes its Mie coefficients and stores them in the drop matrix. Therefore, instead of recalculating the coefficients every time step, only coefficients for new drops need to be considered, while the already computed and stored values are reused. This procedure significantly reduces the simulation time.

A further decrease of simulation effort is achieved by applying look-up tables. A trial shows that while tables listing Bessel functions of any kind are difficult to calculate due to their singularities, tables for Mie coefficients are steady and accurate. Applying a resolution of the argument of 10^{-5} results in a relative error of maximum 10^{-7}.

5.2.2 π and τ Functions

Analogous to the Mie coefficients Bohren and Huffman (1983) give a recursion formula for the θ dependent functions from equation (4.1.36) in form of

$$
\begin{aligned}
\pi_n(u) &= \frac{2n-1}{n-1} u \pi_{n-1}(u) - \frac{n}{n-1} \pi_{n-2}(u) \\
\tau_n(u) &= n u \pi_n(u) - (n+1) \pi_{n-1}(u).
\end{aligned}
\tag{5.2.4}
$$

The initial parameters for the calculation of π_n and τ_n are

$$
\pi_0(u) = 0, \quad \tau_0(u) = 0 \quad \text{and} \quad \pi_1(u) = 1.
\tag{5.2.5}
$$

5.2.3 Calculation of Field Sample for Step n

Following the arguments of section 4.1.4 the total field consists of a coherent and an incoherent part. The total extinction of the rain field causes the coherent signal (equation (4.2.10)). This extinction results from the accumulation of the contributions by the individual drops given in equation (4.1.38). The computation of this equation applies the Mie coefficients a and b, already derived in the scattering step.

Accumulating all drop contributions and normalising over the simulation volume results in the total extinction

$$
\sigma_{\text{ext,Vol}} = \frac{\sum \sigma_{\text{ext}}}{V_{\text{simulation}}}
\tag{5.2.6}
$$

leading to the total coherent field (compare with equation (4.2.9))

$$
\vec{E}_c(\vec{r}) = \vec{E}_i(\vec{r}) \exp\left(-\frac{1}{2} \frac{\sum \sigma_{\text{ext}}}{V_{\text{simulation}}} \Delta x \right).
\tag{5.2.7}
$$

In addition, the scattering contributions from all individual drops K generate the inco-

parameter name	symbol	variable name	value	unit
speed of light	c	c	299 792 458	$\mathrm{m/s}$
frequency	f	ini.f	$22 \cdot 10^9$	Hz
direction of propagation (fixed!)	$\vec{k}$	ini.k_vec	[1 0 0].'	
polarisation	$\vec{E}_0$	ini.k_field	[0 1 0].'	
(normalised at simulation start)				
amplitude of electric field	E_0	ini.E_0	1	$\mathrm{V/m}$

Table 5.1: Radiation parameters defined in the numerical implementation.

herent field

$$\vec{E}_{\mathrm{f}}(\vec{r}, t) = \frac{\sum\limits_{k=1}^{K} \vec{E}_k(\vec{r}, \vec{r}_k, t)}{K(t)} \ .$$

(5.2.8)

Combining both terms returns the total field for the time step n.

5.3 Simulation Model

This section outlines the remaining step of the virtual rain progress outlined in figure 5.2. The algorithm starts with the definition of initial field, geometry, rain and simulation parameters. Next, basic relations derive quantities resulting from these parameters. These parameters, like frequency, drop size distribution and duration of the simulation may easily be adjusted to simulate differing conditions.

5.3.1 Parameters

This subsection lists all available simulation parameters and derivations of related quantities. In addition, figure 5.2 shows an image of radiation and geometry parameters. Table 5.1 lists the possible radiation parameters. Here .' denotes the complex transpose of the vector, a notation adapted from the formulation in MATLAB.

Table 5.2 gives the geometry parameters set in the simulation as illustrated in figure 5.2. A cuboid spreading from source to receiver serves as initial simulation volume. The maximum of the Fresnel radius, which depends on the frequency, determines its transverse size. Namely, a ray scattered by an object at the Fresnel radius destructively interferes with the direct ray. It is maximum at half the distance source - drain and outlines an ellipsoid around source and drain. If desired, the simulation volume may be adopted to this Fresnel ellipsoid by modifying the parameter *ini.mainVolume*. The location variable of the transceiver *ini.source* is set empty to apply incident plane waves. For a point source emitting the waves *ini.source* contains its location vector.

Time parameters listed in table 5.3 define the simulation resolution and a possible stop criterion. An alternative stop criterion is determined by the steps necessary to analyse
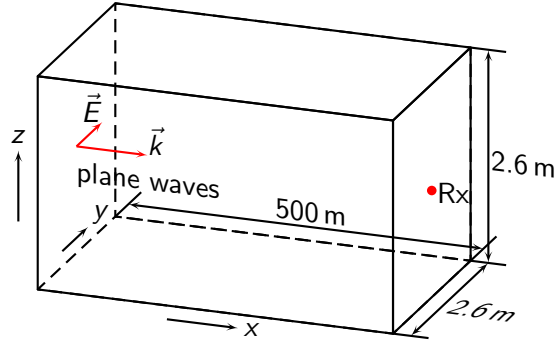
Figure 5.2: Simulation volume for a simulation frequency of 22 GHz. Indicated are radiation and geometry parameters such as the link length (500 m) and the corresponding maximum Fresnel radius (2.6 m at 22 GHz).

the results applying the Welch algorithm. This algorithm divides the input signal in *ini.WelchW* overlapping parts, each including *ini.WelchN* samples. For both parameters table 5.4 lists default values. Following, the method computes the periodogram of the FFTs of each part. Averaging all periodograms and scaling to the sampling frequency returns an estimation for the power spectral density of the input signal. Refer to Welch (1967) for further information. To this end, the simulation runtime is either determined by the variable *ini.time* or by the minimum signal length calculated from the Welch parameters (see table 5.4 and the derived step number from table 5.11).

Parameters describing the rain statistics, dynamics and environmental influence possess values according to table 5.5. The MATLAB class ProbDistUnivParam, emulating a distribution, realised a statistical DSD.

Finally, the simulation stores initial parameters like the iteration value for debugging information, outlined in table 5.6.

After the initialisation of parameters the algorithms computes quantities necessary for the succeeding simulation stages.

parameter name	symbol	variable name	value	unit
distance to receiver	L	ini.d	500	m
source position		ini.source	[]	
position of receiver		ini.drain	$[L\ 0\ 0]$.'	
maximum drop radius		ini.a_max	$4 \cdot 10^{-3}$	m
maximum Fresnel radius	r_{fresnel}	fresnel_max	$\frac{1}{2}\sqrt{\left(\frac{c}{f} \cdot L\right)}$	m
simulation volume	$V_{\text{simulation}}$	ini.mainVolume	$\begin{bmatrix} 0 & L \\ -r_{\text{fresnel}} & r_{\text{fresnel}} \\ -r_{\text{fresnel}} & r_{\text{fresnel}} \end{bmatrix}$	m^3

Table 5.2: Geometry parameters defined in the numerical implementation.

parameter name	symbol	variable name	value	unit
simulation duration		ini.time	5	s
iteration step	Δt	ini.dt	$0.04 \cdot 10^{-3} \widehat{=} 25\,\text{kHz}$	s

Table 5.3: Time parameters defined in the numerical implementation.

parameter name	variable name	value
number of samples per window	ini.welchN	512
number of windows	ini.welchW	8

Table 5.4: Welch analysis parameters defined in the numerical implementation.

parameter name	symbol	variable name	value	unit
drop velocity (depending on radius)	$v(r)$	ini.rainfall	$615.109 \cdot$ $\exp(0.67 \cdot \log(R))$	m/s
rain rate	R	ini.rainrate	0.1	mm/h
Marshall-Palmer parameter	N_0	ini.N0	$16 \cdot 10^6$	$1/\text{m}^3\,\text{m}$
Marshall-Palmer parameter	Λ	ini.Lambda	$8.2 \cdot 10^3 \cdot (R)^{-0.21}$	$1/\text{m}$
DSD	$n(r)$	ini.DSD	ProbDistUnivParam ('exponential', $1/\Lambda$)	
temperature	T	ini.T	25	°C
wind velocity		*ini.wind*	10	m/s

Table 5.5: Rain statistics defined in the numerical implementation.

parameter name	variable name	value
first simulation step	ini.start_sim	1000
iteration of debug information	ini.info_step	100
resolution of look-up table	ini.lookup_res	$1 \cdot 10^{-5}$

Table 5.6: Simulation parameters defined in the numerical implementation.

parameter name	symbol	variable name	value
refractive index	m	ini.m	refer to 3.1.2

Table 5.7: Environmental quantities derived in the numerical implementation.

parameter name	symbol	variable name	value	unit
extension volume	V_{fill}	ini.fillVolume	$\begin{bmatrix} 0 & L \\ -r_{\text{fresnel}} & r_{\text{fresnel}} \\ -r_{\text{fresnel}} & r_{\text{fresnel}} + \Delta z \end{bmatrix}$	m^3

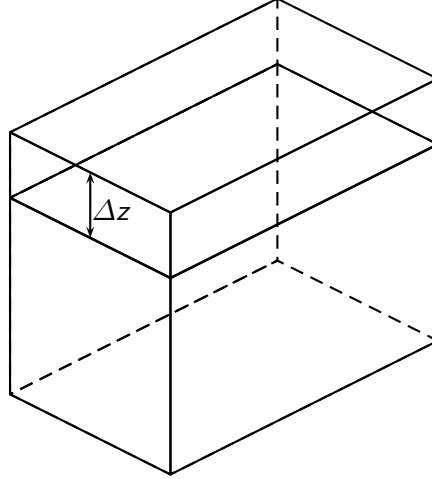Table 5.8: Geometry measures derived in the numerical implementation.

Figure 5.3: Illustration of the supplementary volume surmounting the simulation volume.

By default the algorithm uses a method to derive the refractive index according to Ray (1972) (Table 5.7). Input parameters are temperature and wavelength (compare with section 3.1.2) defined in tables 5.5 and 5.1.

Starting from the second time step, rain drops populate a volume of height Δz on top of the main volume (compare with figure 5.3). The initial calculation step assigns this volume to a variable (compare table 5.8). Δz is considered using the mean velocity $v(r)$ as given in equation (3.1.18), the time resolution Δt and the DSD $n(r)$ by

$$
\begin{aligned}
\Delta z &= 2.2 \cdot v\left(\overline{n(r)}\right) \cdot \Delta t \\
&= 2.2 \cdot v\left(\frac{1}{\Lambda}\right) \cdot \Delta t .
\end{aligned}
$$

(5.3.1)

Furthermore, the algorithm computes additional radiation quantities such as the wave number or the vector between transceiver and receiver (see table 5.9). Additionally, it derives the value of the field strength at the scatterer, without extinction, using the freespace function. This function evaluates the amplitude of the incident ray caused by free space attenuation. It also decreases the waves incident on a scattering object.

Finally, applying Mie scattering the algorithm additionally assigns the parameters

parameter name	symbol	variable name	value	unit
An empty ini.source yields vector transceiver - receiver	r_{rx}	r_rx	ini.drain	m
else vector transceiver - receiver	r_{rx}	r_rx	ini.drain - ini.source	m
wave number	k	ini.k	$2\pi f/c$	$1/\text{m}$
normalised polarisation	$\vec{E}_0/E_0$	ini.k_field	$ini.k\_field/norm(ini.k\_field)$	
amplitude of attenuated direct ray @ receiver		directray		V/m

Table 5.9: Radiation quantities derived in the numerical implementation.

of table 5.10. The ceil operator determines the maximum expansion order *ini.n_max* required for Mie scattering by using the next integer number of the argument in positive direction. Furthermore, the function Mie_abcd_lookup generates the look-up table for the Mie coefficients up to the expansion order *ini.n_max*.

5.3.2 Creation of Drops

The simulation cycle starts by generating drop radii complying with the selected DSD. The MATLAB class ProbDistUnivParam implements a random function taking samples of a defined distribution. For a Marshall Palmer DSD, which is set by default, the distribution follows equation (3.2.2) in section 3.2.3. The total number of drops is calculated according to equation (3.2.3) depending on the populated volume. Occasionally, some chosen drop radii exceed the defined maximum value *ini.a_max*. These radii are interchanged with valid random values.

5.3.3 Volume Population

The second simulation step assigns equally distributed random values to the x, y and z coordinates of the drops. In the first run, values inside the whole simulation volume,

parameter name	variable name	value
Mie factor	miefactor	j/k equation (4.1.24)
maximum size parameter	ini.x_max	$x_{\max} = ini.a\_max \cdot k$
maximum expansion order	ini.n_max	$\text{ceil}(2 + x + 4 \cdot x^{1/3})$ (section 4.1.3)
look-up table: size parameters	*ini.xs*	
look-up table: expansion coefficients	*ini.abcd*	

Table 5.10: Simulation quantities derived in the numerical implementation.

parameter name	variable name	value
total number of simulation steps	*ini.welchSteps*	$\frac{ini.welchW+1}{2} \cdot ini.welchN$

Table 5.11: Welch algorithm quantities derived in the numerical implementation.

whose extent is stored in the variable *ini.mainVolume*, are chosen. In succeeding cycles the Volume *ini.fillVolume* supplies the value extension. As stated before, this ensures continuous statistically distributed rain.

5.3.4 Drop Selection

During the initialisation step, described in section 5.3.1, a volume relevant for the scattering process is stored in the *ini.main Volume* variable. The drop selection step chooses all drops lying inside this volume. This ensures that both drops that will leave the volume and drops that will enter the volume in the next time step are neglected. By adjusting *ini.mainVolume*, the scattering may be performed at drops inside more advanced volumes like the Fresnel ellipsoid.

Furthermore, the selection step removes disposable items from the collection of drops. For instance, if one only applies vertical fall velocity, drops with z values smaller than the main volume are erased.

To summarise, this chapter illustrated the realisation of the synthetic rain field and the simulation of an electromagnetic wave propagating through it. After a short overview of the whole algorithm, section 5.2 outlined the scattering step in greater detail extending the knowledge of the preceding chapters with additional theory.

Following, the individual simulation steps including initial definitions and derived simulation quantities were presented. The accumulation continues until stop criteria, determined either by the simulation time or by the number of runs required by the selected analysis method, are satisfied.

6 Simulation Results

Following from the description of the model on drop scale in the last section, this section describes and analyses the results obtained by its application. For all individual computation runs leading to these results the initial values, except polarisation and rain rate, remain constant. Table 6.1 lists an overview of the simulation parameters. The specific simulations use the Marshall-Palmer DSD described in section 3.2.3 and the terminal drop velocity according to section 3.1.3. An illustration of the geometric parameters was given in figure 5.2.

The incident field is either horizontally (y) or vertically (z, in drops fall direction) polarised, propagating through rain with rates from $0.1\,\mathrm{mm/h}$ to $100\,\mathrm{mm/h}$. First, this section shows and analyses graphs displaying amplitude and phase of the signal resulting from the simulations for the two polarisation directions and four selected rain rates of $0.1\,\mathrm{mm/h}$, $1\,\mathrm{mm/h}$, $10\,\mathrm{mm/h}$ and $100\,\mathrm{mm/h}$. Both the co- and cross-polarised components of the electric fields are presented. These signals are analysed concerning their spectral and statistical as well as their temporal behaviour.

Focussing on the purpose of this work, the results highlight the impact of a rain field disturbing electromagnetic propagation. The plotted data involve the two signal components namely the coherent signal and the incoherent signal described in detail in section 4.2 and section 4.3.

The first component, apparent as the attenuation of electromagnetic waves due to a rain field, directly influences everyday life. Weaker sight, decreased quality of terestrial or satellite television, and a reduction of the reliability of vehicle-interval radar during rain periods indicate a direct correlation of the signal level and the rain rate. Many publications, such as cited in section 4.2, justify this subjective impression. Shedding light on the second aspect unveils a deeper insight into the statistical rain process. The drop size distribution, the statistical measure of rain, dynamically influences the incoherent signal. The direct relation of drop size to velocity effects a characteristric Doppler pattern in the resulting frequency spectrum according to the corresponding drop population.

However, in a real world rain event the rain parameters change. This causes varying characteristics during the rain process. Keeping the rain characteristics constant this work evaluates a statistically chosen set of 2304 datapoints to yield a footprint of a specific configuration of characteristics applying the Welch algorithm (compare section 5.3).

6.1 Time Signal

The application of the algorithm presented in the last chapter directly provides a signal during the whole simulation time. The algorithm generates a signal for co- and cross-polarisation containing information on amplitude and phase of the received field. The graphs in the following subsections show either amplitude or phase of the field. An additional polar plot draws the complex phasor including both measures for a rain rate of $0.1\,\mathrm{mm/h}$. Analysis of the co-polar case is performed for the total signals as well as for the incoherent signals only.

6.1.1 Co-Polarisation

Figure 6.1 shows the received time signal of waves propagating through a rain field. The signal plotted in the left plot originates from the horizontally polarised electric field at the receiver for a horizontal polarised incident field. The right graph denotes the same for vertical polarisation. In this and the succeeding plots the curves draw values

Radiation parameters	
frequency	$22 \cdot 10^9\,\mathrm{Hz}$
polarisation	y or z
direction of propagation	x
Amplitude of electric field	$1\,\mathrm{V/m}$
Geometry parameters	
distance to receiver	$500\,\mathrm{m}$
maximum drop radius	$4 \cdot 10^{-3}\,\mathrm{m}$
incident waves	plane
Time parameters	
midrule iteration step	$0.04 \cdot 10^{-3}\,\mathrm{s}$
Analysis parameters	
number of samples per Welch window	512
number of Welch windows	8
resulting total time	$0.163\,84 \cdot 10^{-3}\,\mathrm{s}$
Simulation parameters	
temperature	$25\,^\circ\mathrm{C}$
resolution of look-up table	$1 \cdot 10^{-5}$
first simulation step	1000

Table 6.1: Simulation parameters leading to the results analysed in this chapter. An illustration of the geometry can be found in figure 5.2.

for four exemplarily selected rain rates. The line style is black solid for 0.1 mm/h, blue dashed for 1 mm/h, dotted green for 10 mm/h and orange dashed dotted for 100 mm/h, respectively. Examining the signal shapes, a decrease of signal level with rising rain rate is observable. The noisy signals, expected in the presence of a statistical rain field, are not visible.

In contrast, when suppressing the coherent signals and only plotting the incoherent signals in figure 6.2 these signals show greater disturbances. The incoherent signals result from the total number of scattering objects. However, although these signals are 120 dB lower than the total signals, they again are quite even. Nevertheless, some disturbances are visible. Both total and incoherent signals serve as input for analyses concerning spectrum and statistical measures in the next section.

In addition to the amplitude components in figure 6.1 and figure 6.2, figure 6.3 and figure 6.4 show the phase values of the total and the incoherent signals. To support the insight on the effects caused by rain, figure 6.3 shows fluctuations of the phase around its mean value. Referring to figure 4.4, the mean value accounts for the phase of the coherent signals (large black arrow). The fluctuations originate from the accumulated contributions of the scattered signals of the individual drops. Figure 4.4 shows this contribution in detail. In both figures, in contrast to the figures showing the amplitudes, a statistical influence is visible causing the noise.

Additionally, a phase change as indicated in figure 4.4 is observed in the total phase. The slope of the phase increases with increasing rain rate. For a low rain rate of 0.1 mm/h the curve is almost constant, developing towards a steep slope for 100 mm/h.

Although, the statistical nature lacks noisy effects on the co-polar signals, one expects a significant impact on the cross-polar component, which is examined in the next subsection.

Figure 6.5 shows amplitude and phase plotted jointly in the complex plane. Preliminary considerations explain the graphs. The phasor of an undisturbed received field would be rotating in the complex plane formed by a constant amplitude and a linearly evolving phase. Therefore, a repeated circle would be observed, from which figure 6.5 is clearly different. Nevertheless, the plot includes sections of nearly circular behaviour, for instance next to the 150° label in the upper graph.

In this plot, jumps of varying height interrupt sections of rotating phase. In contrast, simulations not shown using rain drop radii up to 2 mm record uninterrupted data. In conclusion, large drops seem to cause the jumps. Indeed, scattering amplitudes of large drops are high and alternate with scattering angle as illustrated in figure 4.9.
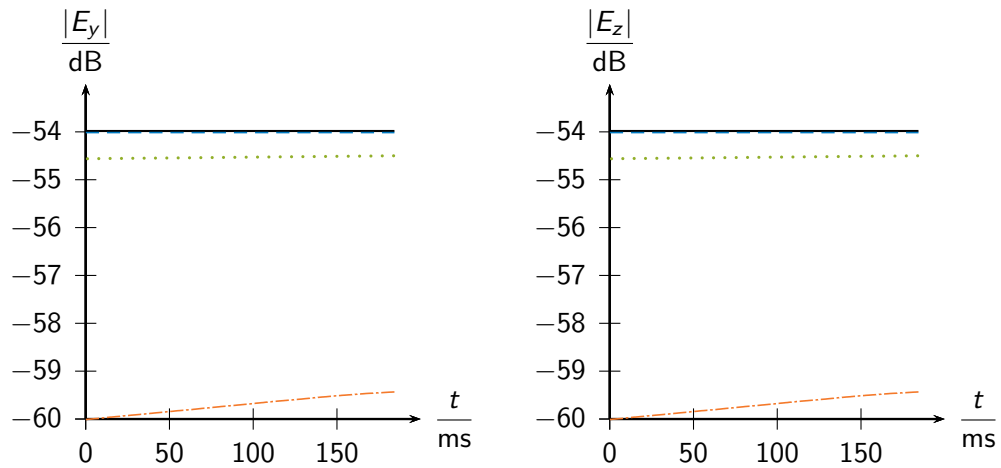
Figure 6.1: Amplitude of total received electric field related to the field strength of the incident field at $z = 0$. The left plot shows the y-polarised received component for a y-polarised incident field. On the right hand side, the same is drawn for z polarisation. A black solid line denotes $0.1\,\mathrm{mm/h}$, blue dashed $1\,\mathrm{mm/h}$, dotted green $10\,\mathrm{mm/h}$ and orange dashed dotted $100\,\mathrm{mm/h}$, respectively.
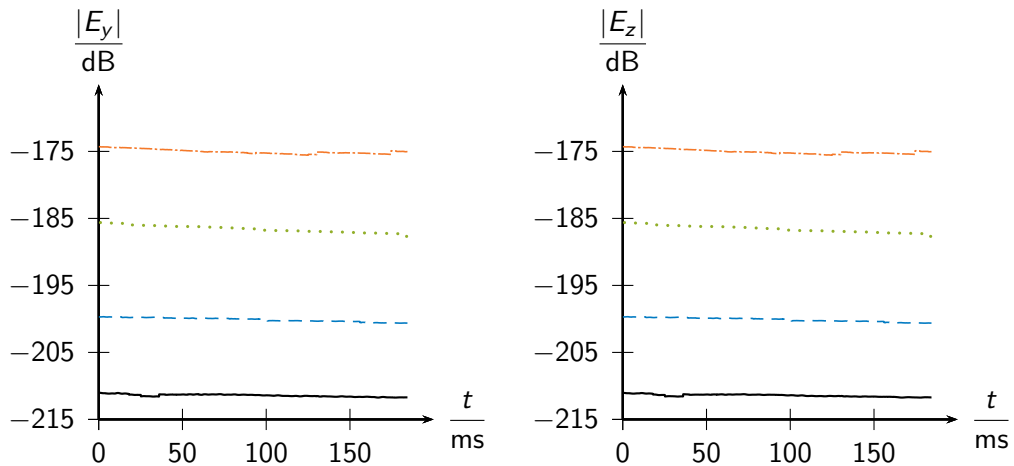
Figure 6.2: Amplitude of incoherent received electric field related to the field strength of the incident field at $z = 0$. The left plot shows the y-polarised received component for a y-polarised incident field. On the right hand side, the same is drawn for z polarisation. A black solid line denotes $0.1\,\mathrm{mm/h}$, blue dashed $1\,\mathrm{mm/h}$, dotted green $10\,\mathrm{mm/h}$ and orange dashed dotted $100\,\mathrm{mm/h}$, respectively.
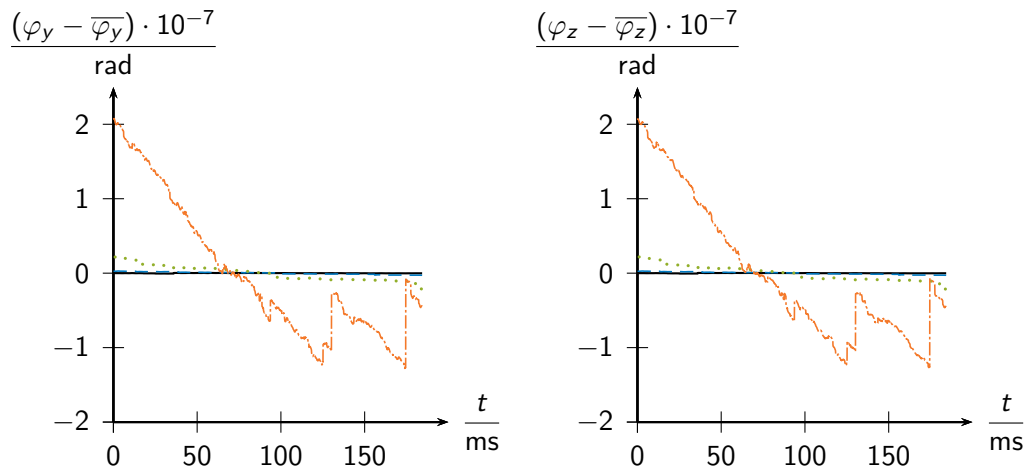
Figure 6.3: Phase of total received electric field. The left plot shows the *y*-polarised received component for a *y*-polarised incident field. On the right hand side, the same is drawn for *z* polarisation. A black solid line denotes $0.1\,\mathrm{mm/h}$, blue dashed $1\,\mathrm{mm/h}$, dotted green $10\,\mathrm{mm/h}$ and orange dashed dotted $100\,\mathrm{mm/h}$, respectively.

Figure 6.4: Phase of incoherent received electric field. The left plot shows the *y*-polarised received component for a *y*-polarised incident field. On the right hand side, the same is drawn for *z* polarisation. A black solid line denotes $0.1\,\mathrm{mm/h}$, blue dashed $1\,\mathrm{mm/h}$, dotted green $10\,\mathrm{mm/h}$ and orange dashed dotted $100\,\mathrm{mm/h}$, respectively.

Figure 6.5: Phasor plot of received electric field around mean value at a rain rate of 0.1 mm/h. Top: Plot for *y* polarisation, Bottom: Plot for *z* polarisation

6.1.2 Cross-Polarisation

The simulations described in the last chapter compute both co- and cross-polar components of the received electric field. Figure 6.6 shows plots of the cross-polar signals with horizontal and vertical polarisation for the same four rain rates as for the co-polar plots in the last subsection. The statistical rain clearly affects the cross-polar fields. The scattering at statistically distributed drops leads to the noisy signals.

This seems to be a discrepancy which relates to the well known fact of missing cross-polar components of a field scattered by a spherical object. However, scattering at drops with scattering planes tilted with respect to the horizontal cause these contributions. Static statistical approaches assume a symmetrical distribution of rain drops. Therefore, a scattered component from a drop with tilted plane cancels the field of a symmetrical one with respect to the horizontal plane between transceiver and receiver.

In contrast to the co-polar case, total and incoherent fields coincide in the cross-polar case because of the perpendicular polarisation of the incident field. The data plotted in figure 6.6 shows no obvious difference between both incident polarisations resembling to the co-polarised results.

Graphs of the phase components in figure 6.7 show fluctuating phases. Unaffected by the direct incident field, the mean value is, in contrast to the one for the co-polar phase, around zero.

Figure 6.8 displays amplitude and phase of the cross-polar signal from a rain rate of $0.1\,\mathrm{mm/h}$ for the co-polar signal, analogous to figure 6.5. Repeating the argument in the last section, a unperturbed signal would describe a circle in the graph. In the co-polar case, one observes strong perturbations of the signal. The cross-polar phase produces a curve running through different deformed ellipses without large sudden variations. In summary, amplitude and phase of the received field behave like a response to incident waves observing steady but random disturbances, while propagating through a medium.
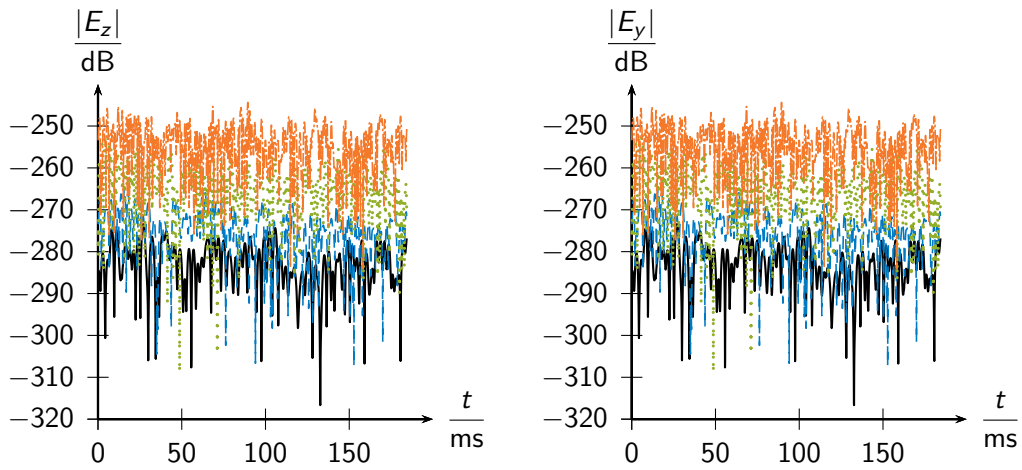
Figure 6.6: Amplitude of cross-polar received electric field related to the field strength of the incident field at $z = 0$. The left plot shows the z-polarised received component for a y-polarised incident field. On the right hand side, the same is drawn for an incident field in z polarisation. A black solid line denotes 0.1 mm/h, blue dashed 1 mm/h, dotted green 10 mm/h and orange dashed dotted 100 mm/h, respectively.
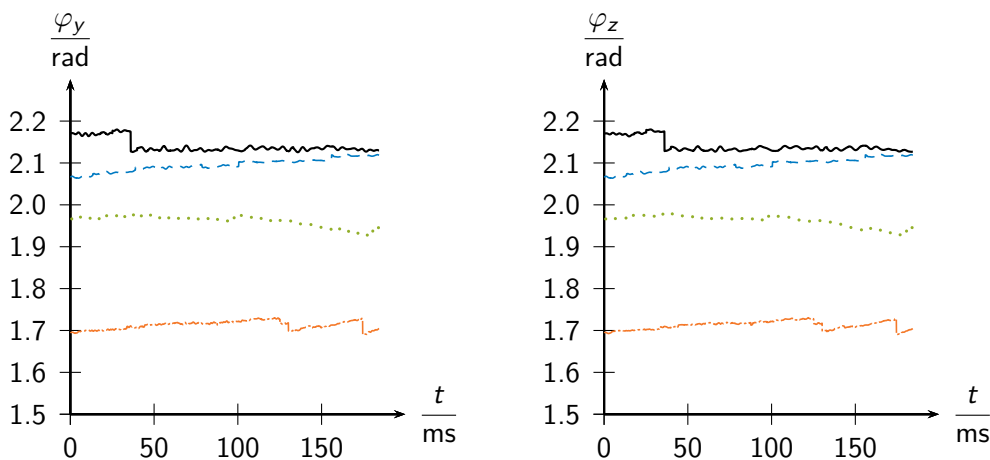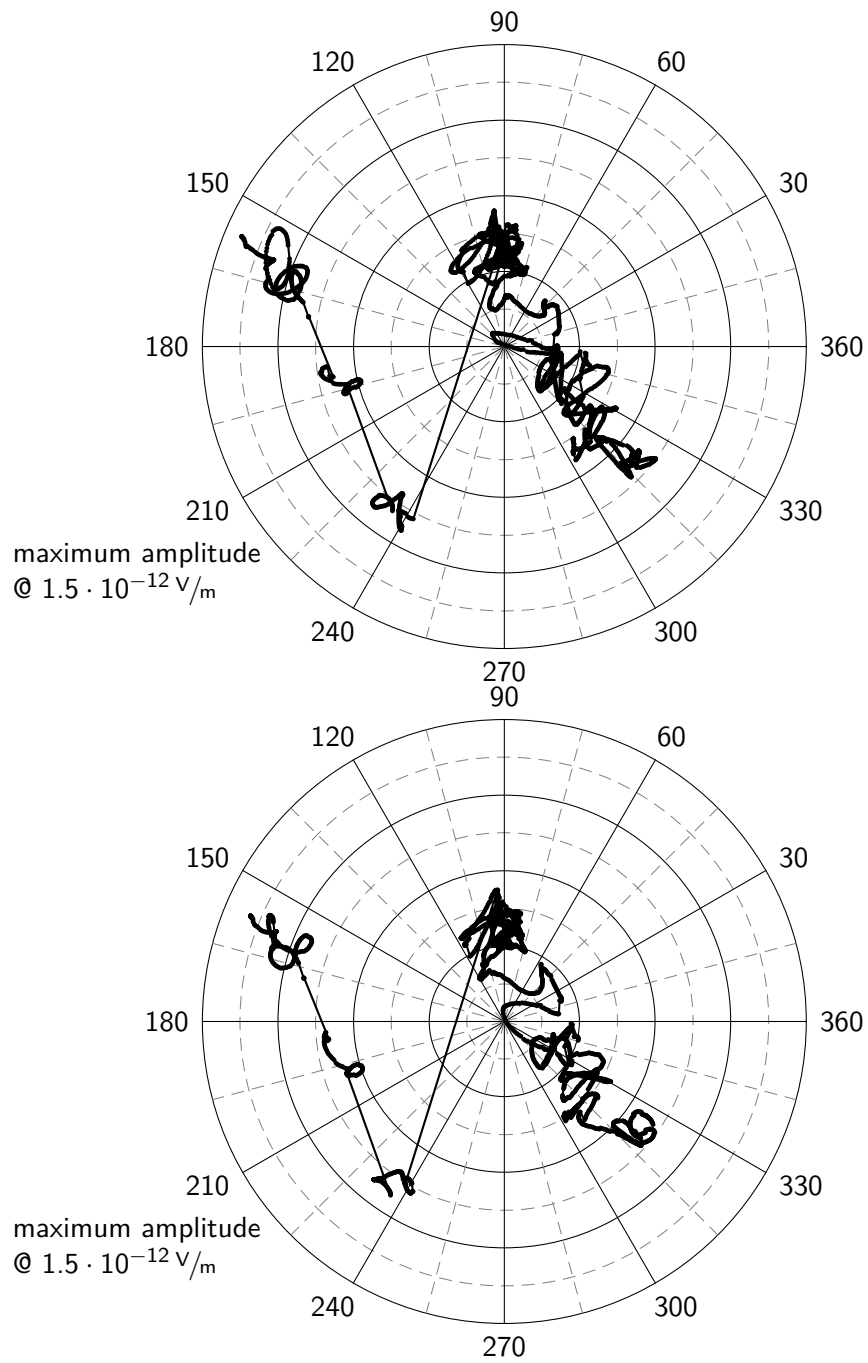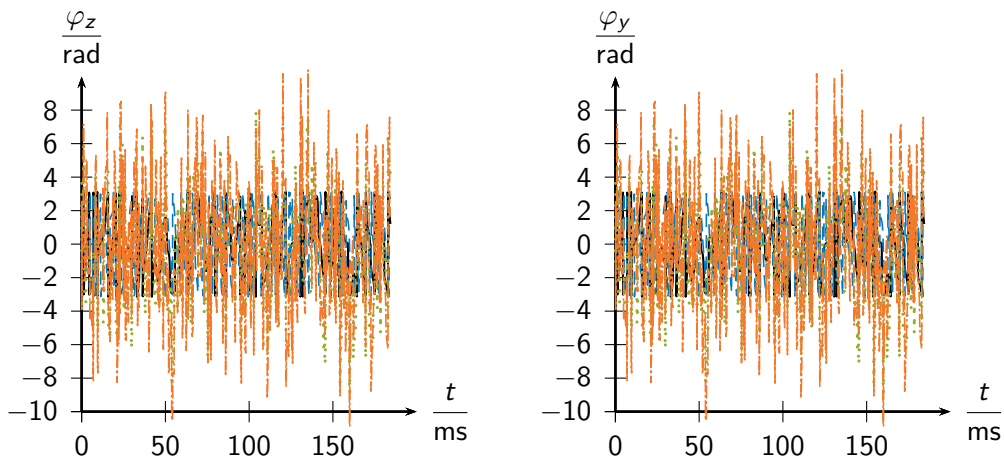

Figure 6.7: Phase of cross-polar received electric field. The left plot shows the z-polarised received component for a y-polarised incident field. On the right hand side, the same is drawn for incident z polarisation. A black solid line denotes 0.1 mm/h, blue dashed 1 mm/h, dotted green 10 mm/h and orange dashed dotted 100 mm/h, respectively.

Figure 6.8: Phasor of cross-polar received electric field at a rain rate of 0.1 mm/h. The upper plot shows the z-polarised received component for a y-polarised incident field. At the button, the same is drawn for incident z polarisation.
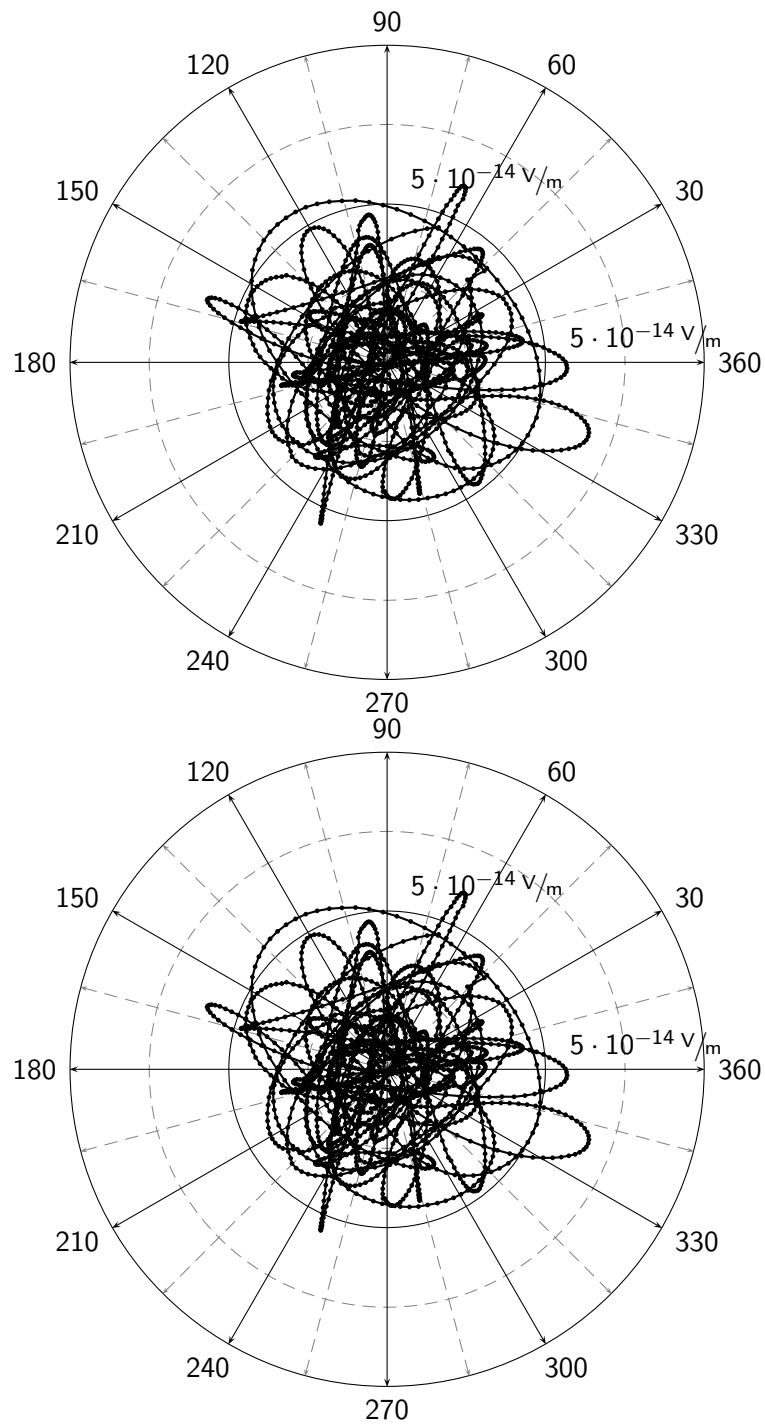
6.2 Spectrum

The analysis of the time signals given in the last section is possible with a number of methods. First, this section analyses the spectrum of co- and cross-polarised received field given in figure 6.9 to figure 6.12. Figure 6.9 shows the spectrum of the incoherent co-polar signal. Around zero frequency shift the power increases from $-227\,\mathrm{dB}$ to $-187\,\mathrm{dB}$ for increasing rain rates. The rise in power results from the increase of scattering objects contributing to the received field. The sharp maximum shows equal extent for all rain rates. Enlarging the central region confirms this assumption. Only waves directly travelling to the receiver observe no frequency shift. Although the graph shows only the incoherent and not the total signal, the strongest contribution results from these waves. Figure 6.10 shows the similarity of both horizontal and vertical polarisation, except for some minor differences. One expects the central peak to broaden because of the Doppler effect. However, finding an augmentation is difficult due to its intensity.

The cross-spectrum is drawn in figure 6.11 and expanded around zero in figure 6.12. At zero frequency shift, the received power drops. The maximum power successively increases from $-295\,\mathrm{dB}$ for a rain rate of $0.1\,\mathrm{mm/h}$ to $-270\,\mathrm{dB}$ for $100\,\mathrm{mm/h}$ at frequencies increasing with increasing rain rates. According to an exponential DSD (section 3.2.3) larger drops correlate with higher rain rates. Therefore, considering the relation of the terminal velocity larger drops are faster than smaller ones, causing larger Doppler shifts.

Comparing the signal levels of co- and cross-polarised field shows a significant power difference of around $60\,\mathrm{dB}$ to $80\,\mathrm{dB}$. The design of receivers with both huge dynamics and blocking of signal crosstalk, able to distinguish between the power levels of co- and cross-polarisd signals, is challenging. Therefore, measurements might be ambitious if not impossible. However, investigations with more realistic drop shapes, in contrast to spherical drops, should result in larger signal levels of the coherent field alleviating the receiver design.
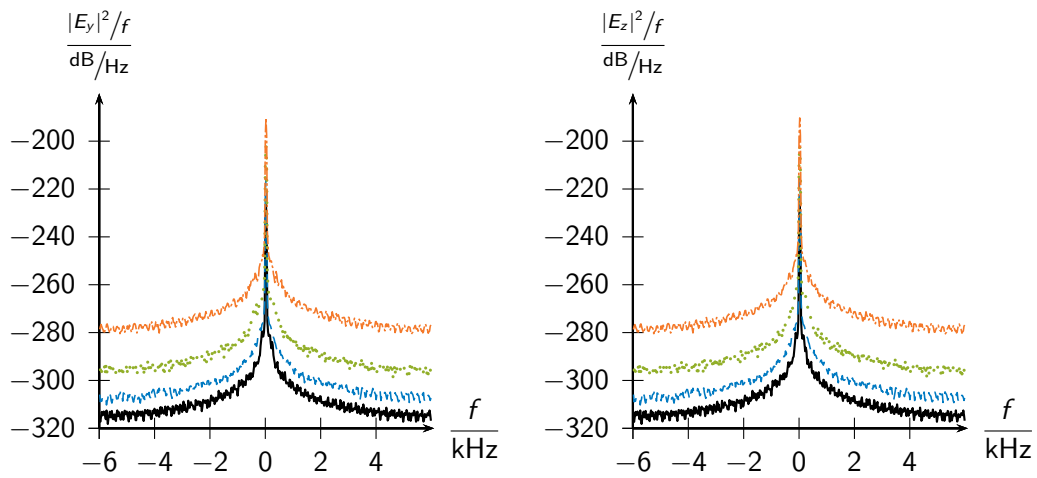
Figure 6.9: Spectral density of incoherent received electric power related to the power of the incident field at $z = 0$. The left plot shows the y-polarised received component for a y-polarised incident field. On the right hand side, the same is drawn for z polarisation. A black solid line denotes $0.1\,\mathrm{mm/h}$, blue dashed $1\,\mathrm{mm/h}$, dotted green $10\,\mathrm{mm/h}$ and orange dashed dotted $100\,\mathrm{mm/h}$, respectively.
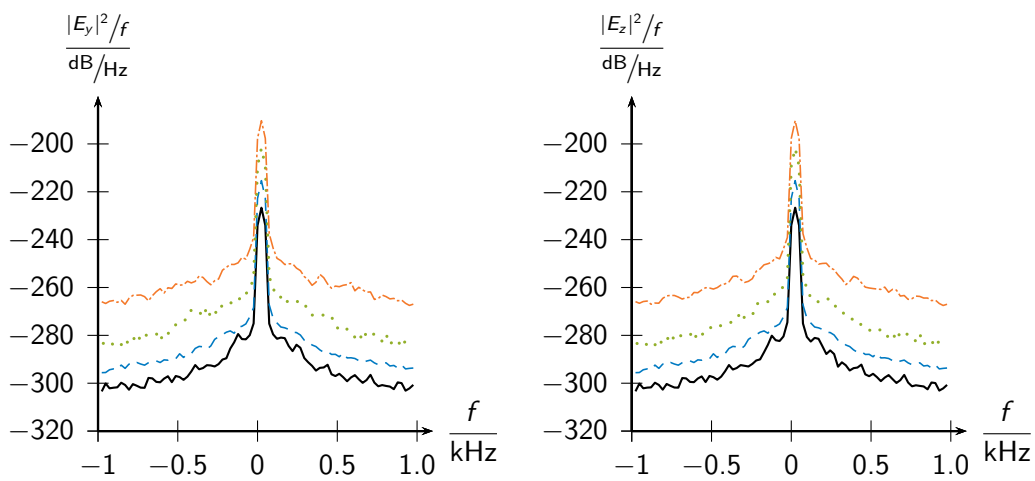
Figure 6.10: Zoom of figure 6.9 around zero.
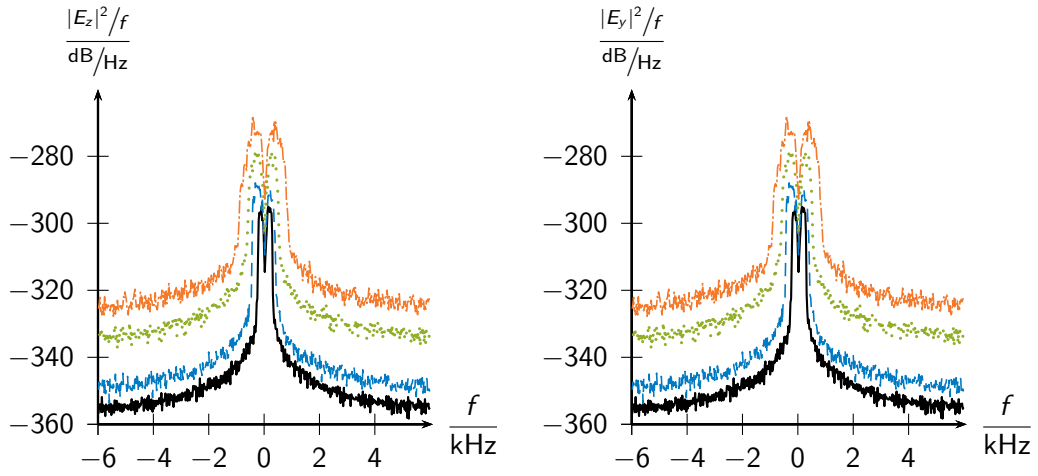
Figure 6.11: Spectral density of cross-polar received electric power related to the power of the incident field at $z = 0$. The left plot shows the z-polarised received component for a y-polarised incident field. On the right hand side, the same is drawn for incident z polarisation. A black solid line denotes $0.1\,\mathrm{mm/h}$, blue dashed $1\,\mathrm{mm/h}$, dotted green $10\,\mathrm{mm/h}$ and orange dashed dotted $100\,\mathrm{mm/h}$, respectively.
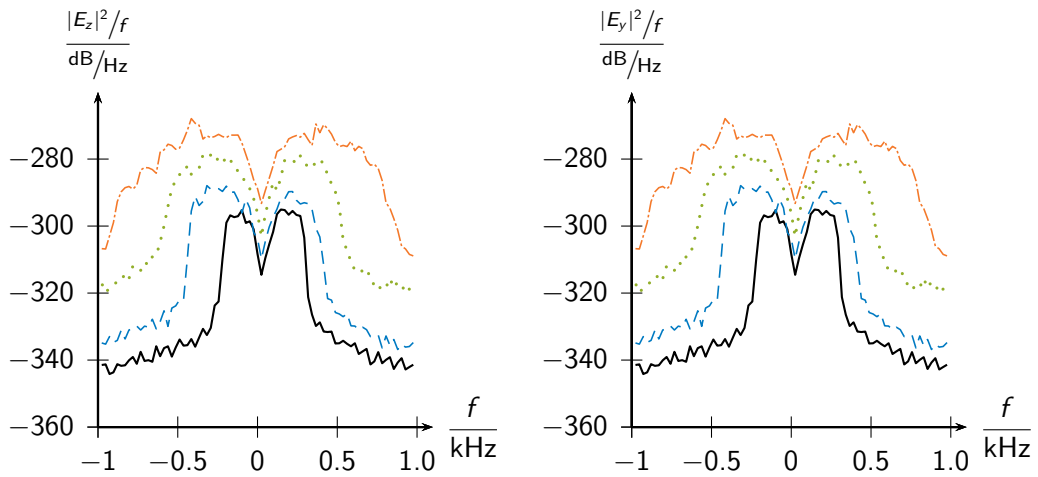
Figure 6.12: Zoom of figure 6.11 around zero.

6.3 Statistical Analysis

Various measures analyse the statistical properties of a signal. This section gives results of the analysis of the received field concerning amplitude and phase. The first two subsections apply the auto-correlation of the signal and the distribution of phases. The first subsection presents evaluations of the co-polar signal, while the second sheds light on the results in cross-polarisation. Finally, the last subsection presents statistical investigations of all simulated rain rates varying from 0.1 to 100 $^{mm}/_{h}$.

6.3.1 Co-Polarised Statistics

This subsection starts the statistical analysis with the auto-covariance function of the received signal and the distribution of the phases of the total and incoherent signal for the four rain rates and 0.1 $^{mm}/_{h}$, 1 $^{mm}/_{h}$, 10 $^{mm}/_{h}$ and 100 $^{mm}/_{h}$ plotted in figure 6.5 and figure 6.8 in section 6.1.1.

The auto-covariance function denotes the auto-correlation of a signal around its mean value

$$c_{xx}(m) = \sum_{n=0}^{N-|m|-1} (x_{n+m} - \overline{x})(x_n^* - \overline{x^*}) \tag{6.3.1}$$

and thus is symmetric around zero.

Figure 6.13 and figure 6.14 show calculation results for total and incoherent signal, respectively. Utilising the axial symmetry of the auto-covariance function, the figures plot the results for horizontal incident polarisation on the negative x-axis and for vertical polarisation along the positive x-axis.

The auto-covariance of the total signal shown in figure 6.13 indicates the received signal to be of coloured noise. This conclusion contrasts our expectation to observe white noise caused by the randomness of the rain field. However, the coherent part of the total electric field diminished other statistical contributions leading to the colouring.

The auto-covariance of the incoherent signal is plotted in figure 6.14. Although the plots for low rain rates show noisy character of the signal, this evolves to coloured noise with increasing rain rates.

Figure 6.15 and figure 6.16 show the distribution of phases of the incoherent signal. Not surprisingly, a very high contribution of a single phase value due to the direct scattering path is observable.
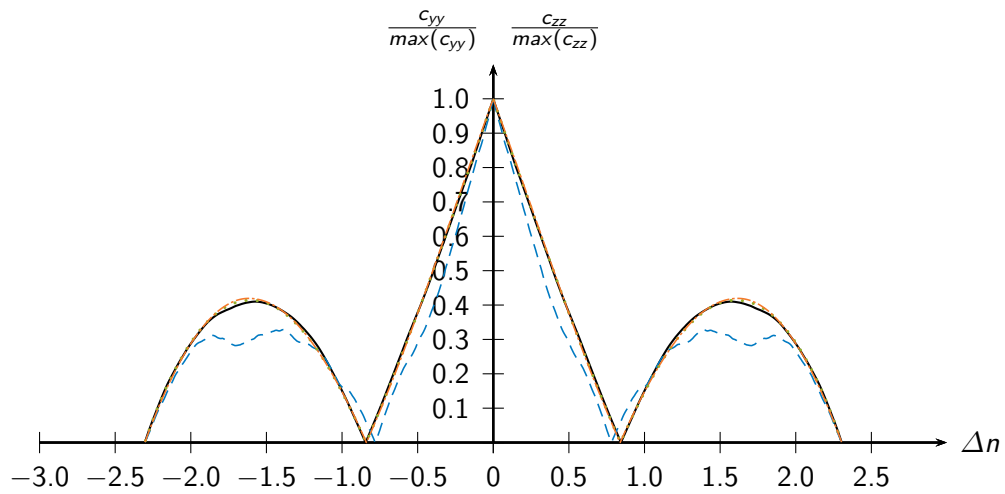
Figure 6.13: Auto-covariance of total received electric field. Data points for negative x values show the y-polarised received component for a y-polarised incident field. Positive x values yield the same for z polarisation. A black solid line denotes 0.1 mm/h, blue dashed 1 mm/h, dotted green 10 mm/h and orange dashed dotted 100 mm/h, respectively.


Figure 6.14: Auto-covariance of incoherent received electric field. Data points for negative x values show the y-polarised received component for a y-polarised incident field. Positive x values yield the same for z polarisation. A black solid line denotes 0.1 mm/h, blue dashed 1 mm/h, dotted green 10 mm/h and orange dashed dotted 100 mm/h, respectively.
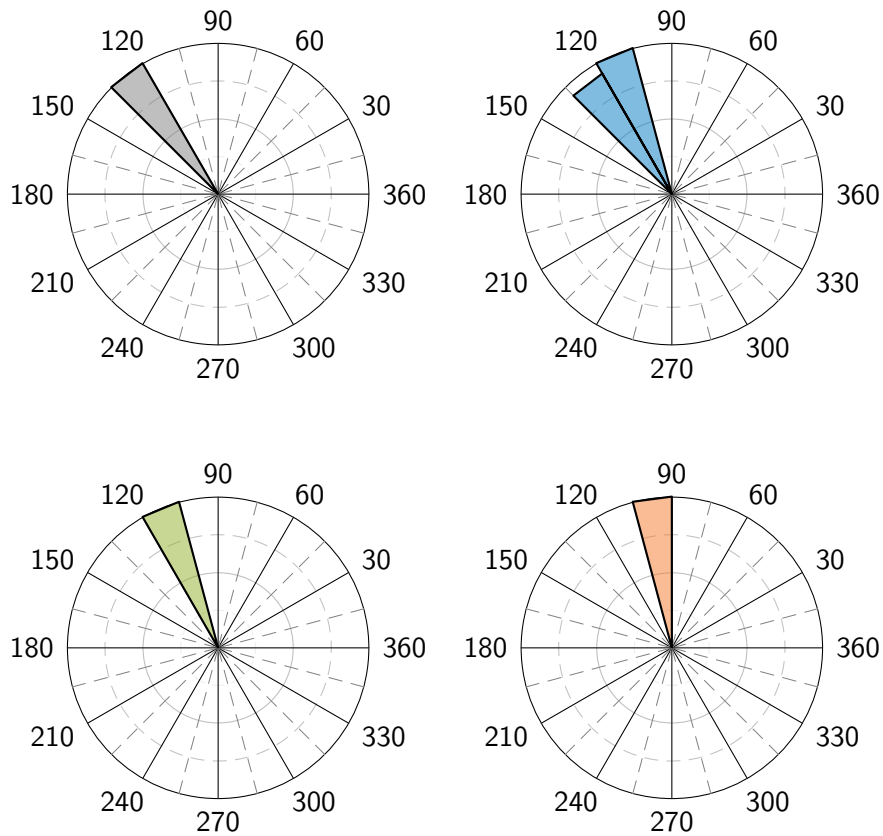
Figure 6.15: Histograms of phases of incoherent received electric field with both incident and received field in *y* polarisation. The plots from upper left to lower right display the histograms for the selected rain rates. The grey color (upper left) denotes 0.1 mm/h, blue (upper right) 1 mm/h, green (lower left) 10 mm/h and orange (lower right) 100 mm/h, respectively. The histograms show the numbers of phase samples, normalized to the number in the most populated interval, in intervals from 0° to 360° with a width of 15°.

Figure 6.16: Histograms of phases of incoherent received electric field with both incident and received field in zpolarisation. The plots from upper left to lower right display the histograms for the selected rain rates. The grey color (upper left) denotes 0.1 mm/h, blue (upper right) 1 mm/h, green (lower left) 10 mm/h and orange (lower right) 100 mm/h, respectively. The histograms show the numbers of phase samples, normalized to the number in the most populated interval, in intervals from 0° to 360° with a width of 15°.

6.3.2 Cross Polarised Statistics

Figure 6.17 shows the auto-covariance for the co-polarised signal. Analogous to figure 6.13 the plot on the left denotes results for horizontal polarisation and on the right for vertical polarisation, respectively.

The curve displays the results for a white noise signal. This is characterised by a sharp peak at zero and decorrelation at other sample shifts. A closer look reveals deviations around zero for different rain rates. For a rain rate of $0.1\,\mathrm{mm/h}$ the plot shows small side lobes around zero, decreasing for $1\,\mathrm{mm/h}$. Rain rates of $10\,\mathrm{mm/h}$ or $100\,\mathrm{mm/h}$ induce more rain drops, improving the implementation of the statistics.

Figure 6.18 and figure 6.19 show the distribution of phases for the cross-polar signal. One observes nearly uniform distributions of all considered phase ranges. The uniformity increases with increasing rain rates for the same reason as the development of white noise in the auto-covariance.
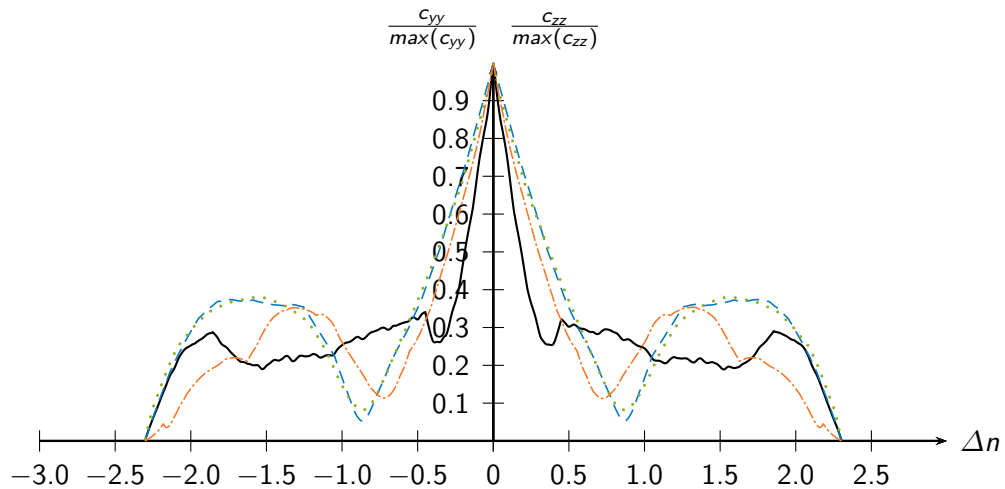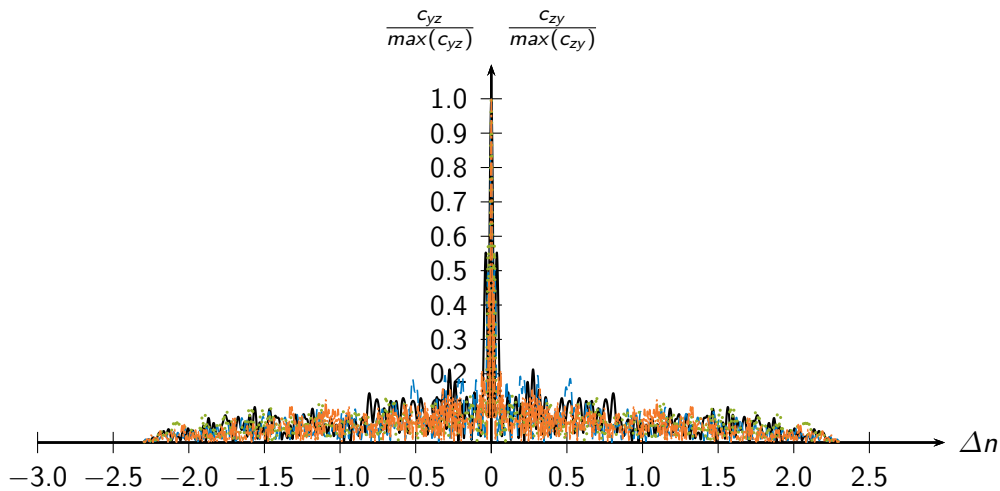

Figure 6.17: Auto-covariance of cross-polarised received electric field. Data points for negative x values show the z-polarised received component for a y-polarised incident field. Positive x values yield the same for the incident field in z polarisation. A black solid line denotes $0.1\,\mathrm{mm/h}$, blue dashed $1\,\mathrm{mm/h}$, dotted green $10\,\mathrm{mm/h}$ and orange dashed dotted $100\,\mathrm{mm/h}$, respectively.
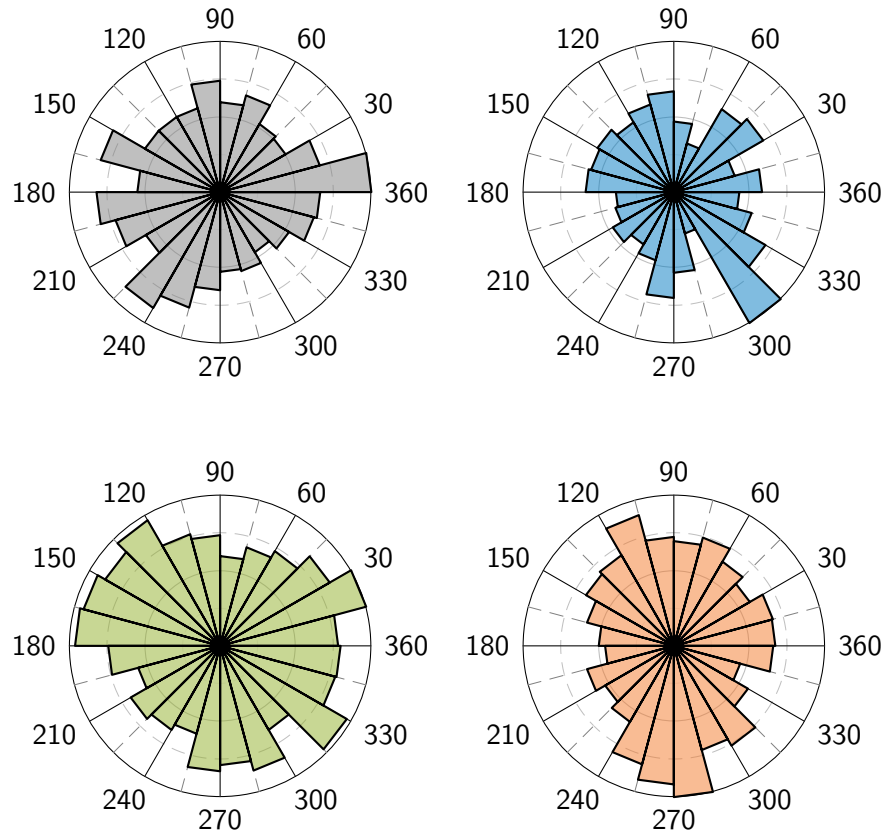
Figure 6.18: Histograms of phases of cross-polar received electric field with *y*-polarised incident and received *z* polarisation. The plots from upper left to lower right display the histograms for the selected rain rates. The grey color (upper left) denotes 0.1 mm/h, blue (upper right) 1 mm/h, green (lower left) 10 mm/h and orange (lower right) 100 mm/h, respectively. The histograms show the numbers of phase samples, normalized to the number in the most populated interval, in intervals from 0° to 360° with a width of 15°.
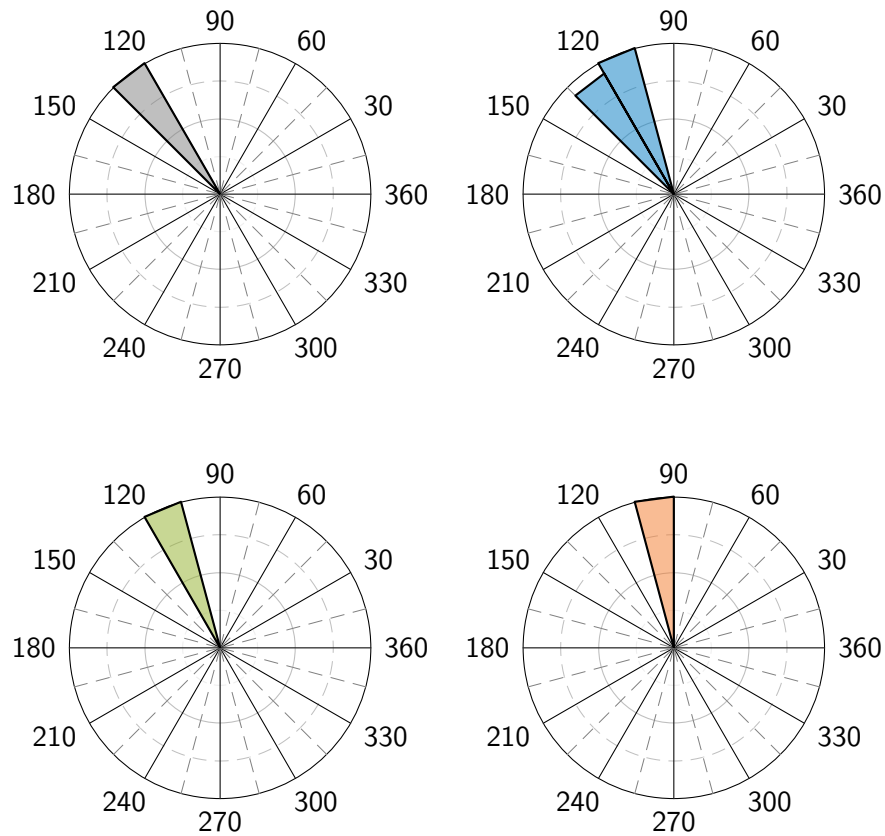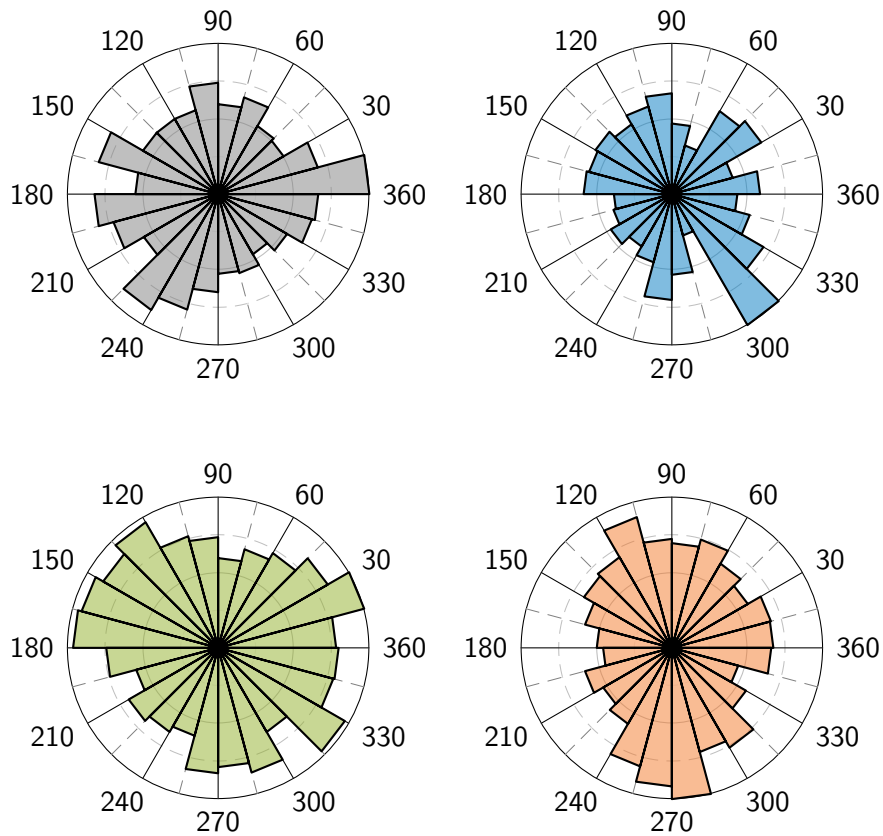
Figure 6.19: Histograms of phases of cross-polar received electric field with *z*-polarised incident and *y*-polarised received field. The plots from upper left to lower right display the histograms for the selected rain rates. The grey color (upper left) denotes 0.1 mm/h, blue (upper right) 1 mm/h, green (lower left) 10 mm/h and orange (lower right) 100 mm/h, respectively. The histograms show the numbers of phase samples, normalized to the number in the most populated interval, in intervals from 0° to 360° with a width of 15°.

6.3.3 Statistics for Rain Varying from Drizzle to Monsoon

The last subsections only characterised results for four selected rain rates for clarity and brevity. Figure 6.20 and figure 6.21 plot statistical measures of the amplitude of the total received signal for all simulated rain rates. The graphs show the mean value of the signal indicated by a horizontal black line. The blue box stretches between the third and first quartile. The red curves give the minimal and maximal amplitude. In conclusion, the plots show an almost linear decrease of the signal with rain rate. Furthermore, the variation of the signal, indicated with the quartile range, increases.

Figure 6.22 illustrates the resulting amplitudes compared with values calculated using the ITU Recommendation P.838. The relation of attenuation A in $^{dB}/_{km}$ on rain rate R in $^{mm}/_{h}$ is approximated as power law, where the equation at 22 GHz for horizontal polarisation is

$$A = 0.1155 \cdot R^{1.0329} \tag{6.3.2}$$

and for vertical

$$A = 0.1170 \cdot R^{0.97} . \tag{6.3.3}$$

In the plot the upper line corresponds to the vertical polarisation while the lower line illustrates the attenuation for horizontal polarisation. The different values result from the special shapes of the rain drops as outlined in section 3.1.1. The values resulting in this work are found in between both lines due to the applied spherical approximation.

Table 6.2 completes the statistical analysis with a list of statistical moments of the amplitudes. Its distributions are almost symmetric (skewness close to zero) and mesokurtic with a kurtosis near zero. Additionally, the variance indicates a broadening of the signal with increasing rain rate. This is effected by increasing drop size with increasing rain rate leading to higher Doppler shifts.

This section presented results of simulations described in chapter 6. First it showed the time signal generated by the algorithm. The signal is available both for horizontal and for vertical incident polarisation as well as co- and cross-polarised received field.

Rain rate ($\mathrm{mm/h}$)	Mean (dB)	Variance (dB)	2nd Moment (skewness) (dB)	3rd Moment (kurtosis) (dB)
0.1	1.899615e-03	1.415887e-16	-1.208096e-25	3.543197e-32
0.2	1.898851e-03	1.122442e-15	-4.594450e-24	2.186680e-30
0.3	1.898012e-03	2.993605e-15	-3.410165e-24	1.678679e-29
0.4	1.897102e-03	5.859313e-15	-1.823271e-25	6.216370e-29
0.5	1.896147e-03	1.066411e-14	-1.455376e-23	2.185620e-28
0.6	1.895200e-03	2.104896e-14	1.622745e-22	8.098270e-28
0.7	1.894210e-03	3.248516e-14	3.627646e-22	1.804783e-27
0.8	1.893190e-03	4.194032e-14	1.914696e-22	3.135928e-27
0.9	1.892185e-03	5.468991e-14	2.223782e-22	5.385304e-27
1	1.891120e-03	6.535324e-14	1.435522e-21	7.810750e-27
2	1.879960e-03	4.123498e-13	5.238940e-21	3.017583e-25
5	1.844290e-03	3.570758e-12	6.368377e-20	2.343037e-23
10	1.783390e-03	1.527087e-11	4.645092e-20	4.107922e-22
15	1.723894e-03	3.443218e-11	4.189269e-18	2.186124e-21
20	1.665842e-03	5.976545e-11	1.120137e-17	6.362668e-21
30	1.556180e-03	1.199693e-10	-1.110956e-17	2.551874e-20
40	1.453685e-03	1.813603e-10	3.673367e-17	5.817585e-20
50	1.360792e-03	2.467727e-10	-1.282706e-16	1.079111e-19
60	1.273065e-03	3.048570e-10	-1.873688e-16	1.636114e-19
100	9.829578e-04	4.222043e-10	-4.480391e-16	3.101408e-19

Table 6.2: List of moments of the field amplitudes for a *y*-polarised incident and received field

Figure 6.20: Amplitude distributions of total received electric field in y polarisation. Indicated are the maximum and minimum field values, the first and third quartile as well as the mean value.
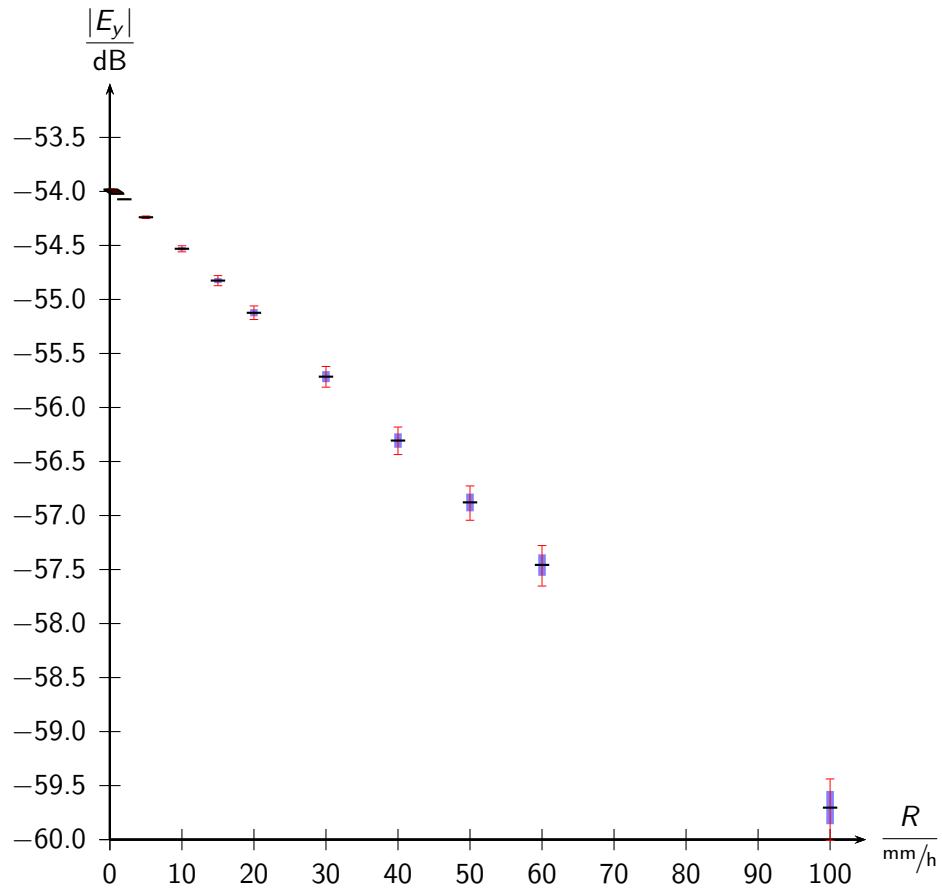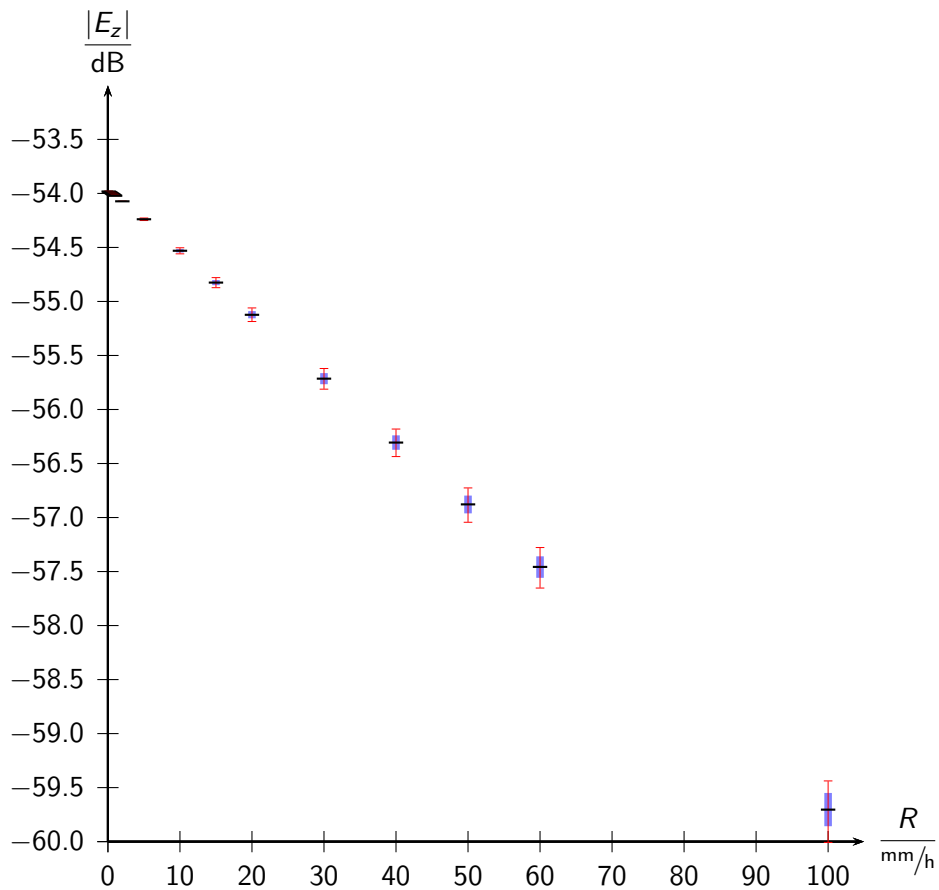
Figure 6.21: Amplitude distributions of total received electric field in z polarisation. Indicated are the maximum and minimum field values, the first and third quartile as well as the mean value.
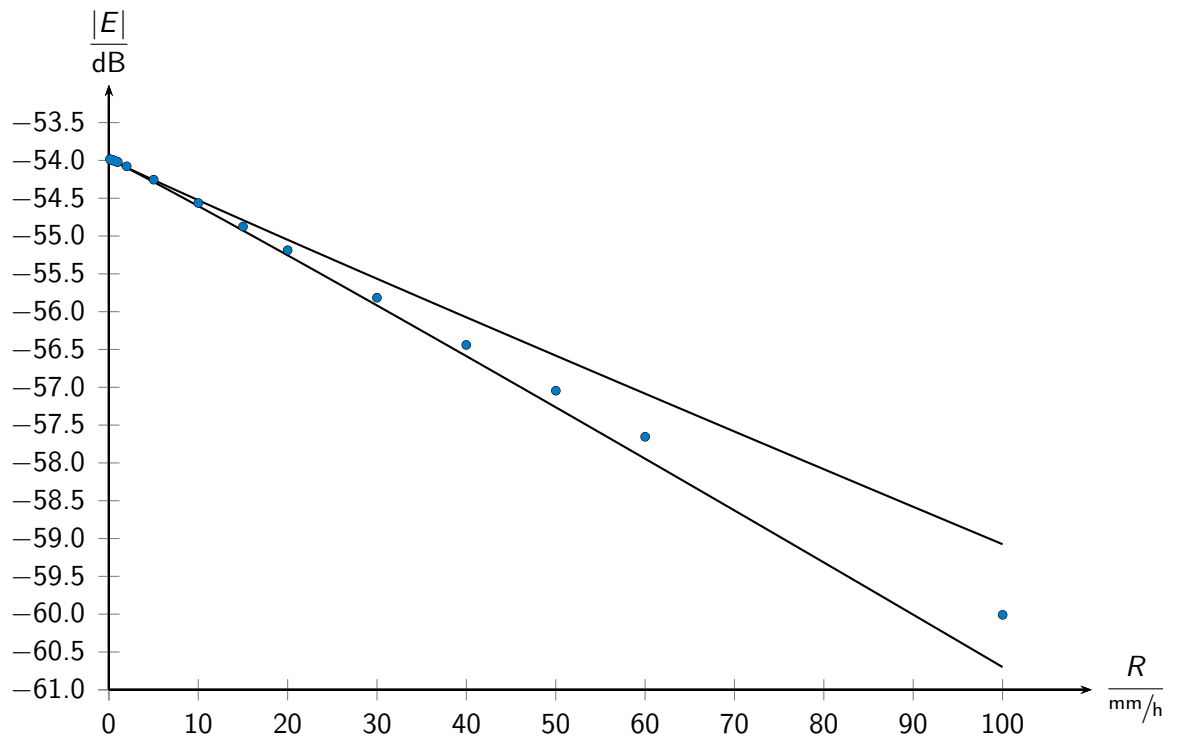
Figure 6.22: Comparison of the simulation results with the ITU Recommendation P.838. The solid lines give limits for either full horizontal or full vertical polarisation of the incident waves.

7 Fokus on Past, Present and Future

7.1 Summary

This chapter draws a conclusion of the discussion presented throughout this documentation. A new approach was developed for the modelling of electromagnetic propagation through rain. While literature gives many approaches to this subject, this work's novelty lies in the composition of synthetic rain fields assembled by individual rain drops. A volume is chosen to enclose the rain field and it is populated with drops sized and distributed according to the statistical properties of the rain field.

This work intends to give a theoretical framework assisting attenuation measurements of waves propagating through rain. Presently, the application of weather monitoring with the use of microwave links is a subject of interest for many groups. To illustrate this, chapter 1 presented a list of experiments currently built or already established worldwide.

This work will be of assistance for projects using point-to-point links of the backhaul network of mobile phone providers. In contrast to the modelling of this application exploiting links of low time resolution, also link paths built with fast recording can be examined using the proposed procedure. For instance the PROCEMA project built a setup with 25 kHz sampling rate that was a model for the simulation whose results are also given in this work.

The approach presented is capable of varying extended properties of rain like the drop size distribution in time or along the link path. Subsequently, the models high flexibility in rain and propagation characteristics enables researchers to image reality more accurately.

The high flexibility offers a new view for related subjects like radiometry or radar. Both subjects can be considered by the model by a simple change of the simulation properties, for instance the direction of scattering for radar. This adjustment in particular is achieved by joining the receiving and the transmission point coordinates.

The model gives a better insight into physical effects taking place when waves propagate through rain. To this end, different rain properties are implemented to analyse effects of their influences.

Two kinds of properties describe rain, first every individual drop shows a specific behaviour. Additionally, its assembly to a rain field is described in a second way.

Major characteristics of individual drops are their shapes, formed by influencing forces. These include inner forces like surface tension as well as environmental influences such as hydrostatic pressure, which causes large drops to flatten at the base.

Therefore, while small drops develop a spherical shape, large drops establish advanced shapes and thus are much harder to deal with. Section 3.1 illustrated and parametrised valid drop shapes intended for the use in the presented model.

An important property of rain drops is the refractive index of water, directly influencing the electromagnetic waves. Two frequency and temperature dependent models based on the refractive index by Ray (1972) and by Liebe, Hufford, and Manabe (1991) were suggested for application.

An individual property of the rain drops is their motion depending on size. While the drops observe a fall velocity increasing with size, wind may also change the position of individual drops.

When observing the rain field as a whole, it is, first of all, characterised by the rain type. Section 3.2 described rain parameters for European countries. Literature proposes the application of one of several distributions of radii expressing the rain type, including the most prominent one, an exponential distribution named after Marshall and Palmer (1948). Linking to the aforementioned dependence, the distribution of radii leads to a distribution of drop velocities. Both different radii as well as the velocities therefore are statistical, producing a noisy received signal.

The signal gathers influences from scattering of the incident rays by rain drops in addition to an extincted propagation of the electromagnetic waves through the rain field. The scattering of the waves by drops is modelled in drop adjusted coordinates.

While the first scattering model was given in a spherical system applying Mie's formulas, other more advanced arrangements can be chosen. Calculations for the simple scattering by spherical shaped objects show similarity for horizontal and vertical polarisation. Applying advanced shapes, for instance spheroids, which are more accurate for larger rain drops, leads to asymmetry in the scattering amplitudes for both polarisations. The adjustment of the polarisation on spherical drops causes a need to transform the incident and scattered coefficients from Cartesian to spherical coordinates and vice versa.

An approach to describe the rain fields as tenuous media, models the extinction of the field amplitude while passing the rain field. Furthermore, applying this method leads to the derivation of an effective refractive index of the whole rain field. For common use, approximations describe the relation of attenuation and rain rate as a power law.

Two additions were given in the chapter dealing with scattering. An often asked question is whether interaction of drops needs to be considered. Therefore, a subsection illustrates models to account for multiple scattering. Finally, the radiative transfer method, applied especially in radiometry, was presented. The presented model is also able to deal with possibly layered paths through rain fields.

The model documented in this work was implemented in MATLAB. The program was built modularly to ensure the possibility to adjust the program to many applications.

The first step performed by the program is the population of a desired volume with rain drops. The drop radii and coordinates are selected in accordance with the chosen radius and coordinate distributions.

The central and most time consuming step performs scattering at all rain drops and accumulates the individual field contributions to derive a single field sample. Until the

stop criteria is met, the program proceeds with an advancement of the drops in space.

The analysis started with a presentation of the amplitude and phase components of the received field for vertical and horizontal polarisation. Examining the figures shows decreasing power with increasing rain rate in the co-polar components. While the contour of this plot is smooth, a clearly noisy signal is visible for the cross-polar part.

The following sections analysed the aforementioned time signals concerning their spectral and statistical behaviours.

In contrast to the co-polar signal, where the direct incidence dominates the received signal, a Doppler shift caused by the falling rain drops is visible in the cross-polar part. Statistical analysis gave a white noise nature in the cross-polar signal while the co-polar part was coloured by the direct incidence.

Analysis of the phases of the signals showed different characteristics. While the phase of the cross-polar signal draws a slowly varying nearly sinusoidal behaviour, the co-polar phase responded with large jumps to a large drop incident into the simulation volume.

A graph showed mean and other statistical measures of the amplitude for several rain rates.

7.2 Conclusion and Outlook

The results presented in this work, clearly give an impression of the noisiness of the received signal. From this result one may conclude the path passed by the field to be of dynamical and statistical nature. Therefore, this concept, in contrast to former ones, manages to imitate reality more authentically. Additional features found in nature may be implemented in the model as will by changing initial parameters or even program functions. Analysis of the effects of these modifications can be computed by the validation algorithms already established and applied in the presented results.

Implementation of new features differs in the effort needed. For instance, altering the scattering process requires a deep insight into the underlying theory, while change of the DSD is realisable by an easy assignment of different parameters describing the distribution.

Similar to many other programs, this algorithm tried to find a balance between computation time and memory consumption. Acceleration was possible, for instance, by the use of look-up tables for the Mie coefficients. In contrast, operations like this increased the memory requirement.

Solving this constraint takes some effort. One approach to further accelerate the program may be performed by a reduction of the simulation volume, while still maintaining accurate statistics. Additionally, speed-up may be achieved by implementation in computer languages offering high multi-core processing and compiled code.

Despite already performed analyses, there is sill the option to examine further effects. For instance, the algorithm allows evaluation of influences such as a rain field passing over the simulation volume or utilising advanced drop shapes.

A Scattering

The following pages derive the equations for scattering at an object consisting of dielectric material. The first section illustrates a general schematic, applied to a spherical object in the second section. The derivations follow Moon and Spencer (1988).

A.1 Schematic to Solve the Helmholtz Equation

The scalar Helmholtz equation using the Laplace operator Δ and the wave number k reads

$$\Delta\Psi + k^2\Psi = 0\,. \tag{A.1.1}$$

In order to solve this equation in a general coordinate system with the coordinates u_i the metric coefficients are defined. A line element

$$(\mathrm{d}s)^2 = \sum_i g_{ii}\,(\mathrm{d}u_i)^2$$

uses the metric coefficients derived from the transformation of the Cartesian coordinates into the general coordinates by

$$g_{ii} = \left(\frac{\partial x}{\partial u_i}\right)^2 + \left(\frac{\partial y}{\partial u_i}\right)^2 + \left(\frac{\partial z}{\partial u_i}\right)^2\,. \tag{A.1.2}$$

In analogy the general volume element

$$\mathrm{d}V = g^{\frac{1}{2}}\prod_i \mathrm{d}u_i$$

applies

$$g^{\frac{1}{2}} = \left(\prod_i g_{ii}\right)^{\frac{1}{2}}\,. \tag{A.1.3}$$

The Nabla operator writen in these general coordinates reads

$$\nabla\Psi = \sum_i \frac{\vec{e}_{ui}}{(g_{ii})^{\frac{1}{2}}}\frac{\partial\Psi}{\partial u_i} \tag{A.1.4}$$

using the unit vector $\vec{e}_{ui}$ for the u_i coordinate. Accordingly, the Laplace operator applied to a function is

$$\Delta\Psi = g^{-\frac{1}{2}} \sum_i \frac{\partial}{\partial u_i} \left[\frac{g^{\frac{1}{2}}}{g_{ii}} \frac{\partial \Psi}{\partial u_i} \right] . \tag{A.1.5}$$

The rotation on an arbitrary vector $\vec{E}$ is expressed as

$$\vec{\nabla} \times \vec{E} = g^{-\frac{1}{2}} \sum_{ijk} \vec{e}_{ui} \left(g_{ii} \right)^{\frac{1}{2}} \varepsilon_{ijk} \frac{\partial}{\partial u_j} \left[g_{kk}^{\frac{1}{2}} E_k \right] \tag{A.1.6}$$

using the Levi-Civita tensor ε_{ijk}.

The Helmholtz equation is separable only in special coordinate systems. In these systems the solution is a product of sub functions U_i, which depend only on a single coordinate u_i

$$\Psi = U_1(u_1)U_2(u_2)U_3(u_3) \tag{A.1.7}$$

with the u_i coordinate specific differential equation

$$\frac{1}{f_i} \frac{\mathrm{d}}{\mathrm{d}u_i} \left(f_i \frac{\mathrm{d}U_i}{\mathrm{d}u_i} \right) + U_i \sum_{j=1}^{3} \alpha_j \Phi_{ij} = 0 . \tag{A.1.8}$$

The variables f_i, Φ_{ij} may be derived from the Stäckel Matrix (see Moon and Spencer (1988)), α is denoted as separation variable.

Propagating waves can be split in two orthogonal modes

$$\vec{M} = (-)\vec{r} \times \nabla\Psi = \nabla \times (\Psi\vec{e}_r) \tag{A.1.9}$$

and

$$\vec{N} = \frac{1}{k} \left(\vec{\nabla} \times \vec{M} \right) = \frac{1}{k} \left[\vec{\nabla} \times (\vec{r} \times \nabla\Psi) \right] . \tag{A.1.10}$$

Combining both modes results in the electric field

$$\vec{E} = \sum_n a_n \vec{N}_n \left(\vec{r} \right) + \frac{z}{j} \sum_n b_n \vec{M}_n \left(\vec{r} \right) . \tag{A.1.11}$$

Were $\vec{N}_n$ denotes the E- or TM-Modes and $\vec{M}_n$ the H- or TE-Modes, respectively.

The expansion coefficients a_n and b_n are derived by using the following considerations: One assumes a plane wave

$$\vec{E}_i = E_0 e^{j\vec{r}\cdot\vec{k}} \vec{e}_x = E_0 e^{jzk} \vec{e}_x = E_0 e^{jrk\cos\theta} \vec{e}_x \tag{A.1.12}$$

propagating in z- and polarized in x-direction with amplitude E_0.

A transformation from Cartesian to general unit vectors can be performed by

$$\vec{e_i} = \sum_j \frac{1}{(g_{ii})^{\frac{1}{2}}} \frac{\partial x_i}{\partial u_j} \vec{e}_{uj} \,. \tag{A.1.13}$$

In general an arbitrary function may be expressed by a series ansatz using the orthogonal functions $g_n(x)$

$$f(x) = \sum_n a_n g_n(x) \,.$$

Here the expansion coefficients are derived by

$$\Rightarrow a_n = \frac{\int\limits_{-1}^{1} f(x) g_n(x) \mathrm{d}x}{\int\limits_{-1}^{1} g_n^2(x) \mathrm{d}x} \,. \tag{A.1.14}$$

For the derivation of the electric field one applies the incident electric field and the two different modes.

Additionally the tangential components of H- and E-Fields at the dielectric medium are continuous at the boundaries, leading to

$$\vec{n}_+ \times \left[\frac{\vec{E}_i}{\vec{H}_i}(k_0 r) + \frac{\vec{E}_s}{\vec{H}_s}(k_0 r) - \frac{\vec{E}_{int}}{\vec{H}_{int}}(kr) \right]\Bigg|_{r \in \partial \Gamma} = 0 \,. \tag{A.1.15}$$

A.2 Solution in Spherical Coordinates

This section applies the schematic derived in the last section to spherical coordinates yielding a solution to the scalar Helmholtz equation as well as E- and H- Field. Detailed calculations, extending the overview given in this section, can be found in section A.2.1 and section A.2.2.

The coordinates from the general solution are substituted by spherical coordinates

$$
\begin{aligned}
u_1 &= r \\
u_2 &= \theta \\
u_3 &= \varphi \,.
\end{aligned}
\tag{A.2.1}
$$

Hence, the Cartesian coordinates are expressed in spherical coordinates by

$$
\begin{aligned}
x &= r \sin \theta \cos \varphi \\
y &= r \sin \theta \sin \varphi \\
z &= r \cos \theta \,.
\end{aligned}
\tag{A.2.2}
$$

Equations (A.1.2) to (A.1.6) yield the metric coefficients

$$
\begin{aligned}
g_{11} &= 1 \\
g_{22} &= r^2 \\
g_{33} &= r^2 \sin^2 \theta \\
g^{\frac{1}{2}} &= r^2 \sin \theta
\end{aligned}
$$

and expressions for Nabla related operations in spherical coordinates:

$$
\nabla \Psi = \frac{\partial \Psi}{\partial r} \vec{e}_r + \frac{1}{r} \frac{\partial \Psi}{\partial \theta} \vec{e}_\theta + \frac{1}{r \sin \theta} \frac{\partial \Psi}{\partial \varphi} \vec{e}_\varphi
\tag{A.2.3}
$$

$$
\Delta \Psi = \frac{1}{r^2} \frac{\partial}{\partial r} \left(r^2 \frac{\partial \Psi}{\partial r} \right) + \frac{1}{r^2 \sin \theta} \frac{\partial}{\partial \theta} \left(\sin \theta \frac{\partial \Psi}{\partial \theta} \right) + \frac{1}{r^2 \sin^2 \theta} \frac{\partial^2 \Psi}{\partial \varphi^2}
\tag{A.2.4}
$$

$$
\begin{aligned}
\nabla \times \vec{E} = \frac{1}{r^2 \sin \theta} &\left\{ \left[\frac{\partial}{\partial \theta} (r \sin \theta E_\varphi) - \frac{\partial}{\partial \varphi} (r E_\theta) \right] \vec{e}_r \right. \\
&+ r \left[\frac{\partial}{\partial \varphi} E_r - \frac{\partial}{\partial r} (r \sin \theta E_\varphi) \right] \vec{e}_\theta \\
&+ \left. r \sin \theta \left[\frac{\partial}{\partial r} (r E_\theta) - \frac{\partial}{\partial \theta} E_r \right] \vec{e}_\varphi \right\}
\end{aligned}
\tag{A.2.5}
$$

In these coordinates the Helmholtz equation is separable

$$
\Psi(r, \theta, \varphi) = R(r) \Theta(\theta) \Phi(\varphi) \,.
\tag{A.2.6}
$$

Equation (A.1.8) of the general schematic yields differential equations for each coordi-

nate:

$$\frac{d}{dr}\left(r^2\frac{dR}{dr}\right) + \left[k^2r^2 - n(n+1)\right]R = 0 \tag{A.2.7}$$

$$\frac{1}{\sin\theta}\frac{d}{d\theta}\left(\sin\theta\frac{d\Theta}{d\theta}\right) + \left[n(n+1) - \frac{m^2}{\sin^2\theta}\right]\Theta = 0 \tag{A.2.8}$$

$$\frac{d^2\Phi}{d\varphi^2} + m^2\Phi = 0 \tag{A.2.9}$$

with the separation variables n and m.

The solutions of these differential equations can be found in literature and are

$$R_n(r) = \left.\begin{matrix} j_n(kr) \\ h_n^{(2)}(kr) \end{matrix}\right\} z_n(kr) \tag{A.2.10}$$

for the radial component with the spherical Bessel functions $j_n(kr)$, with $k = k_0$, for the solution inside the scatterer and spherical Hankel functions $h_n^{(2)}(kr)$, with $k = mk_0$ accounting for the refraction index of the medium, outside the object. In general both solutions are abbreviated with $z_n(kr)$. Using the size parameter $x = kr$ results in the derivation of the radius as $dr = \frac{dx}{k}$.

The angular functions are associated Legendre polynomials for the θ coordinate and sine and cosine for φ:

$$\Theta_{nm}(\theta) = P_n^m(\cos\theta)$$

$$\Phi_m(\varphi) = \begin{matrix} \sin \\ \cos \end{matrix} m\varphi \, .$$

Summarising, the product of the solutions gives

$$\Rightarrow \Psi_{\substack{e \\ o} mn} = \begin{matrix} \cos \\ \sin \end{matrix} m\varphi \, P_n^m(\cos\theta) \, z_n(x) \, . \tag{A.2.11}$$

The associated Legendre polynomials can be derived from the Legendre polynomials (see Abramowitz and Stegun (1964)) by

$$P_l^m(x) = (-1)^m(1-x^2)^{\frac{m}{2}}\frac{d^m}{dx^m}P_l(x)$$

yielding

$$(A.2.61): \quad P_n^1(\cos\theta) = \frac{d\,P_n(\cos\theta)}{d\theta} \tag{A.2.12}$$

for $m = 1$ and $l = n$.

The representation of the TE- and TM-modes is (according to Stratton (2007); van

Bladel (2007)) given by

$$\vec{M}_{e \atop o\, mn} = \frac{m}{\sin\theta}{-\sin \atop \cos}m\varphi\, P_n^m(\cos\theta)z_n(x)\vec{e}_\theta - {\cos \atop \sin}m\varphi\frac{\mathrm{d}\, P_n^m(\cos\theta)}{\mathrm{d}\theta}z_n(x)\vec{e}_\varphi \quad \text{(A.2.13)}$$

and

$$\begin{aligned}
\vec{N}_{e \atop o\, mn} =\ & {\cos \atop \sin}m\varphi n(n+1)\, P_n^m(\cos\theta)\frac{z_n(x)}{x}\vec{e}_r \\
&+ {\cos \atop \sin}m\varphi\frac{\mathrm{d}\, P_n^m(\cos\theta)}{\mathrm{d}\theta}\frac{1}{x}\frac{\mathrm{d}}{\mathrm{d}x}(x\, z_n(x))\vec{e}_\theta \\
&+ m{-\sin \atop \cos}m\varphi\frac{P_n^m(\cos\theta)}{\sin\theta}\frac{1}{x}\frac{\mathrm{d}}{\mathrm{d}x}(x\, z_n(x))\vec{e}_\varphi\,.
\end{aligned} \qquad \text{(A.2.14)}$$

Thus, assuming again the incident plane wave from (A.1.12) expressed in the spherical coordinate system using (A.1.13) and (A.2.2)

$$\text{(A.1.12)}: \qquad \vec{E}_i = E_0 e^{jx\cos\theta}(\sin\theta\cos\varphi\vec{e}_r + \cos\theta\cos\varphi\vec{e}_\theta - \sin\varphi\vec{e}_\varphi)$$

shows that only $\vec{M}_{o1n}$, $\vec{N}_{e1n}$ are possible:

$$\vec{E}_i = \sum_n (A_{e1n}\vec{N}_{e1n} + B_{o1n}\vec{M}_{o1n}) \qquad \text{(A.2.15)}$$

The expansion coefficients can be found by the fraction (see equation (A.1.14) in the general schematic and detailed calculations in the next section)

$$B_{o1n} = \frac{\int\limits_0^{2\pi}\int\limits_0^{\pi} \vec{E}_i \cdot \vec{M}_{o1n}\sin\theta d\theta d\varphi}{\int\limits_0^{2\pi}\int\limits_0^{\pi} |\vec{M}_{o1n}|^2 \sin\theta d\theta d\varphi} \qquad \text{(A.2.16)}$$

$$= E_o(-j)^n\frac{2n+1}{n(n+1)}\,. \qquad \text{(A.2.17)}$$

While A_{e1n} is analogously determined by

$$A_{e1n} = \frac{\int\limits_0^{2\pi}\int\limits_0^{\pi} \vec{E}_i \cdot \vec{N}_{e1n}\sin\theta d\theta d\varphi}{\int\limits_0^{2\pi}\int\limits_0^{\pi} |\vec{N}_{e1n}|^2 \sin\theta d\theta d\varphi} \qquad \text{(A.2.18)}$$

$$= jE_o(-j)^n\frac{2n+1}{n(n+1)}\,. \qquad \text{(A.2.19)}$$

Thus the final expansion of the incident field reads

$$\vec{E}_i = E_0 \sum_n (-j)^n \frac{2n+1}{n(n+1)} \left(\vec{M}_{o1n} - j\vec{N}_{e1n} \right) . \tag{A.2.20}$$

The magnetic field can be derived from the electric field using Maxwell's equation

$$\nabla \times \vec{E} = -j\omega\mu\vec{H}$$

yielding

$$\vec{H}_i = \frac{j}{\omega\mu}\nabla \times \vec{E}_i = \frac{k}{\omega\mu} \sum_{n=1}^{\infty} (-j)^n \frac{2n+1}{n(n+1)} \left(\vec{M}_{e1n} - j\vec{N}_{o1n} \right) \tag{A.2.21}$$

A closer look at the coordinate system reveals the positive normal component $\vec{n}_+$ on a spherical object to be $\vec{e}_r$. Thus internal and scattered field read

$$\vec{E}_{\text{int}} = \sum_{n=1}^{\infty} E_n (c_n \vec{M}_{o1n} + jd_n \vec{N}_{e1n})$$

$$\vec{H}_{\text{int}} = \frac{-k_1}{\omega\mu_1} \sum_{n=1}^{\infty} E_n (d_n \vec{M}_{e1n} - jc_n \vec{N}_{o1n}) \tag{A.2.22}$$

and

$$\vec{E}_s = \sum_{n=1}^{\infty} E_n (-ja_n \vec{N}'_{e1n} - b_n \vec{M}'_{o1n})$$

$$\vec{H}_s = \frac{k}{\omega\mu} \sum_{n=1}^{\infty} E_n (-jb_n \vec{N}'_{o1n} + a_n \vec{M}'_{e1n}) . \tag{A.2.23}$$

The dashed modes depict the use of the spherical Hankel functions as radial solution outside the object in contrast to spherical Bessel functions inside the object and for the incident fields.

Additionally, textbooks denote the abbreviations

$$\pi_n = \frac{P_n^1(\cos\theta)}{\sin\theta}; \ \tau_n = \frac{d\,P_n^1(\cos\theta)}{d\theta} \tag{A.2.24}$$

for the Θ solution. The continuity at the surface yields

$$\begin{aligned}
c_n \, j_n(mx) + b_n \, h_n^{(2)}(x) &= j_n(x) , \\
d_n \, J_n(mx) + a_n \, H_n^{(2)}(x) &= J_n(x) , \\
md_n \, j_n(mx) + a_n \, h_n^{(2)}(x) &= j_n(x) \text{ and} \\
mc_n \, J_n(mx) + b_n \, H_n^{(2)}(x) &= J_n(x) .
\end{aligned} \tag{A.2.25}$$

A Scattering

In these equations the derivation of the spherical Bessel and Hankel functions concerning x is abbreviated by

$$Z_n(x) = \frac{1}{x}\frac{\partial}{\partial x}(x\, z_n(x)) \tag{A.2.26}$$

A convenient solution of (A.2.25) can be found using the matrix notation

$$\begin{bmatrix} H_n^{(2)}(x) & 0 & 0 & J_n(mx) \\ h_n^{(2)}(x) & 0 & 0 & m\, j_n(mx) \\ 0 & h_n^{(2)}(x) & j_n(mx) & 0 \\ 0 & H_n^{(2)}(x) & m\, J_n(mx) & 0 \end{bmatrix} \begin{pmatrix} a_n \\ b_n \\ c_n \\ d_n \end{pmatrix} = \begin{pmatrix} J_n(x) \\ j_n(x) \\ j_n(x) \\ J_n(x) \end{pmatrix} \tag{A.2.27}$$

that can be split in equations for a_n and d_n and analogue for b_n and c_n

$$\begin{bmatrix} H_n^{(2)}(x) & J_n(mx) \\ h_n^{(2)}(x) & m\, j_n(mx) \end{bmatrix} \begin{pmatrix} a_n \\ d_n \end{pmatrix} = \begin{pmatrix} J_n(x) \\ j_n(x) \end{pmatrix} . \tag{A.2.28}$$

Matrix inversion yields the coefficients

$$\begin{pmatrix} a_n \\ d_n \end{pmatrix} = \frac{1}{H_n^{(2)}(x) m\, j_n(mx) - h_n^{(2)}(x)\, J_n(mx)} \begin{bmatrix} m\, j_n(mx) & -J_n(mx) \\ -h_n^{(2)}(x) & H_n^{(2)}(x) \end{bmatrix} \begin{pmatrix} J_n(x) \\ j_n(x) \end{pmatrix} . \tag{A.2.29}$$

For instance the solution for a_n reads

$$a_n = \frac{m\, j_n(mx)\, J_n(x) - J_n(mx)\, j_n(x)}{H_n^{(2)}(x) m\, j_n(mx) - h_n^{(2)}(x)\, J_n(mx)} . \tag{A.2.30}$$

A.2.1 Calculations for Spherical Coordinates

The following pages give detailed calculations for the derivation of the field at a spherical scatterer. They are collected here to avoid destroying the clearness of the total overview in the last section.

The metric coefficients are calculated by

$$
(A.1.2): \quad g_{11} = \left(\frac{\partial x}{\partial r}\right)^2 + \left(\frac{\partial y}{\partial r}\right)^2 + \left(\frac{\partial z}{\partial r}\right)^2
$$

$$
= \sin^2 \theta \cos^2 \varphi + \sin^2 \theta \sin^2 \varphi + \cos^2 \theta = 1
$$

$$
g_{22} = r^2 \cos^2 \theta \cos^2 \varphi + r^2 \cos^2 \theta \sin^2 \varphi + r^2 \sin^2 \theta
$$

$$
= r^2 \cos^2 \theta + r^2 \sin^2 \theta = r^2
$$

$$
g_{33} = r^2 \sin^2 \theta \sin^2 \varphi + r^2 \sin^2 \theta \cos^2 \varphi + 0
$$

$$
= r^2 \sin^2 \theta
$$

$$
(A.1.3): \quad g^{\frac{1}{2}} = (1 \cdot r^2 \cdot r^2 \sin^2 \theta)^{\frac{1}{2}} = r^2 \sin \theta
$$

$$
(A.1.4): \quad \nabla \Psi = \frac{\vec{e}_r}{1} \frac{\partial \Psi}{\partial r} + \frac{\vec{e}_\theta}{r} \frac{\partial \Psi}{\partial \theta} + \frac{\vec{e}_\varphi}{r \sin \theta} \frac{\partial \Psi}{\partial \varphi}
$$

$$
= \frac{\partial \Psi}{\partial r} \vec{e}_r + \frac{1}{r} \frac{\partial \Psi}{\partial \theta} \vec{e}_\theta + \frac{1}{r \sin \theta} \frac{\partial \Psi}{\partial \varphi} \vec{e}_\varphi \qquad (A.2.31)
$$

$$
(A.1.5): \quad \Delta \Psi = \frac{1}{r^2 \sin \theta} \left[\frac{\partial}{\partial r} \left(\frac{r^2 \sin \theta}{1} \frac{\partial \Psi}{\partial r} \right) \right.
$$

$$
+ \frac{\partial}{\partial \theta} \left(\frac{r^2 \sin \theta}{r^2} \frac{\partial \Psi}{\partial \theta} \right)
$$

$$
\left. + \frac{\partial}{\partial \varphi} \left(\frac{r^2 \sin \theta}{r^2 \sin^2 \theta} \frac{\partial \Psi}{\partial \varphi} \right) \right]
$$

$$
= \frac{1}{r^2 \sin \theta} \left[\frac{\partial}{\partial r} \left(r^2 \sin \theta \frac{\partial \Psi}{\partial r} \right) \right.
$$

$$
+ \frac{\partial}{\partial \theta} \left(\sin \theta \frac{\partial \Psi}{\partial \theta} \right)
$$

$$
\left. + \frac{\partial}{\partial \varphi} \left(\frac{1}{\sin \theta} \frac{\partial \Psi}{\partial \varphi} \right) \right]
$$

$$
= \frac{1}{r^2} \frac{\partial}{\partial r} \left(r^2 \frac{\partial \Psi}{\partial r} \right)
$$

$$
+ \frac{1}{r^2 \sin \theta} \frac{\partial}{\partial \theta} \left(\sin \theta \frac{\partial \Psi}{\partial \theta} \right)
$$

$$
+ \frac{1}{r^2 \sin^2 \theta} \frac{\partial^2 \Psi}{\partial \varphi^2} \qquad (A.2.32)
$$

$$(A.1.6): \qquad \nabla \times \vec{E} = \frac{1}{r^2 \sin\theta} \left\{ \vec{e}_r \cdot 1 \left[\frac{\partial}{\partial\theta}(r\sin\theta E_\varphi) - \frac{\partial}{\partial\varphi}(rE_\theta) \right] \right.$$

$$+ \vec{e}_\theta \cdot r \left[\frac{\partial}{\partial\varphi}(1 \cdot E_r) - \frac{\partial}{\partial r}(r\sin\theta E_\varphi) \right]$$

$$\left. + \vec{e}_\varphi \cdot r\sin\theta \left[\frac{\partial}{\partial r}(rE_\theta) - \frac{\partial}{\partial\theta}(1E_r) \right] \right\}$$

$$= \frac{1}{r^2 \sin\theta} \left\{ \left[\frac{\partial}{\partial\theta}(r\sin\theta E_\varphi) - \frac{\partial}{\partial\varphi}(rE_\theta) \right] \vec{e}_r \right.$$

$$+ r \left[\frac{\partial}{\partial\varphi}E_r - \frac{\partial}{\partial r}(r\sin\theta E_\varphi) \right] \vec{e}_\theta$$

$$\left. + r\sin\theta \left[\frac{\partial}{\partial r}(rE_\theta) - \frac{\partial}{\partial\theta}E_r \right] \vec{e}_\varphi \right\} \qquad (A.2.33)$$

Calculation of $\vec{M}_{{e \atop o}\,mn}$, $\vec{N}_{{e \atop o}\,mn}$

$$(A.2.11) :\Rightarrow \Phi_{{e \atop o}\,mn} = {\cos \atop \sin}m\varphi\, P_n^m(\cos\theta)\, z_n(x) \qquad (A.2.34)$$

$$(A.1.9): \vec{M}_{{e \atop o}\,mn} = -\vec{r} \times \nabla\Phi_{{e \atop o}\,mn}$$

$$\overset{(A.1.4)}{=} -r\vec{e}_r \times \left[\frac{\partial}{\partial r}\left({\cos \atop \sin}m\varphi\, P_n^m(\cos\theta)\, z_n(x) \right) \vec{e}_r \right.$$

$$+ \frac{1}{r}\frac{\partial}{\partial\theta}\left({\cos \atop \sin}m\varphi\, P(\cos\theta)\, z_n(x) \right) \vec{e}_\theta$$

$$\left. + \frac{1}{r\sin\theta}\frac{\partial}{\partial\varphi}\left({\cos \atop \sin}m\varphi\, P_n^m(\cos\theta)\, z_n(x) \right) \vec{e}_\varphi \right]$$

$$= -r\vec{e}_r \times \left({\cos \atop \sin}m\varphi\, P_n^m(\cos\theta)\frac{\mathrm{d}\,z_n(x)}{\mathrm{d}r}\vec{e}_r \right.$$

$$+ \frac{1}{r}{\cos \atop \sin}m\varphi\frac{\mathrm{d}\,P_n^m(\cos\theta)}{\mathrm{d}\theta}\, z_n(x)\vec{e}_\theta$$

$$\left. + \frac{m}{\sin\theta}{-\sin \atop \cos}m\varphi\, P_n^m(\cos\theta)\, z_n(x)\vec{e}_\varphi \right)$$

$$\overset{(A.2.55)}{=} \frac{m}{\sin\theta}{-\sin \atop \cos}m\varphi\, P_n^m(\cos\theta)\, z_n(x)\vec{e}_\theta$$

$$- {\cos \atop \sin}m\varphi\frac{\mathrm{d}\,P_n^m(\cos\theta)}{\mathrm{d}\theta}\, z_n(x)\vec{e}_\varphi \qquad (A.2.35)$$

(A.1.10) partial component (using (A.2.5))

$$kN_r = \left(\nabla \times \vec{M}\right) \cdot \vec{e}_r$$

$$= \frac{1}{r^2 \sin\theta} \frac{\partial}{\partial\theta} \left(-r\sin\theta \frac{\cos}{\sin} m\varphi \frac{\mathrm{d}\,P_n^m(\cos\theta)}{\mathrm{d}\theta} z_n(x)\right)$$

$$- \frac{\partial}{\partial\varphi} \left(r \frac{m}{\sin\theta} \frac{-\sin}{\cos} m\varphi\, P_n^m(\cos\theta)\, z_n(x)\right)$$

$$= \frac{r\,z_n(x)}{r^2 \sin\theta} \left[-\frac{\cos}{\sin} m\varphi \frac{\mathrm{d}}{\mathrm{d}\theta} \left(\sin\theta \frac{\mathrm{d}\,P_n^m(\cos\theta)}{\mathrm{d}\theta}\right)\right.$$

$$\left. - \frac{m\,P_n^m(\cos\theta)}{\sin\theta} \frac{\mathrm{d}}{\mathrm{d}\varphi}\left(\frac{-\sin}{\cos} m\varphi\right)\right]$$

$$= \frac{z_n(x)}{r\sin\theta} \left[-\frac{\cos}{\sin} m\varphi \frac{\mathrm{d}}{\mathrm{d}\theta}\left(\sin\theta \frac{\mathrm{d}\,P_n^m(\cos\theta)}{\mathrm{d}\theta}\right) + \frac{\cos}{\sin} m\varphi \frac{m^2}{\sin\theta} P_n^m(\cos\theta)\right]$$

$$= \frac{z_n(x)}{r\sin\theta} \frac{\cos}{\sin} m\varphi \left[\frac{m^2}{\sin\theta} P_n^m(\cos\theta) - \frac{\mathrm{d}}{\mathrm{d}\theta}\left(\sin\theta \frac{\mathrm{d}\,P_n^m(\cos\theta)}{\mathrm{d}\theta}\right)\right]$$

$$\overset{(A.2.59)}{\underset{\downarrow}{=}} \frac{z_n(x)}{r\sin\theta} \frac{\cos}{\sin} m\varphi\, n(n+1)\, P_n^m(\cos\theta) \sin\theta$$

$$= \frac{\cos}{\sin} m\varphi \frac{z_n(x)}{r} n(n+1)\, P_n^m(\cos\theta)$$

$$kN_\theta = \frac{1}{r^2 \sin\theta} r \left[-\frac{\partial}{\partial r}\left(r\sin\theta M_\varphi\right)\right]$$

$$= -\frac{1}{r} \frac{\partial}{\partial r}\left(r M_\varphi\right)$$

$$= \frac{1}{r} \frac{\partial}{\partial r}\left(r \frac{\cos}{\sin} m\varphi \frac{\mathrm{d}\,P_n^m(\cos\theta)}{\mathrm{d}\theta} z_n(x)\right)$$

$$= \frac{\cos}{\sin} m\varphi \frac{\mathrm{d}\,P_n^m(\cos\theta)}{\mathrm{d}\theta} \frac{1}{r} \frac{\mathrm{d}}{\mathrm{d}r}\left(r\, z_n(x)\right)$$

$$kN_\varphi = \frac{1}{r^2 \sin\theta} r\sin\theta \frac{\partial}{\partial r}\left(r M_\theta\right)$$

$$= \frac{1}{r} \frac{\partial}{\partial r}\left(r \frac{m}{\sin\theta} \frac{-\sin}{\cos} m\varphi\, P_n^m(\cos\theta)\, z_n(x)\right)$$

$$= \frac{m}{r\sin\theta} \frac{-\sin}{\cos} m\varphi\, P_n^m(\cos\theta) \frac{\mathrm{d}}{\mathrm{d}r}\left(r\, z_n(x)\right)$$

$$\Rightarrow \vec{N}_{\substack{e\\o\,mn}} = \frac{z_n(x)}{x}\frac{\cos}{\sin}m\varphi\,n(n+1)\,P_n^m(\cos\theta)\vec{e}_r$$

$$+\frac{\cos}{\sin}m\varphi\frac{\mathrm{d}\,P_n^m(\cos\theta)}{\mathrm{d}\theta}\frac{1}{x}\frac{\mathrm{d}}{\mathrm{d}r}(r\,z_n(x))\vec{e}_\theta$$

$$+\frac{m}{\sin\theta}\frac{-\sin}{\cos}m\varphi\,P_n^m(\cos\theta)\frac{1}{x}\frac{\mathrm{d}}{\mathrm{d}r}(r\,z_n(x))\vec{e}_\varphi$$

$$=\frac{\cos}{\sin}m\varphi\,n(n+1)\,P_n^m(\cos\theta)\frac{z_n(x)}{x}\vec{e}_r$$

$$+\frac{\cos}{\sin}m\varphi\frac{\mathrm{d}\,P_n^m(\cos\theta)}{\mathrm{d}\theta}\frac{1}{x}\frac{\mathrm{d}}{\mathrm{d}x}(x\,z_n(x))\vec{e}_\theta$$

$$+m\frac{-\sin}{\cos}m\varphi\frac{P_n^m(\cos\theta)}{\sin\theta}\frac{1}{x}\frac{\mathrm{d}}{\mathrm{d}x}(x\,z_n(x))\vec{e}_\varphi \qquad (A.2.36)$$

Derivation of Incident Waves

Plane waves: (A.1.12) and (A.1.13)

$$\vec{E}_i = E_0 e^{-\mathrm{j}x\cos\theta}\vec{e}_x$$

$$\vec{e}_x = \frac{\partial x}{\partial r}\vec{e}_r + \frac{\partial x}{\partial\theta}\vec{e}_\theta + \frac{\partial x}{\partial\varphi}\vec{e}_\varphi$$

$$=\sin\theta\cos\varphi\,\vec{e}_r + \cos\theta\cos\varphi\,\vec{e}_\theta - \sin\varphi\,\vec{e}_\varphi$$

$$\Rightarrow \vec{E}_i = E_0 e^{-\mathrm{j}x\cos\theta}(\sin\theta\cos\varphi\,\vec{e}_r + \cos\theta\cos\varphi\,\vec{e}_\theta - \sin\varphi\,\vec{e}_\varphi) \qquad (A.2.37)$$

Comparison of $\vec{E}_i$ using $\vec{M}_{\substack{e\\o\,mn}}$, $\vec{N}_{\substack{e\\o\,mn}}$ ((A.2.13), (A.2.14))

$$\Rightarrow \quad \text{just}\cos\varphi,\ \sin\varphi \Rightarrow m=1$$

$$S_1\cos\varphi\vec{e}_\theta + S_2\sin\varphi\vec{e}_\varphi \Rightarrow \text{just}\ \begin{matrix}\vec{M}_{o1n}\\\vec{N}_{e1n}\end{matrix}\ \text{using}\ \mathrm{j}_n(x)$$

$$(A.1.11)\Rightarrow \quad \vec{E}_i = \sum_n\left(A_{e1n}\vec{N}_{e1n} + B_{o1n}\vec{M}_{o1n}\right)$$

$$(A.2.16)\quad B_{o1n} = \frac{\int\limits_0^{2\pi}\int\limits_0^\pi \vec{E}_i\vec{M}_{o1n}\sin\theta\mathrm{d}\theta\mathrm{d}\varphi}{\int\limits_0^{2\pi}\int\limits_0^\pi\left|\vec{M}_{o1n}\right|^2\sin\theta\mathrm{d}\theta\mathrm{d}\varphi} \qquad (A.2.38)$$

Denominator

$$(A.2.13):\ \left|\vec{M}_{o1n}\right|^2 = \frac{\cos^2\varphi}{\sin^2\theta}(P_n^1(\cos\theta))^2\,\mathrm{j}_n^2(x) + \sin^2\varphi\left(\frac{\mathrm{d}\,P_n^1(\cos\theta)}{\mathrm{d}\theta}\right)^2\mathrm{j}_n^2(x) \quad (A.2.39)$$

Integration over φ & (A.2.57)

$$\int_0^{2\pi} \left| \vec{M}_{o1n} \right|^2 \mathrm{d}\varphi = \pi \, \mathrm{j}_n^2(x) \left\{ \left(\frac{\mathrm{P}_n^1(\cos\theta)}{\sin\theta} \right)^2 + \left(\frac{\mathrm{d}\,\mathrm{P}_n^1(\cos\theta)}{\mathrm{d}\theta} \right)^2 \right\}$$

using (A.2.58) & m = 1

$$= \pi \, \mathrm{j}_n^2(x) \left\{ n(n+1)(\mathrm{P}_n^1(\cos\theta))^2 \right.$$
$$\left. + \frac{\mathrm{d}}{\mathrm{d}\theta} \left(\sin\theta \frac{\mathrm{d}\,\mathrm{P}_n^1(cos\theta)}{\mathrm{d}\theta} \, \mathrm{P}_n^1(\cos\theta) \right) \frac{1}{\sin\theta} \right\}$$

Integration over θ

$$\int_0^{2\pi}\int_0^{\pi} \left| \vec{M}_{o1n} \right|^2 \sin\theta \mathrm{d}\theta \mathrm{d}\varphi = \pi \, \mathrm{j}_n^2(x) n(n+1) \int_0^{\pi} (\mathrm{P}_n^1(\cos\theta))^2 \sin\theta \mathrm{d}\theta$$

$$+ \pi \, \mathrm{j}_n^2(x) \int_0^{\pi} \frac{\mathrm{d}}{\mathrm{d}\theta} \left(\sin\theta \frac{\mathrm{d}\,\mathrm{P}_n^1(cos\theta)}{\mathrm{d}\theta} \, \mathrm{P}_n^1(\cos\theta) \right) \mathrm{d}\theta$$

$$\overset{\underset{(A.2.59)}{\downarrow}}{=} \pi \, \mathrm{j}_n^2(x) \frac{2n^2(n+1)^2}{2n+1}$$

$$+ \pi \, \mathrm{j}_n^2(x) \underbrace{\left[\sin\theta \frac{\mathrm{d}\,\mathrm{P}_n^2(\cos\theta)}{\mathrm{d}\theta} \, \mathrm{P}_n^2(\cos\theta) \right]_0^{\pi}}_{\sin 0 = \sin\pi = 0}$$

$$= \pi \, \mathrm{j}_n^2(x) \frac{2n^2(n+1)^2}{2n+1} \qquad\qquad (A.2.40)$$

Numerator

$$\vec{E}_{\mathrm{i}} \cdot \vec{M}_{o1n} = E_0 e^{-\mathrm{j}x\cos\theta}(\sin\theta\cos\varphi\vec{e}_r + \cos\theta\cos\varphi\vec{e}_\theta - \sin\varphi\vec{e}_\varphi)$$
$$\cdot \left(\frac{\cos\varphi}{\sin\theta} \mathrm{P}_n^1(\cos\theta)\, \mathrm{j}_n(x)\vec{e}_\theta - \sin\varphi \frac{\mathrm{d}\,\mathrm{P}_n^1(\cos\theta)}{\mathrm{d}\theta} \mathrm{j}_n(x)\vec{e}_\varphi \right)$$
$$= E_o e^{-\mathrm{j}x\cos\theta}\,\mathrm{j}_n(x) \left(\frac{\cos\theta}{\sin\theta}\cos^2\varphi\,\mathrm{P}_n^1(\cos\theta) + \sin^2\varphi \frac{\mathrm{d}\,\mathrm{P}_n^1(\cos\theta)}{\mathrm{d}\theta} \right)$$

Integration over φ & (A.2.57)

$$\int_0^{2\pi} \vec{E}_i \cdot \vec{M}_{o1n}\mathrm{d}\varphi = \pi E_0 e^{-\mathrm{j}x\cos\theta}\,\mathrm{j}_n(x) \left(\frac{\cos\theta}{\sin\theta}\mathrm{P}_n^1(\cos\theta) + \frac{\mathrm{d}\,\mathrm{P}_n^1(\cos\theta)}{\mathrm{d}\theta} \right) \quad (A.2.41)$$

Integration over θ

$$\int_0^\pi \int_0^{2\pi} \vec{E_i} \cdot \vec{M}_{o1n} \mathrm{d}\varphi \sin\theta \mathrm{d}\theta = \int_0^\pi \pi E_0 e^{-\mathrm{j}x\cos\theta} \, \mathrm{j}_n(x) \left(\cos\theta \, \mathrm{P}_n^1(\cos\theta) \right.$$

$$\left. + \sin\theta \frac{\mathrm{d}\,\mathrm{P}_n^1(\cos\theta)}{\mathrm{d}\theta} \right) \mathrm{d}\theta$$

$$\stackrel{(A.2.60)}{=} \pi \int_0^\pi E_0 e^{-\mathrm{j}x\cos\theta} \, \mathrm{j}_n(x) \frac{\mathrm{d}}{\mathrm{d}\theta} \left(\sin\theta \, \mathrm{P}_n^1(\cos\theta) \right) \mathrm{d}\theta$$

$$\stackrel{(A.2.12)}{=} \pi E_0 \, \mathrm{j}_n(x) \int_0^\pi e^{-\mathrm{j}x\cos\theta} \frac{\mathrm{d}}{\mathrm{d}\theta} \left(\sin\theta \frac{\mathrm{d}\,\mathrm{P}_n(\cos\theta)}{\mathrm{d}\theta} \right) \mathrm{d}\theta$$

$$\stackrel{(A.2.8)}{\underset{m=0}{=}} \pi E_0 \, \mathrm{j}_n(x)(-1)n(n+1)$$

$$\cdot \int_0^\pi e^{-\mathrm{j}x\cos\theta} \, \mathrm{P}_n(\cos\theta) \sin\theta \mathrm{d}\theta$$

$$\stackrel{(A.2.62)}{=} \pi E_0 n(n+1) \, \mathrm{j}_n^2(x) 2(-\mathrm{j})^n \tag{A.2.42}$$

(A.2.40), (A.2.42)

$$\Rightarrow B_{o1n} = \frac{\text{Numerator}}{\text{Denominator}} = \frac{\pi E_0 z_n^2(x) 2n(n+1)(-\mathrm{j})^n}{\pi z_n^2(x) \frac{2n^2(n+1)^2}{2n+1}}$$

$$= E_0(-\mathrm{j})^n \frac{2n+1}{n(n+1)} \tag{A.2.43}$$

Derivation of A_{e1n}

$$\text{(A.2.63)} \quad A_{e1n} = \frac{\int_0^{2\pi}\int_0^\pi \vec{E_i}\vec{N}_{e1n}\sin\theta \mathrm{d}\theta \mathrm{d}\varphi}{\int_0^{2\pi}\int_0^\pi \left|\vec{N}_{e1n}\right|^2 \sin\theta \mathrm{d}\theta \mathrm{d}\varphi} \tag{A.2.44}$$

$$\text{Substitution } J_n(x) = \frac{\mathrm{d}}{\mathrm{d}x}(x\,\mathrm{j}_n(x)) \tag{A.2.45}$$

Denominator

$$\left|\vec{N}_{e1n}\right|^2 = \cos^2\varphi\, n^2(n+1)^2 (P_n^1(\cos\theta))^2 \frac{j_n^2(x)}{x^2}$$

$$+ \cos^2\varphi \left(\frac{d\, P_n^1(\cos\theta)}{d\theta}\right)^2 \frac{J_n^2(x)}{x^2}$$

$$+ \sin^2\varphi \left(\frac{P_n^1(\cos\theta)}{\sin\theta}\right)^2 \frac{J_n^2(x)}{x^2}$$

Integration over φ using (A.2.57)

$$\int\limits_0^{2\pi} \left|\vec{N}_{e1n}\right|^2 d\varphi = \frac{\pi}{x^2}\left\{ n^2(n+1)^2 (P_n^1(\cos\theta))^2\, j_n^2(x) \right.$$

$$\left. + J_n^2(x)\left[\left(\frac{d\, P_n^1(\cos\theta)}{d\theta}\right)^2 + \left(\frac{P_n^1(\cos\theta)}{\sin\theta}\right)^2\right]\right\}$$

Integration over θ & (A.2.58) using $m = 1$

$$\int\limits_0^\pi \int\limits_0^{2\pi} \left|\vec{N}_{e1n}\right|^2 d\varphi\, \sin\theta d\theta = \frac{\pi}{x^2}\int\limits_0^\pi \left\{ n^2(n+1)^2 (P_n^1(\cos\theta))^2\, j_n^2(x)\sin\theta \right.$$

$$+ n(n+1)\, J_n^2(x)(P_n^1(\cos\theta))^2 \sin\theta$$

$$\left. + J_n^2(x)\frac{d}{d\theta}\underbrace{\left(\sin\theta\frac{d\, P_n^1(\cos\theta)}{d\theta}\, P_n^1(\cos\theta)\right)}_{\int = 0}\right\}d\theta$$

$$= \frac{\pi}{x^2}n(n+1)\left[n(n+1)\, j_n^2(x)\right.$$

$$\left. + J_n^2(x)\right]\int\limits_0^\pi (P_n^1(\cos\theta))^2 \sin\theta d\theta$$

(A.2.59) :
$$= \frac{2\pi n^2(n+1)^2}{x^2(2n+1)}\left[n(n+1)\, j_n^2(x) + J_n^2(x)\right] \qquad \text{(A.2.46)}$$

Numerator

$$\vec{E}_i \vec{N}_{e1n} = E_0 e^{-jx\cos\theta}\left(\sin\theta\cos^2\varphi\, n(n+1)\,P_n^1(\cos\theta)\frac{j_n(x)}{x}\right.$$

$$\left. + \cos\theta\cos^2\varphi\frac{d\,P_n^1(\cos\theta)}{d\theta}\frac{J_n(x)}{x} + \sin^2\varphi\frac{P_n^1(\cos\theta)}{\sin\theta}\frac{J_n(x)}{x}\right)$$

Integration over φ using (A.2.57)

$$\int\limits_0^{2\pi}\vec{E}_i\vec{N}_{e1n}\mathrm{d}\varphi = \frac{\pi E_0}{x}e^{-jx\cos\theta}\left[\sin\theta\, n(n+1)\,P_n^1(\cos\theta)\,j_n(x)\right.$$

$$\left. + J_n(x)\left(\cos\theta\frac{d\,P_n^1(\cos\theta)}{d\theta} + \frac{P_n^1(\cos\theta)}{\sin\theta}\right)\right]$$

Integration over θ

$$\int\limits_0^\pi\int\limits_0^{2\pi}\vec{E}_i\vec{N}_{e1n}\mathrm{d}\varphi\sin\theta\mathrm{d}\theta = \frac{\pi E_0}{x}\int\limits_0^\pi\left[e^{-jx\cos\theta}\sin^2\theta\, n(n+1)\,P_n^1(\cos\theta)\,j_n(x)\right.$$

$$+ J_n(x)e^{-jx\cos\theta}\left(\cos\theta\frac{d\,P_n^1(\cos\theta)}{d\theta}\right.$$

$$\left.\left. + \frac{P_n^1(\cos\theta)}{\sin\theta}\right)\sin\theta\right]\mathrm{d}\theta$$

$$\text{(A.2.63), (A.2.65)}\qquad = \frac{\pi E_0}{x}\left[\frac{n(n+1)\,j_n(x)}{jx}\right.$$

$$\cdot\int\limits_0^\pi\left(\frac{\mathrm{d}}{\mathrm{d}\theta}e^{-jx\cos\theta}\right)(\sin\theta\,P_n^1(\cos\theta))\mathrm{d}\theta$$

$$\left. + J_n(x)\frac{J_n(x)2n(n+1)}{j^n jx}\right]$$

$$\text{part. Int. (A.2.12)}\qquad = \frac{\pi E_0}{x^2}j\left[n(n+1)\,j_n(x)\right.$$

$$\cdot\left(\underbrace{\int\limits_0^\pi\frac{\mathrm{d}}{\mathrm{d}\theta}\left(e^{-jx\cos\theta}\sin\theta\frac{d\,P_n^1(\cos\theta)}{d\theta}\right)\mathrm{d}\theta}_{\int = 0}\right.$$

$$\left. + \int\limits_0^\pi e^{-jx\cos\theta}\frac{\mathrm{d}}{\mathrm{d}\theta}\left(\sin\theta\frac{d\,P_n^1(\cos\theta)}{d\theta}\right)\mathrm{d}\theta\right)$$

$$\left. + J_n^2(x)2n(n+1)(-j)^n\right]$$

$$(A.2.8) \ m = 1 \& (A.2.62) \quad = j\frac{\pi E_0}{x^2} \left[2n^2(n+1)^2 \, j_n^2(x)(-j)^n \right.$$

$$\left. + 2n(n+1) \, J_n^2(x)(-j)^n \right]$$

$$= \frac{j\pi E_0 2n(n+1)(-j)^n}{x^2} \left[n(n+1) \, j_n^2(x) + J_n^2(x) \right]$$

$$(A.2.47)$$

also (A.2.46), (A.2.47)

$$A_{e1n} = j\frac{\cancel{\pi E_0 2n(n+1)} - (j)^n [n(n+1) \cancel{j_n^2(x) + J_n^2(x)}] \cancel{x^2}(2n+1)}{\cancel{x^2} 2\pi \cancel{n^2(n+1)^2} [n(n+1) \cancel{j_n^2(x) + J_n^2(x)}]}$$

$$= jE_0(-j)^n \frac{2n+1}{n(n+1)} \tag{A.2.48}$$

(A.2.16) using (A.2.20)-(A.2.24)
E-Field

$$\vec{e}_r \times \left[\vec{E}_i(x) + \vec{E}_s(x) - \vec{E}_{int}(mx) \right] \big|_{x=\frac{a}{k_0}} = 0 \tag{A.2.49}$$

$$\Rightarrow E_{int,\varphi} = E_{i,\varphi} + E_{s,\varphi}$$
$$E_{int,\theta} = E_{i,\theta} + E_{s,\theta} \tag{A.2.50}$$

$$\varphi : \sum_{n=1}^{\infty} E_n(c_n M_{o1n,\varphi} + j d_n N_{e1n,\varphi})$$

$$= E_0 \sum_{n=1}^{\infty} (-j)^n \frac{2n+1}{n(n+1)} (M_{o1n,\varphi} + j N_{e1n,\varphi})$$

$$+ \sum_{n=1}^{\infty} E_n(-j a_n N'_{e1n,\varphi} - b_n M'_{o1n,\varphi}) \tag{A.2.51}$$

using $E_n = E_o(-j)^n \dfrac{2n+1}{n(n+1)}$

$$c_n(-\sin\varphi)\tau_n \, j(mx) + j d_n(-\sin\varphi)\pi_n \, J(mx)$$

$$= (-\sin\varphi)\tau_n \, j(x) + j(-\sin\varphi)\pi_n \, J(x)$$

$$- j a_n(-\sin\varphi)\pi_n \, H_n^{(2)}(x) - b_n(-\sin\varphi)\tau_n \, h_n^{(2)}(x) \tag{A.2.52}$$

Terms with τ_n

$$c_n \tau_n \, \mathrm{j}_n(mx) = \tau_n \, \mathrm{j}_n(x) - b_n \tau_n \, \mathrm{h}_n^{(2)}(x)$$
$$\rightarrow c_n \, \mathrm{j}_n(mx) = \mathrm{j}_n(x) - b_n \, \mathrm{h}_n^{(2)}(x)$$

Terms with π_n

$$\mathrm{j}d_n \pi_n \, \mathrm{J}_n(mx) = \mathrm{j}\pi_n \, \mathrm{J}(x) - \mathrm{j}a_n \pi_n \, \mathrm{H}^{(2)}(x)$$
$$d_n \, \mathrm{J}_n(mx) = \mathrm{J}(x) - a_n \, \mathrm{H}^{(2)}(x)$$

(A.2.53)

Same result for θ-part

H-Field: φ

$$-\frac{mk}{\omega} \sum_{n=1}^{\infty} E_n(d_n M_{e1n,\varphi} - \mathrm{j}c_n N_{o1n,\varphi})$$
$$= -\frac{k}{\omega} E_0 \sum_{n=1}^{\infty} \mathrm{j}^n \frac{2n+1}{n(n+1)}(M_{e1n,\varphi} - \mathrm{j}N_{o1n,\varphi})$$
$$-\frac{k}{\omega} \sum_{n=1}^{\infty} E_n(\mathrm{j}b_n N'_{o1n,\varphi} + a_n M'_{e1n,\varphi})$$

$$m(d_n(-\cos\varphi)\tau_n \, \mathrm{j}(mx) - \mathrm{j}c_n(-\cos\varphi)\pi_n \, \mathrm{J}(mx)$$
$$= (-\cos\varphi)\tau_n \, \mathrm{j}(x) - \mathrm{j}\cos\varphi\pi_n \, \mathrm{J}(x)$$
$$+ \mathrm{j}b_n \cos\varphi\pi_n \, \mathrm{H}_n^{(2)}(x) - a_n(-\cos\varphi)\tau_n \, \mathrm{h}_n^{(2)}(x)$$

$$\tau_n : md_n \, \mathrm{j}_n(mx) = \mathrm{j}_n(x) - a_n \, \mathrm{h}_n^{(2)}(x)$$
$$\pi_n : mc_n \, \mathrm{J}_n(mx) = \mathrm{J}_n(x) - b_n \, \mathrm{H}_n^{(2)}(x)$$

(A.2.54)

A.2.2 Auxiliary Calculations for Spherical Coordinates

referring to (A.1.9)

$$r\vec{e}_r \times (a_1\vec{e}_r + a_2\vec{e}_\theta + a_3\vec{e}_\varphi) = r(a_2\vec{e}_\varphi - a_3\vec{e}_\theta) = -r(a_3\vec{e}_\theta - a_2\vec{e}_\varphi) \qquad \text{(A.2.55)}$$

Auxiliary calculation to (A.1.10)
Differential Equation of Θ (A.2.8)

$$\frac{1}{\sin\theta}\frac{\mathrm{d}}{\mathrm{d}\theta}\left(\sin\theta\frac{\mathrm{d}\Theta}{\mathrm{d}\theta}\right) + \left[n(n+1) - \frac{m^2}{\sin^2\theta}\right]\Theta = 0$$

$$\Rightarrow \frac{m^2}{\sin^2\theta}\Theta - \frac{1}{\sin\theta}\frac{\mathrm{d}}{\mathrm{d}\theta}\left(\sin\theta\frac{\mathrm{d}\Theta}{\mathrm{d}\theta}\right) = n(n+1)\Theta \qquad \text{(A.2.56)}$$

Auxiliary calculation to (A.2.16) (Bronstein and Semendjajew 2008):

$$\int\limits_0^{2\pi}\cos^2\varphi\mathrm{d}\varphi = \int\limits_0^{2\pi}\sin^2\varphi\mathrm{d}\varphi = \pi \qquad \text{(A.2.57)}$$

From (A.2.8)$\cdot\Theta/\sin\theta$

$$\frac{\mathrm{d}}{\mathrm{d}\theta}\left(\sin\theta\frac{\mathrm{d}\Theta}{\mathrm{d}\theta}\right)\Theta + \left[n(n+1) - \frac{m^2}{\sin^2\theta}\right]\Theta^2\sin\theta = 0$$

Chain rule

$$\frac{\mathrm{d}}{\mathrm{d}\theta}\left(\sin\theta\frac{\mathrm{d}\Theta}{\mathrm{d}\theta}\Theta\right) - \sin\theta\left(\frac{\mathrm{d}\Theta}{\mathrm{d}\theta}\right)^2 + \left[n(n+1) - \frac{m^2}{\sin^2\theta}\right]\Theta^2\sin\theta = 0$$

sort

$$\left[\left(\frac{\mathrm{d}\Theta}{\mathrm{d}\theta}\right)^2 + m^2\left(\frac{\Theta}{\sin\theta}\right)^2\right]\sin\theta = n(n+1)\Theta^2\sin\theta + \frac{\mathrm{d}}{\mathrm{d}\theta}\left(\sin\theta\frac{\mathrm{d}\Theta}{\mathrm{d}\theta}\Theta\right) \quad \text{(A.2.58)}$$

(Abramowitz and Stegun 1964) Calculation of

$$\int\limits_0^{\pi}(P_n^1(\cos\theta))^2\sin\theta\mathrm{d}\theta$$

using

$$\text{Substitution } \mu = \cos\theta \Rightarrow d\mu = -\sin\theta d\theta$$
$$\text{Limits } \cos(0) = 1; \; \cos(\pi) = 1$$

$$\int_0^\pi (P_n^1(\cos\theta))^2 \sin\theta d\theta = \int_{-1}^1 (P_n^1(\mu))^2 d\mu = \frac{2(n+1)!}{(2n+1)(n-1)!}$$
$$= \frac{2n(n+1)}{2n+1} \tag{A.2.59}$$

Auxiliary calculation to (A.2.16):

$$\frac{d}{d\theta}(\sin\theta \, P_n^1(\cos\theta)) = \cos\theta \, P_n^1(\cos\theta) + \sin\theta \frac{d\,P_n^1(\cos\theta)}{d\theta} \tag{A.2.60}$$

(Abramowitz and Stegun 1964) (8.6.6)

$$P_l^m(x) = (-1)^m (1-x^2)^{\frac{m}{2}} \frac{d^m}{dx^m} P_l(x)$$

with $m = 1$, $l = n$, $x = \cos\theta$

$$P_n^1(\cos\theta) = -(1 - \cos^2\theta)^{\frac{1}{2}} \frac{d\,P_n(\cos\theta)}{d\cos\theta}$$

from (A.2.59): $d\cos\theta = -\sin\theta d\theta$

$$= -\frac{\sin\theta}{-\sin\theta}\frac{d\,P_n(\cos\theta)}{d\theta} = \frac{d\,P_n(\cos\theta)}{d\theta} \tag{A.2.61}$$

(Abramowitz and Stegun 1964)
Gegenbauer's Generalisation

$$j_n(x) = \frac{j^n}{2}\int_0^\pi e^{-jx\cos\theta}\,P_n(\cos\theta)\sin\theta d\theta \tag{A.2.62}$$

$$\frac{d}{d\theta}e^{-jx\cos\theta} = e^{-jx\cos\theta}jx\sin\theta$$
$$\Rightarrow e^{-jx\cos\theta}\sin\theta = \frac{1}{jx}\frac{d}{d\theta}e^{-jx\cos\theta} \tag{A.2.63}$$

$$\cos\theta \frac{d}{d\theta}(\sin\theta\,P_n^1) = \cos\theta(\cos\theta\,P_n^1 + \sin\theta \frac{d\,P_n^1}{d\theta}) = \cos^2\theta\,P_n^1 + \cos\theta\sin\theta\frac{d\,P_n^1}{d\theta}$$

$$= -\sin^2\theta\,P_n^1 + P_n^1 + \cos\theta\sin\theta\frac{d\,P_n^1}{d\theta}$$

$$= -\sin^2\theta\,P_n^1 + \sin\theta\left(\frac{P_n^1}{\sin\theta} + \cos\theta\frac{d\,P_n^1}{d\theta}\right) \qquad (A.2.64)$$

$$(A.2.62): \qquad j_n(x) = \frac{j^n}{2}\int_0^\pi e^{-jx\cos\theta}\,P_n(\cos\theta)\sin\theta d\theta \quad /\cdot x/\frac{d}{dx}$$

$$\frac{d}{dx}(x\,j_n(x)) = \frac{j^n}{2}\int_0^\pi \frac{d}{dx}\left(e^{-jx\cos\theta}x\,P_n(\cos\theta)\sin\theta\right)d\theta$$

$$= \frac{j^n}{2}\int_0^\pi \left(e^{-jx\cos\theta} - j\cos\theta x\,P_n(\cos\theta)\sin\theta\right.$$

$$\left. + e^{-jx\cos\theta}\,P_n(\cos\theta)\sin\theta\right)d\theta$$

$$\overset{(A.2.8)}{=} \frac{j^n}{2n(n+1)}\int_0^\pi \left[e^{-jx\cos\theta}jx\left(\cos\theta\frac{d}{d\theta}\left(\sin\theta\,P_n^1(\cos\theta)\right)\right)\right.$$

$$\left. - e^{-jx\cos\theta}\frac{d}{d\theta}\left(\sin\theta\,P_n^1(\cos\theta)\right)\right]d\theta$$

$$\overset{(A.2.64)}{=} \frac{j^n}{2n(n+1)}\int_0^\pi \left[e^{-jx\cos\theta}jx\left(\cos\theta\frac{d\,P_n^1(\cos\theta)}{d\theta}\right.\right.$$

$$\left.\left. + \frac{P_n^1(\cos\theta)}{\sin\theta}\right)\sin\theta\right.$$

$$\left. - e^{-jx\cos\theta}jx\sin\theta(\sin\theta\,P_n^1(\cos\theta))\right.$$

$$\left. - e^{-jx\cos\theta}\frac{d}{d\theta}\left(\sin\theta\,P_n^1(\cos\theta)\right)\right]d\theta$$

$$
\stackrel{(A.2.63)}{=} \frac{j^n}{2n(n+1)} \int_0^\pi \left[e^{jx\cos\theta} jx \left(\cos\theta \frac{\mathrm{d}\, P_n^1(\cos\theta)}{\mathrm{d}\theta} \right. \right.
$$

$$
\left. + \frac{P_n^1(\cos\theta)}{\sin\theta} \right) \sin\theta
$$

$$
\left. - \underbrace{\frac{\mathrm{d}}{\mathrm{d}\theta} \left(e^{-jx\cos\theta} \sin\theta\, P_n^1(\cos\theta) \right)}_{\int = 0} \right] \mathrm{d}\theta
$$

$$
= \frac{j^n}{2n(n+1) \int_0^\pi} \int_0^\pi e^{-jx\cos\theta} jx \left(\cos\theta \frac{\mathrm{d}\, P_n^1(\cos\theta)}{\mathrm{d}\theta} \right.
$$

$$
\left. + \frac{P_n^1(\cos\theta)}{\sin\theta} \right) \sin\theta\,\mathrm{d}\theta \qquad\qquad \text{(A.2.65)}
$$

B Acknowledgements

This work wouldn't have been possible without the assistance of many people. First of all I want to thank Prof. Peter Russer for giving me the chance to work at the Institute of Microwave Engineering of the Technische Universität München. Prof. Uwe Siart for his guidance through my research projects including this thesis, and finally Prof. Thomas Eibert for taking over the of the PROCEMA project at the TUM, supervising my thesis and his fruitful advises. I had a great time at the HFT, where I was heartly welcomed and want to thank my former colleagues (especially my roommate Thomas Mittereder and Arndt Ott) for their friendly company. Arndt Ott, Dennis Schobert, Georg Schnattinger and Michael Gruber gave valuable comments concerning my thesis.

The PROCEMA project was a chance to get a deep insight into interdisciplinary research combining microwave engineering and metrology. The chance to join this team was given by Prof. Harald Kunstmann and Prof. Uwe Siart. The communication with my team colleagues, although they were 100 km away, was very good, especially with Christian Chwala, who reviewed my thesis as well. My students Susan Martinfar and Thomas Dengler contributed valuably to this thesis. These acknowledgments would not be complete without being grateful to my parents for giving me so many chances in my life. Especially my father who guided me and got me excited for microwave engineering in my childhood. Thanks to my husband for his great patience and support throughout the whole time of my PhD. He kept me from leaving everything to early and was the first one to read my attempts to write a thesis. My sister Stefanie and my brother Thomas showed interest when reading this book. Last but not least I thank my current colleges Felix Wolfheimer, for reviewing the chapter on electromangnetic theory and his constant encouragement as well as Emma Kowalczuk for correcting my English.

Bibliography

Abramowitz, M. and I. A. Stegun (1964), *Handbook of Mathematical Functions: With Formulas, Graphs, and Mathematical Tables*. Courier Dover Publications, 1964. 1072 pp. ISBN: 9780486612720.

Andsager, K., K. V. Beard, and N. F. Laird (1999), "Laboratory Measurements of Axis Ratios for Large Raindrops". *Journal of the Atmospheric Sciences* 56 (15 Aug. 15, 1999), pp. 2673–2683. DOI: `10.1175/1520-0469(1999)056<2673:LMOARF>2.0.CO;2`.

Asano, S. and G. Yamamoto (1975), "Light Scattering by a Spheroidal Particle". *Applied Optics* 14 (1 Jan. 1975), pp. 29–49. DOI: `10.1364/AO.14.000029`.

Atlas, D. and C. W. Ulbrich (1977), "Path- and Area-Integrated Rainfall Measurement by Microwave Attenuation in the 1-3 cm Band". *Journal of Applied Meteorology* 16 (12 Dec. 1977), pp. 1322–1331. DOI: `10.1175/1520-0450(1977)016<1322:PAAIRM>2.0.CO;2`.

Aydin, K. and S. Daisley (2000), "Rainfall Rate Relationships with Propagation Parameters (attenuation and Phase) at Centimeter and Millimeter Wavelengths". *IEEE International Geoscience and Remote Sensing Symposium (IGARSS)*. Vol. 1. Honolulu, HI, USA, 2000, pp. 177–179. DOI: `10.1109/IGARSS.2000.860460`.

Aydin, K. and S. Daisley (2002), "Relationships Between Rainfall Rate and 35-GHz Attenuation and Differential Attenuation: Modeling the Effects of Raindrop Size Distribution, Canting, and Oscillation". *IEEE Transactions on Geoscience and Remote Sensing* 40 (11 2002), pp. 2343–2352. ISSN: 0196-2892. DOI: `10.1109/TGRS.2002.805073`.

Aydin, K. and Y.-M. Lure (1991), "Millimeter Wave Scattering and Propagation in Rain: A Computational Study at 94 and 140 GHz for Oblate Spheroidal and Spherical Raindrops". *IEEE Transactions on Geoscience and Remote Sensing* 29 (4 1991), pp. 593–601. ISSN: 0196-2892. DOI: `10.1109/36.135821`.

Battaglia, A., P. Saavedra, C. Simmer, and T. Rose (2009), "Rain Observations by a Multifrequency Dual-Polarized Radiometer". *IEEE Geoscience and Remote Sensing Letters* 6 (2 Apr. 2009), pp. 354–358. ISSN: 1545-598X. DOI: `10.1109/LGRS.2009.2013484`.

Battan, L. J. (1973), *Radar Observation of the Atmosphere*. Techbooks, June 1973. 334 pp. ISBN: 9781878907271.

Beard, K. V. and C. Chuang (1987), "A New Model for the Equilibrium Shape of Raindrops". *Journal of the Atmospheric Sciences* 44 (11 June 1987), pp. 1509–1524. DOI: `10.1175/1520-0469(1987)044<1509:ANMFTE>2.0.CO;2`.

Bibliography

Beard, K. and A. Jameson (1983), "Raindrop Canting". *Journal of the Atmospheric Sciences* 40 (2 Feb. 1983), pp. 448–454. DOI: `10.1175/1520-0469(1983)040<0448:RC>2.0.CO;2`.

Berg, M. J., C. M. Sorensen, and A. Chakrabarti (2008a), "Extinction and the Optical Theorem. Part I. Single Particles". *Journal of the Optical Society of America A* 25 (7 July 2008), pp. 1504–1513. DOI: `10.1364/JOSAA.25.001504`.

Berg, M. J., C. M. Sorensen, and A. Chakrabarti (2008b), "Extinction and the Optical Theorem. Part II. Multiple Particles". *Journal of the Optical Society of America A* 25 (7 July 2008), pp. 1514–1520. DOI: `10.1364/JOSAA.25.001514`.

Berne, A. and R. Uijlenhoet (2007), "Path-Averaged Rainfall Estimation Using Microwave Links: Uncertainty Due to Spatial Rainfall Variability". *Geophysical Research Letters* 34 (7 Apr. 2007). DOI: `10.1029/2007GL029409`.

Bohren, C. F. and D. R. Huffman (1983), *Absorption and Scattering of Light by Small Particles*. Wiley, 1983. 547 pp. ISBN: 0471293407, 9780471293408.

Born, M., E. Wolf, and A. B. Bhatia (1999), *Principles of Optics: Electromagnetic Theory of Propagation, Interference and Diffraction of Light*. Cambridge University Press, Oct. 1999. 1000 pp. ISBN: 9780521642224.

Bronstein, I. N. and K. A. Semendjajew (2008), *Taschenbuch der Mathematik*. Harri Deutsch Verlag, 2008. 1325 pp. ISBN: 9783817120079.

Bruning, J. and Yuen Lo (1971a), "Multiple Scattering of EM Waves by Spheres Part I–Multipole Expansion and Ray-Optical Solutions". *IEEE Transactions on Antennas and Propagation* 19 (3 1971), pp. 378–390. ISSN: 0018-926X. DOI: `10.1109/TAP.1971.1139944`.

Bruning, J. and Yuen Lo (1971b), "Multiple Scattering of EM Waves by Spheres Part II–Numerical and Experimental Results". *IEEE Transactions on Antennas and Propagation* 19 (3 1971), pp. 391–400. ISSN: 0018-926X. DOI: `10.1109/TAP.1971.1139925`.

Brussaard, G. (1976), "A Meteorological Model for Rain-Induced Cross Polarization". *IEEE Transactions on Antennas and Propagation* 24 (1 Jan. 1976), pp. 5–11. ISSN: 0018-926X. DOI: `10.1109/TAP.1976.1141282`.

Chandrasekhar, S. (1960), *Radiative Transfer*. Courier Dover Publications, 1960. 420 pp. ISBN: 9780486605906.

Cheffena, M. (2010), "Measurement Analysis of Amplitude Scintillation for Terrestrial Line-of-Sight Links at 42 GHz". *IEEE Transactions on Antennas and Propagation* 58 (6 2010), pp. 2021–2028. ISSN: 0018-926X. DOI: `10.1109/TAP.2010.2046869`.

Chuang, C. C. and K. V. Beard (1990), "A Numerical Model for the Equilibrium Shape of Electrified Raindrops". *Journal of the Atmospheric Sciences* 47 (11 June 1990), pp. 1374–1389. DOI: `10.1175/1520-0469(1990)047<1374:ANMFTE>2.0.CO;2`.

Chwala, C., U. Siart, S. Hipp, T. F. Eibert, and H. Kunstmann (2010a), "Dual-Band Polarimetric Coherent Atmospheric Transmission Experiment for Precipitation Observation". *40th European Microwave Conference (EuMC)*. Paris, France: IEEE, Sept. 28–30, 2010, pp. 1333–1336. ISBN: 978-1-4244-7232-1.

Chwala, C., U. Siart, S. Hipp, T. F. Eibert, and H. Kunstmann (2010b), "Point-to-Point Link Atmospheric Transmission Measurements for Precipitation Quantification". *Kleinheubacher Tagung*. Miltenberg, Germany, Oct. 4–6, 2010.

Chwala, C., U. Siart, S. Hipp, T. F. Eibert, and H. Kunstmann (2011a), "Remote Sensing of Precipitation and Atmospheric Humidity by Microwave Transmission". *Kleinheubacher Tagung*. Miltenberg, Germany, Sept. 26–28, 2011.

Chwala, C., H. Kunstmann, W. Qiu, S. Hipp, U. Siart, J. E. Seltmann, M. Pohl, A. Bradt, and J. Fritz (2011b), "Using Microwave Transmission for Line Integrated Precipitation and Humidity Observation". *12th URSI Commission-F Triennial Open Symposium on Radio Wave Propagation and Remote Sensing*. Garmisch-Partenkirchen, Germany, Mar. 8–11, 2011.

Chwala, C., W. Qiu, S. Hipp, H. Kunstmann, U. Siart, J. E. Seltmann, and M. Pohl (2011c), "Wet/Dry-Estimation Algorithm for Commercial Backhaul Link Attenuation Data to Derive Precipitation Intensity in Alpine Terrain". *European Geoscience Union General Assembly (EGU)*. Vienna, Austria, Apr. 3–8, 2011.

Chwala, C., A. Gmeiner, W. Qiu, S. Hipp, D. Nienaber, U. Siart, T. F. Eibert, M. Pohl, J. E. Seltmann, J. Fritz, and H. Kunstmann (2012), "Precipitation Observation Using Microwave Backhaul Links in the Alpine and Pre-Alpine Region of Southern Germany". *Hydrology and Earth System Sciences* 16.8 (Jan. 13, 2012), pp. 2647–2661. DOI: 10.5194/hess-16-2647-2012.

Crane, R. K. (1996), *Electromagnetic Wave Propagation Through Rain*. Wiley-Interscience, 1996.

Cummings, R., G. Upton, A. Holt, and M. Kitchen (2009), "Using Microwave Links to Adjust the Radar Rainfall Field". *Advances in Water Resources* 32 (7 2009), pp. 1003–1010. ISSN: 0309-1708. DOI: 10.1016/j.advwatres.2008.08.010.

Czekala, H. and C. Simmer (1998), "Microwave Radiative Transfer with Nonspherical Precipitating Hydrometeors". *Journal of Quantitative Spectroscopy and Radiative Transfer* 60 (3 Sept. 1998), pp. 365–374. ISSN: 00224073. DOI: 10.1016/S0022-4073(98)00012-0.

Deiveegan, M., C. Balaji, and S. Venkateshan (2008), "A Polarized Microwave Radiative Transfer Model for Passive Remote Sensing". *Atmospheric Research* 88 (3-4 June 2008), pp. 277–293. ISSN: 0169-8095. DOI: 10.1016/j.atmosres.2007.11.023.

Deutscher Wetterdienst: Weather Extremes - Wind (2012). Apr. 10, 2012. URL: http://www.dwd.de.

Draine, B. T. and P. J. Flatau (1994), "Discrete-Dipole Approximation for Scattering Calculations". *Journal of the Optical Society of America A* 11 (4 Apr. 1994), pp. 1491–1499. DOI: 10.1364/JOSAA.11.001491.

Evans, K. and G. Stephens (1991), "A New Polarized Atmospheric Radiative Transfer Model". *Journal of Quantitative Spectroscopy and Radiative Transfer* 46 (5 Nov. 1991), pp. 413–423. ISSN: 0022-4073. DOI: 10.1016/0022-4073(91)90043-P.

Fiser, O. and D. Rezacova (2007), "Rain Measurement for Improved Propagation Modelling in Czech Republic". *2nd European Conference on Antennas and Propagation (EuCAP)*. Edinburgh, UK, Nov. 11–16, 2007, pp. 1–7.

Garcia-Rubia, J. M, J. M Riera, A. Benarroch, and P. Garcia-del Pino (2011), "Estimation of Rain Attenuation From Experimental Drop Size Distributions". English. *IEEE Antennas and Wireless Propagation Letters* 10 (2011), pp. 839–842. ISSN: 1536-1225. DOI: 10.1109/LAWP.2011.2163609.

Goldshtein, O., H. Messer, and A. Zinevich (2009), "Rain Rate Estimation Using Measurements From Commercial Telecommunications Links". *IEEE Transactions on Signal Processing* 57 (4 2009), pp. 1616–1625. ISSN: 1053-587X. DOI: `10.1109/TSP.2009.2012554`.

Gunn, R. and G. D. Kinzer (1949), "The Terminal Velocity of Fall for Water Droplets in Stagnant Air". *Journal of the Atmospheric Sciences* 6 (4 Aug. 1949), pp. 243–248. DOI: `10.1175/1520-0469(1949)006<0243:TTVOFF>2.0.CO;2`.

Hipp, S., C. Chwala, U. Siart, T. F. Eibert, and H. Kunstmann (2010), "Modelling of Electromagnetic Scattering in Rain Fields for Precipitation Quantification". *Kleinheubacher Tagung*. Miltenberg, Germany, Oct. 4–6, 2010.

Hipp, S., U. Siart, C. Chwala, T. F. Eibert, and H. Kunstmann (2011a), "Doppler Noise Modeling for Rain-Rate Obseravtion by Ground-Based Transmission Measurement". *12th URSI Commission-F Triennial Open Symposium on Radio Wave Propagation and Remote Sensing*. Garmisch-Partenkirchen, Germany, Mar. 8–11, 2011.

Hipp, S., U. Siart, C. Chwala, T. F. Eibert, and H. Kunstmann (2011b), "Dynamic Modelling of Atmospheric Microwave Transmission for Precipitation Quantification Using Mie Scattering". English. *5th European Conference on Antennas and Propagation (EUCAP)*. Rome, Italy: IEEE, Apr. 11–15, 2011, pp. 3380–3383. ISBN: 978-1-4577-0250-1.

Hipp, S., U. Siart, C. Chwala, T. F. Eibert, and H. Kunstmann (2011c), "Improved Numerical Efficiency for Modelling of Electromagnetic Attenuation and Noise from Rain Fields with Different Rain Rate". *Kleinheubacher Tagung*. Miltenberg, Germany, Sept. 26–28, 2011.

Hipp, S., U. Siart, C. Chwala, H. Kunstmann, and T. F. Eibert (2011d), "Rainfall Noise Modeling for Sensing the Atmosphere by Microwaves". *European Geoscience Union General Assembly (EGU)*. Vienna, Austria, Apr. 3–8, 2011.

Hirata, A., R. Yamaguchi, H. Takahashi, T. Kosugi, K. Murata, N. Kukutsu, and Y. Kado (2009), "Effect of Rain Attenuation for a 10-Gb/s 120-GHz-Band Millimeter-Wave Wireless Link". *IEEE Transactions on Microwave Theory and Techniques* 57 (12 2009), pp. 3099–3105. ISSN: 0018-9480. DOI: `10.1109/TMTT.2009.2034342`.

Holt, A., G. Kuznetsov, and A. Rahimi (2003), "Comparison of the Use of Dual-Frequency and Single-Frequency Attenuation for the Measurement of Path-Averaged Rainfall Along a Microwave Link". *IEE Proceedings - Microwaves, Antennas and Propagation* 150 (5 2003), pp. 315–320. ISSN: 1350-2417. DOI: `10.1049/ip-map:20030616`.

Holt, A., J. Goddard, G. Upton, M. Willis, A. Rahimi, P. Baxter, and C. Collier (2000), "Measurement of Rainfall by Dual-Wavelength Microwave Attenuation". *Electronics Letters* 36 (25 2000), pp. 2099–2101. ISSN: 0013-5194. DOI: `10.1049/el:20001468`.

Hornbostel, A., A. Schroth, B. Kutuza, and A. Evtuchenko (1997), "Dual Polarisation and Multifrequency Measurements of Rain Rate and Drop Size Distribution by Ground-Based Radar and Radiometers". *IEEE International Geoscience and Remote Sensing Symposium (IGARSS)*. Vol. 3. Singapore, 1997, 1126–1128 vol.3. DOI: `10.1109/IGARSS.1997.606372`.

Ishimaru, A. (1997), *Wave Propagation and Scattering in Random Media*. John Wiley and Sons, 1997. 539 pp. ISBN: 0780334094.

Ishimaru, A. and R. Cheung (1980), "Multiple Scattering Effects on Wave Propagation Due to Rain". *Annales des Télécommunication* 35 (11-12 1980). 10.1007/BF03003515, pp. 373–379. ISSN: 0003-4347. DOI: 10.1007/BF03003515.

ITU, *Attenuation by Atmospheric Gases*. Recommendation P.676. Geneve.

ITU, *Attenuation Due to Clouds and Fog*. Recommendation P.840. Geneve.

ITU, *Calculation of Free-Space Attenuation*. Recommendation P.525. Geneve.

ITU, *Characteristics of Precipitation for Propagation Modelling*. Recommendation P.837. Geneve.

ITU, *Characterization of the Natural Variability of Propagation Phenomena*. Recommendation P.678. Geneve.

ITU, *Differential Rain Attenuation*. Recommendation P.1815. Geneve.

ITU, *Exchange of Information for Short-Term Forecasts and Transmission of Ionospheric Disturbance Warnings*. Recommendation P.313. Geneve.

ITU, *Propagation by Diffraction*. Recommendation P.526. Geneve.

ITU, *Propagation Data and Prediction Methods Required for the Design of Earth-Space Telecommunication Systems*. Recommendation P.618. Geneve.

ITU, *Propagation Data and Prediction Methods Required for the Design of Terrestrial Line-of-Sight Systems*. Recommendation P.530. Geneve.

ITU, *Rain Height Model for Prediction Methods*. Recommendation P.839. Geneve.

ITU, *Specific Attenuation Model for Rain for Use in Prediction Methods*. Recommendation P.838. Geneve.

ITU, *The Radio Refractive Index: Its Formula and Refractivity Data*. Recommendation P.453. Geneve.

ITU, *Water Vapour: Surface Density and Total Columnar Content*. Recommendation P.836. Geneve.

ITU (2008), *Radiowave Propagation Information for Designing Terrestrial Point-to-Point Links*. ITU-R, 2008.

Jackson, J. D. (1998), *Classical Electrodynamics*. Wiley, Aug. 10, 1998. 832 pp. ISBN: 9780471309321.

Joss, J., J. C. Thams, and A. Waldvogel (1968), "The Variation of Raindrop Size Distributions at Locarno". *International Conference on Cloud Physics*. Toronto, Ontario, Canada: International Association of Meteorology and Atmospheric Physics, 1968, pp. 369–373.

Kahnert, M. F. (2003), "Numerical Methods in Electromagnetic Scattering Theory". *Journal of Quantitative Spectroscopy and Radiative Transfer* 79-80 (2003), pp. 775–824. DOI: 10.1016/S0022-4073(02)00321-7.

Kerker, M. (1969), *The Scattering of Light, and Other Electromagnetic Radiation*. Academic Press, 1969. 680 pp.

Kunstmann, H., C. Chwala, S. Hipp, W. Qiu, and U. Siart (2010), "Precipitation Quantification by Cellular-Network Backhaul-Link Signal Attenuation and a Monostatic Atmospheric Transmission Experiment". *European Geosciences Union General Assembly (EGU)*. Vienna, Austria, May 2–7, 2010, p. 9444.

Laws, J. and D. Parsons (1943), "The Relation of Raindrop-Size to Intensity". *Transactions of the American Geophysics Union* 24 (Part II 1943), pp. 452–460.

Leijnse, H., R. Uijlenhoet, and J. N. M. Stricker (2007), "Rainfall Measurement Using Radio Links from Cellular Communication Networks". *Water Resources Research* 43 (3 Mar. 2007), 6 PP. DOI: `10.1029/2006WR005631`.

Leijnse, H., R. Uijlenhoet, and J. Stricker (2008), "Microwave Link Rainfall Estimation: Effects of Link Length and Frequency, Temporal Sampling, Power Resolution, and Wet Antenna Attenuation". *Advances in Water Resources* 31 (11 Nov. 2008), pp. 1481–1493. ISSN: 0309-1708. DOI: `10.1016/j.advwatres.2008.03.004`.

Leijnse, H. (2007), "Hydrometeorological Application of Microwave Links". Wageningen University, 2007. 158 pp.

Liebe, H. J., G. A. Hufford, and T. Manabe (1991), "A Model for the Complex Permittivity of Water at Frequencies Below 1 THz". *International Journal of Infrared and Millimeter Waves* 12 (7 1991), pp. 659–675. ISSN: 0195-9271. DOI: `10.1007/BF01008897`.

Luini, L. and C. Capsoni (2009), "MultiEXCELL: A New Rainfall Model for the Analysis of the Millimetre Wave Propagation Through the Atmosphere". English. *3rd European Conference on Antennas and Propagation (EuCAP)*. Berlin, Germany: IEEE, Mar. 23–27, 2009, pp. 1946–1950. ISBN: 978-1-4244-4753-4.

Luini, L. and C. Capsoni (2010), "A Physically Based Methodology for the Evaluation of the Rain Attenuation on Terrestrial Radio Links". English. *4th European Conference on Antennas and Propagation (EuCAP)*. Barcelona, Spain: IEEE, Apr. 12–16, 2010, pp. 1–5. ISBN: 978-1-4244-6431-9.

MANTISSA (Microwave Attenuation a a New Tool for Improving Storm-water Supervision Administration) (2009). Mar. 20, 2009. URL: `http://prswww.essex.ac.uk/mantissa/`.

Marshall, J. and W. M. Palmer (1948), "The Distribution of Raindrops with Size". *Journal of Meteorology* 5 (4 Aug. 1948), pp. 165–166. DOI: `10.1175/1520-0469(1948)005<0165:TDORWS>2.0.CO;2`.

Marzano, F. S., G. Botta, and M. Montopoli (2010), "Iterative Bayesian Retrieval of Hydrometeor Content From X-Band Polarimetric Weather Radar". *IEEE Transactions on Geoscience and Remote Sensing* 48 (8 2010), pp. 3059–3074. ISSN: 0196-2892. DOI: `10.1109/TGRS.2010.2045231`.

Matricciani, E. (1996), "Physical Mathematical Model of the Dynamics of Rain Attenuation Based on Rain Rate Time Series and a Two-Layer Vertical Structure of Precipitation". *Radio Science* 31 (2 Mar.–Apr. 1996), pp. 281–295. ISSN: 0048-6604. DOI: `10.1029/95RS03129`.

Matricciani, E. (2009), "A Relationship Between Phase Delay and Attenuation Due to Rain and Its Applications to Satellite and Deep-Space Tracking". *IEEE Transactions on Antennas and Propagation* 57 (11 Nov. 2009), pp. 3602 –3611. ISSN: 0018-926X. DOI: `10.1109/TAP.2009.2024177`.

Medhurst, R. (1965), "Rainfall Attenuation of Centimeter Waves: Comparison of Theory and Measurement". English. *IEEE Transactions on Antennas and Propagation* 13 (4 July 1965), pp. 550–564. ISSN: 0018-926X. DOI: `10.1109/TAP.1965.1138472`.

Messer, H., O. Goldshtein, A. Rayitsfeld, and P. Alpert (2008), "Recent Results of Rainfall Mapping from Cellular Network Measurements". *IEEE International Conference on Acoustics, Speech and Signal Processing (ICASSP)*. Las Vegas, NV, USA, 2008, pp. 5157–5160. ISBN: 1520-6149. DOI: `10.1109/ICASSP.2008.4518820`.

Messer, H., A. Zinevich, and P. Alpert (2006), "Environmental Monitoring by Wireless Communication Networks". *Science* 312 (5774 May 2006), p. 713. DOI: `10.1126/science.1120034`.

Mie, G. (1908), "Beiträge zur Optik trüber Medien, speziell kolloidaler Metallösungen". *Annalen der Physik* 330 (3 Jan. 1, 1908), pp. 377–445. ISSN: 1521-3889. DOI: `10.1002/andp.19083300302`.

Minda, H. and K. Nakamura (2005), "High Temporal Resolution Path-Average Rain Gauge with 50-GHz Band Microwave". *Journal of Atmospheric and Oceanic Technology* 22 (2 Feb. 2005), pp. 165–179. DOI: `10.1175/JTECH-1683.1`.

Mishchenko, M. I. (2008), "Broadband Electromagnetic Scattering by Particles". *Journal of the Optical Society of America A* 25 (12 Dec. 2008), pp. 2893–2895. DOI: `10.1364/JOSAA.25.002893`.

Mishchenko, M. I., L. D. Travis, and D. W. Mackowski (1996), "T-Matrix Computations of Light Scattering by Nonspherical Particles: A Review". *Journal of Quantitative Spectroscopy and Radiative Transfer* 55 (5 May 1996), pp. 535–575. ISSN: 0022-4073. DOI: `10.1016/0022-4073(96)00002-7`.

Mishchenko, M. I., L. Liu, D. W. Mackowski, B. Cairns, and G. Videen (2007), "Multiple Scattering by Random Particulate Media: Exact 3d Results". *Optics Express* 15 (6 Mar. 19, 2007), pp. 2822–2836. DOI: `10.1364/OE.15.002822`.

Moon, P. H. and D. E. Spencer (1988), *Field Theory Handbook: Including Coordinate Systems, Differential Equations, and Their Solutions*. Springer-Verlag, 1988. 256 pp. ISBN: 9780387184302.

Nešpor, V. and B. Sevruk (1999), "Estimation of Wind-Induced Error of Rainfall Gauge Measurements Using a Numerical Simulation". *Journal of Atmospheric and Oceanic Technology* 16 (4 Apr. 1999), pp. 450–464. ISSN: 0739-0572, 1520-0426. DOI: `10.1175/1520-0426(1999)016<0450:EOWIEO>2.0.CO;2`.

Oguchi, T. (1983), "Electromagnetic Wave Propagation and Scattering in Rain and Other Hydrometeors". *Proceedings of the IEEE* 71 (9 1983), pp. 1029–1078. ISSN: 0018-9219. DOI: `10.1109/PROC.1983.12724`.

Oguchi, T. (1973), "Attenuation and Phase Rotation of Radio Waves Due to Rain: Calculations at 19.3 and 34.8 GHz". *Radio Science* 8 (1 1973), pp. 31–38. DOI: `197310.1029/RS008i001p00031`.

Olsen, R., D. Rogers, and D. Hodge (1978), "The aR^b Relation in the Calculation of Rain Attenuation". *IEEE Transactions on Antennas and Propagation* 26 (2 Mar. 1978), pp. 318–329. ISSN: 0018-926X. DOI: `10.1109/TAP.1978.1141845`.

Pruppacher, H. R. and K. V. Beard (1970), "A Wind Tunnel Investigation of the Internal Circulation and Shape of Water Drops Falling at Terminal Velocity in Air". *Quarterly Journal of the Royal Meteorological Societ* 96 (Apr. 1970), pp. 247–256. DOI: `10.1002/qj.49709640807`.

Bibliography

Pruppacher, H. and R. Pitter (1971), "A Semi-Empirical Determination of the Shape of Cloud and Rain Drops". *Journal of the Atmospheric Sciences* 28 (1 Jan. 1971), pp. 86–94. ISSN: 15200469. DOI: `10.1175/1520-0469(1971)028<0086:ASEDOT> 2.0.CO;2`.

Rahimi, A. R., A. R. Holt, G. J. G. Upton, and R. J. Cummings (2003), "Use of Dualfrequency Microwave Links for Measuring Path-Averaged Rainfall". *Journal of Geophysical Research: Atmospheres* 108 (D15 2003), p. 4467. DOI: `10.1029/2002JD003202`.

Rahimi, A. R., A. R. Holt, G. J. G. Upton, S. Krämer, A. Redder, and H. R. Verworn (2006), "Attenuation Calibration of an X-Band Weather Radar Using a Microwave Link". *Journal of Atmospheric and Oceanic Technology* 23 (3 2006), pp. 395–405. DOI: `10.1175/JTECH1855.1`.

Rahimi, A. (2004), *Statistical Validation of Rainfall Estimates Obtained from Microwave Attenuation*. 2004.

Ray, P. S. (1972), "Broadband Complex Refractive Indices of Ice and Water". *Applied Optics* 11 (8 1972), pp. 1836–1844. DOI: `10.1364/AO.11.001836`.

Rincon, R. and R. Lang (2002), "Microwave Link Dual-Wavelength Measurements of Path-Average Attenuation for the Estimation of Drop Size Distributions and Rainfall". *IEEE Transactions on Geoscience and Remote Sensing* 40 (4 2002), pp. 760–770. ISSN: 0196-2892. DOI: `10.1109/TGRS.2002.1006324`.

Rogers, D. V. and R. L. Olsen (1983), "Multiple Scattering in Coherent Radiowave Propagation Through Rain". *COMSAT Technical Review* 13 (1983), pp. 385–401.

Rogers, R. (1976), "Statistical Rainstorm Models: Their Theoretical and Physical Foundations". *IEEE Transactions on Antennas and Propagation* 24 (4 1976), pp. 547–566. ISSN: 0018-926X. DOI: `10.1109/TAP.1976.1141359`.

Ruf, C. S., K. Aydin, S. Mathur, and J. P. Bobak (1996), "35-GHz Dual-Polarization Propagation Link for Rain-Rate Estimation". *Journal of Atmospheric and Oceanic Technology* 13 (2 Apr. 1996), pp. 419–425. DOI: `10.1175/1520-0426(1996) 013<0419:GDPPLF>2.0.CO;2`.

Russchenberg, H. and L. Ligthart (1992), "Ground-Based Remote Sensing of Precipitation Using a Multi-Polarized FM-CW Doppler Radar". TU Delft, Dec. 14, 1992.

Ryde, J. and D. Ryde (1944), "Attenuation of Centimetre Waves by Rain, Hail, and Clouds". *General Electric Co. Research Laboratories* 8516 (1944).

ScattPort (2009). July 30, 2009. URL: `http://www.scattport.org/`.

Schleiss, M. and A. Berne (2010), "Identification of Dry and Rainy Periods Using Telecommunication Microwave Links". *IEEE Geoscience and Remote Sensing Letters* 7 (3 2010), pp. 611–615. ISSN: 1545-598X. DOI: `10.1109/LGRS.2010.2043052`.

Schleiss, M. A., A. Berne, and R. Uijlenhoet (2009), "Geostatistical Simulation of Two-Dimensional Fields of Raindrop Size Distributions at the Meso-Λ Scale". *Water Resources Research* 45 (7 July 18, 2009), p. 10. DOI: `200910.1029/2008WR007545`.

Setijadi, E., A. Matsushima, N. Tanaka, and G. Hendrantoro (2009), "Effect of Temperature and Multiple Scattering on Rain Attenuation of Electromagnetic Waves by a Simple Spherical Model". *Progress In Electromagnetics Research* 99 (2009), pp. 339–354. DOI: `10.2528/PIER09102609`.

Sevruk, B. and L. Zahlavova (1994), "Classification System of Precipitation Gauge Site Exposure: Evaluation and Application". *International Journal of Climatology* 14 (6 July 1994), pp. 681–689. ISSN: 1097-0088. DOI: `10.1002/joc.3370140607`.

Siart, U., S. Hipp, T. F. Eibert, C. Chwala, and H. Kunstmann (2012), "Efficient Modelling of Rain Field Microwave Attenuation and Doppler Noise for Different Drop Size Distributions". *12th Specialist Meeting on Microwave Radiometry and Remote Sensing of the Environment (MicroRad)*. Rome, Italy, Mar. 5–9, 2012, pp. 1–3. DOI: `10.1109/MicroRad.2012.6185245`.

Sihvola, A. and J. Kong (1988), "Effective Permittivity of Dielectric Mixtures". *IEEE Transactions on Geoscience and Remote Sensing* 26 (4 1988), pp. 420–429. ISSN: 0196-2892. DOI: `10.1109/36.3045`.

Simpson, J., C. Kummerow, W. K. Tao, and R. F. Adler (1996), "On the Tropical Rainfall Measuring Mission (TRMM)". *Meteorology and Atmospheric Physics* 60 (1 Mar. 1996), pp. 19–36. ISSN: 0177-7971. DOI: `10.1007/BF01029783`.

Siqueira, P. and K. Sarabandi (1996), "Determination of Effective Permittivity for Three-Dimensional Random Media". *Antennas and Propagation Society International Symposium (AP-S)*. Vol. 3. Baltimore, MD, USA, 1996, pp. 1780–1783. DOI: `10.1109/APS.1996.549948`.

Smith, E., G. Asrar, Y. Furuhama, A. Ginati, A. Mugnai, K. Nakamura, R. Adler, M.-D. Chou, M. Desbois, J. Durning, J. Entin, F. Einaudi, R. Ferraro, R. Guzzi, P. Houser, P. Hwang, T. Iguchi, P. Joe, R. Kakar, J. Kaye, M. Kojima, C. Kummerow, K.-S. Kuo, D. Lettenmaier, V. Levizzani, N. Lu, A. Mehta, C. Morales, P. Morel, T. Nakazawa, S. Neeck, K. Okamoto, R. Oki, G. Raju, J. Shepherd, J. Simpson, B. Sohn, E. Stocker, W.-K. Tao, J. Testud, G. Tripoli, E. Wood, S. Yang, and W. Zhang (2007), "Measuring Precipitation From Space". In collab. with V. Levizzani, P. Bauer, and F. J. Turk. Vol. 28. Advances in Global Change Research. Springer Netherlands, 2007, pp. 611–653. ISBN: 978-1-4020-5835-6.

Sreerekha, T. R., C. Emde, N. Courcoux, C. Teichmann, S. A. Buehler, U. Loehnert, M. Mech, S. Crewell, A. Battaglia, P. Eriksson, B. Rydberg, C. Davis, C. Jimenez, S. English, and A. Doherty (2006), *Development of an RT model for frequencies between 200 and 1000 GHz*. Final Report. 2006.

Stratton, J. A. (2007), *Electromagnetic Theory*. Wiley-IEEE, 2007. 642 pp. ISBN: 9780470131534.

Szakáll, M., K. Diehl, S. K. Mitra, and S. Borrmann (2009), "A Wind Tunnel Study on the Shape, Oscillation, and Internal Circulation of Large Raindrops with Sizes between 2.5 and 7.5 mm". *Journal of Atmospheric and Oceanic Technology* 66 (3 Mar. 2009), pp. 755–765. DOI: `10.1175/2008JAS2777.1`.

Townsend, A. J. and R. J. Watson (2011), "The Linear Relationship Between Attenuation and Average Rainfall Rate for Terrestrial Links". *IEEE Transactions on Antennas and Propagation* 59 (3 2011), pp. 994–1002. ISSN: 0018-926X. DOI: `10.1109/TAP.2010.2103021`.

Townsend, A. J, R. J Watson, and D. D Hodges (2009), "The Effect of Raindrop Size Distribution Variability on the Estimation of Attenuation". *3rd European Conference*

on Antennas and Propagation (EuCAP). Berlin, Germany: IEEE, Mar. 23–27, 2009, pp. 313–317. ISBN: 978-1-4244-4753-4.

Tsolakis, A. and W. L. Stutzman (1982), "Multiple Scattering of Electromagnetic Waves by Rain". *Radio Science* 17 (6 1982), pp. 1495–1502. DOI: `10.1029/RS017i006p01495`.

Ulbrich, C. W. (1983), "Natural Variations in the Analytical Form of the Raindrop Size Distribution". *Journal of Climate and Applied Meteorology* 22 (10 Oct. 1983), pp. 1764–1775. DOI: `10.1175/1520-0450(1983)022<1764:NVITAF>2.0.CO;2`.

Upton, G., A. Holt, R. Cummings, A. Rahimi, and J. Goddard (2005), "Microwave Links: The Future for Urban Rainfall Measurement?" *Atmospheric Research* 77 (1-4 2005), pp. 300–312. ISSN: 0169-8095. DOI: `10.1016/j.atmosres.2004.10.009`.

Valtr, P., P. Pechac, V. Kvicera, and M. Grabner (2011), "Estimation of the Refractivity Structure of the Lower Troposphere From Measurements on a Terrestrial Multiple-Receiver Radio Link". *IEEE Transactions on Antennas and Propagation* 59 (5 2011), pp. 1707–1715. ISSN: 0018-926X. DOI: `10.1109/TAP.2011.2122234`.

van Bladel, J. (2007), *Electromagnetic Fields*. John Wiley & Sons, June 4, 2007. 1171 pp. ISBN: 9780471263883.

van de Hulst, H. C. (1981), *Light Scattering by Small Particles*. New York: Dover, 1981. ISBN: 0-486-64228-3.

Vogl, S., P. Laux, W. Qiu, G. Mao, and H. Kunstmann (2012), "Copula-based assimilation of radar and gauge information to derive bias-corrected precipitation fields". *Hydrology and Earth System Sciences* 16.7 (2012), pp. 2311–2328. DOI: `10.5194/hess-16-2311-2012`.

Waterman, P. C. (1976), "Matrix Theory of Elastic Wave Scattering". *The Journal of the Acoustical Society of America* 60 (3 1976), p. 567. ISSN: 00014966. DOI: `10.1121/1.381130`.

Welch, P. (1967), "The Use of Fast Fourier Transform for the Estimation of Power Spectra: A Method Based on Time Averaging Over Short, Modified Periodograms". *IEEE Transactions on Audio and Electroacoustics* 15 (2 June 1967), pp. 70–73. ISSN: 0018-9278. DOI: `10.1109/TAU.1967.1161901`.

Windfinder - Wind Statistics Map Europe (2012). Apr. 10, 2012. URL: `http://www.windfinder.com`.

Wiscombe, W. J. (1980), "Improved Mie Scattering Algorithms". *Applied Optics* 19 (9 May 1980), pp. 1505–1509. DOI: `10.1364/AO.19.001505`.

Zhang, G., J. Vivekanandan, and E. Brandes (2001), "A Method for Estimating Rain Rate and Drop Size Distribution from Polarimetric Radar Measurements". *IEEE Transactions on Geoscience and Remote Sensing* 39 (4 2001), pp. 830–841. ISSN: 0196-2892. DOI: `10.1109/36.917906`.

Zinevich, A., P. Alpert, and H. Messer (2008), "Estimation of Rainfall Fields Using Commercial Microwave Communication Networks of Variable Density". *Advances in Water Resources* 31 (11 Nov. 2008), pp. 1470–1480. ISSN: 0309-1708. DOI: `10.1016/j.advwatres.2008.03.003`.

Zurk, L. M., L. Tsang, and D. P. Winebrenner (1996), "Scattering Properties of Dense Media from Monte Carlo Simulations with Application to Active Remote Sensing of Snow". *Radio Science* 31 (4 1996), pp. 803–819. DOI: 199610.1029/96RS00939.

Zvanovec, S. and P. Pechac (2011), "Validation of Rain Spatial Classification for High Altitude Platform Systems". English. *IEEE Transactions on Antennas and Propagation* 59 (7 July 2011), pp. 2746–2750. ISSN: 0018-926X. DOI: 10.1109/TAP.2011. 2152325.